UNIVERSITY OF OKLAHOMA

GRADUATE COLLEGE

INVESTIGATIONS OF THE TRICUSPID HEART VALVE FUNCTION: AN INTEGRATED COMPUTATIONAL-EXPERIMENTAL APPROACH

A THESIS

SUBMITTED TO THE GRADUATE FACULTY

in partial fulfillment of the requirements for the

Degree of

MASTER OF SCIENCE

By

DEVIN WILLIAM LAURENCE
Norman, Oklahoma
2019

INVESTIGATIONS OF THE TRICUSPID HEART VALVE FUNCTION:

AN INTEGRATED COMPUTATIONAL-EXPERIMENTAL APPROACH

A THESIS APPROVED FOR THE
SCHOOL OF AEROSPACE AND MECHANICAL ENGINEERING

BY

Dr. Zahed Siddique

Dr. Kuang-Hua Chang

Dr. Handan Acar

Dr. Ryan Baumwart

Dr. Chung-Hao Lee, Chair

To my family

Without your love and support, this would not be possible.

Table of Contents

List of Figures ix

List of Tables xvii

Acknowledgments xviii

Abstract of the Thesis xix

CHAPTER 1 Introduction 1

1.1 Motivation 1

1.2 Objective and Scope 2

CHAPTER 2 Literature Review 6

2.1 Overview of the Tricuspid Valve Anatomy and Function 6

2.1.1 The Tricuspid Valve Anatomy 6

2.1.2 Tricuspid Valve Organ-Level Function 10

2.1.3 Microstructure of The Tricuspid Valve Leaflet 10

2.2 Overview of Tricuspid Regurgitation 12

2.2.1 Tricuspid Regurgitation 12

2.2.2 Clinical Assessment and Diagnosis 15

2.2.3 Clinical Treatment of Tricuspid Regurgitation 17

2.3 Mechanical Properties of the Heart Valve Leaflets 18

2.3.1 The Mitral and Aortic Valve Leaflets 19

2.3.2 The Tricuspid Valve Leaflets 22

2.4 Constitutive Modeling 23

2.4.1 Common Constitutive Models for the Heart Valves 24
2.5 Computational Modeling of the Heart Valve Function 26
2.5.1 Computational Models of the Tricuspid Valve 27
CHAPTER 3 Finite Element Model of the Tricuspid Valve 30
3.1 Geometry and Finite Element Mesh 31
3.1.1 Tricuspid Valve Leaflets 31
3.1.2 Chordae Tendineae 32
3.1.3 Finite Element Computational Mesh 33
3.2 Material Model 34
3.3 Boundary and Loading Conditions 36
3.4 Simulation of Healthy TV Closure 38
3.4.1 Simulation Results – Geometrical Metrics 39
3.4.2 Simulation Results – Engineering Mechanics Metrics 45
3.5 Discussion 48
CHAPTER 4 Finite Element Simulations of the Diseased Tricuspid Valve 50
4.1 Study Scenarios of Various Pathological Conditions 51
4.1.1 Pulmonary Hypertension 51
4.1.2 Flattened Annulus 52
4.1.3 Annular Dilation 52
4.1.4 Papillary Muscle Displacement 54
4.1.5 Fully-Diseased Scenario 56
4.1.6 Chordae Tendineae Rupture 57
4.2 FE Simulation Results of Various Pathological Scenarios – Engineering Mechanics

Metrics 58

4.3 FE Simulation Results of Various Pathological Scenarios – Geometrical Metrics 64

4.4 Chordae Rupture Scenario Results 67

4.5 Discussion 69

CHAPTER 5 Biaxial Mechanical Characterizations of the Tricuspid Valve 71

5.1 Methods 72

5.1.1 Tissue Acquisition 72

5.1.2 Baseline Investigation 73

5.1.3 Regional Variations Investigation 75

5.1.4 GAG Contribution Investigation 77

5.1.5 Stress and Strain Calculations 78

5.1.6 Statistical Analysis 80

5.2 Results 80

5.2.1 Baseline Investigation 80

5.2.2 Regional Variations 84

5.2.3 GAG Contribution to the TV Mechanics Responses 86

5.3 Discussion 90

5.3.1 Baseline Investigations 90

5.3.2 Investigation of Regional Variations 91

5.3.3 GAG Contributions to the TV Mechanical Behavior 92

CHAPTER 6 Constitutive Modeling of the Tricuspid Valve Biaxial Mechanical Response 94

6.1 Constitutive Modeling Framework 96

6.2 Differential Evolution Algorithm 98
6.3 Model Fitting Results 101
6.3.1 Strain Energy Density Form Proposed by Lee et al. 102
6.3.2 Fung-Type Strain Energy Density Form 104
6.4 Discussion 107
CHAPTER 7 Conclusions and Future Work 109
7.1 Conclusions 109
7.1.1 Finite Element Computational Model of the Tricuspid Valve 109
7.1.2 Numerical Investigations of the Pathological Tricuspid Valve Via In Silico Modeling 110
7.1.3 Biaxial Mechanical Characterizations of Tricuspid Valve Leaflets 110
7.1.4 Constitutive Modeling Framework 111
7.2 Recommendations for Future Research 112
APPENDIX A Nomenclature 115
APPENDIX B ABAQUS Input File Description 119
APPENDIX C Biaxial Mechanical Testing Procedures 125
References 143

List of Figures

Figure 2-1: (a) Schematic of the TV within the heart chambers (image adapted from uptodate.com). (b) Excised porcine heart showing the key components of the TV, including the TV leaflets, annulus, and the chordae tendineae. 7

Figure 2-2: Annuloplasty ring for the TV shape, demonstrating a clear saddle-shaped TV annulus. Image was adapted from [40]. 8

Figure 2-3: Average chordae tendineae thickness (*top*) and length (*bottom*) for each classification and each leaflet (MVAL: MV anterior leaflet, MVPL: MV posterior leaflet). Values are reported as mean ± the standard error of the mean (SEM). A horizontal bar denotes $p<0.01$, ** denotes $p<0.001$. Image was adapted from [110]..... 9

Figure 2-4: Histological images using Masson's trichrome staining, illustrating the microstructure (dark blue: collagen fibers, black: nuclei, and red: cytoplasm) and layers (A: atrialis, S: spongiosa, F: fibrosa, and V: ventricularis) of the TV leaflets. Image was adapted from [59]..... 11

Figure 2-5: Movat's Pentachrome histological staining of the TVAL tissue, showing the complex microstructure. Image was adopted from [72]. 12

Figure 2-6: The number of publications (*left*) and number of total citations (*right*) since 1990 for the four heart valves. Data was adopted from *Web of Science*. 14

Figure 2-7: The observed probability that a leaflet combination appears on a given 2DTTE imaging perspective. Image was adapted from [1]. 16

Figure 2-8: 2DTTE (*left*) and color Doppler imaging (*right*) of the four-chamber view of an infant patient with pulmonary atresia. Image courtesy of Children's Heart

Center at the OU Health Sciences Center. 17

Figure 2-9: Schematic of the experimental setups of typical uniaxial testing (*left*) and biaxial testing (*right*)..... 20

Figure 2-10: Comparison between the uniaxial and biaxial mechanical testing of the MV leaflet tissues. Images were modified from [90]..... 20

Figure 2-11: Representative data from [65] for the TVAL tissue under (a) the equibiaxial loading protocol (i.e., T_{circ}:T_{rad} = 1:1), (b) T_{circ}:T_{rad} = 1:0.75 loading protocol, (c) T_{circ}:T_{rad} = 0.75:1 loading protocol, (d) T_{circ}:T_{rad} = 1:0.5 loading protocol, and (e) T_{circ}:T_{rad} = 0.5:1 loading protocol. 23

Figure 2-12: FE simulation results from [71] for the three patients' data sets. 29

Figure 3-1: Experimental photo of an excised porcine TV with highlighted key anatomical features and dimensions. 32

Figure 3-2: FE mesh for the combined TV leaflet and chordae tendineae geometries.... 34

Figure 3-3: (a) FE simulation setup of a equibiaxial displacement problem to validate the implementation of the VUMAT subroutine. (b) Comparison between the analytical solutions and the FE simulation results. 36

Figure 3-4: Boundary and loading conditions for the FE simulation of the TV systolic closure. 38

Figure 3-5: Resulting closed TV geometry from the FE simulation..... 40

Figure 3-6: (a) Illustration of the three slices made for viewing the TV coaptation, and (b) visualization from above the TV of the leaflet coaptation at the three locations. 41

Figure 3-7: (a) Illustration of the three slices per coaptation between two leaflets, and (b)

definition of geometrical values for each slice. (CVAP: Cut View Anterior-Posterior, CVAS: Cut View Anterior Septal, CVPS: Cut View Posterior Septal). 42

Figure 3-8: (a) Representative slice views for each coaptation for the healthy simulation and (b) the corresponding quantitative values for each view in (a). 43

Figure 3-9: Quantitative geometrical values for each cut view (cf. Figure 3-7) of each coaptation between two leaflets. 45

Figure 3-10: The von Mises stress contour of the closed TV geometry obtained from the FE simulation. 46

Figure 3-11: Maximum in-plane Green strain contour of the closed TV geometry obtained from the FE simulation. 47

Figure 4-1: The saddle annulus shape (*left*) and the flattened annulus shape (*right*) considered in the FE simulations. 52

Figure 4-2: Schematic of the uniform AD scenario (*left*) and the clinically-observed non-uniform AD scenario (*right*). 53

Figure 4-3: Two scenarios for the PM displacement: the longitudinal displacement perpendicular to the septum line (*left*), and the apical displacement towards the apex of the heart (*right*). 56

Figure 4-4: Definition of the eleven chordae tendineae groups. 57

Figure 4-5: Comaprison of the minimum, maximum, and mean stress and strain values for all pathological study scenarios. 59

Figure 4-6: Results of the pathological FE simulations for the saddle annulus configuration (*top*) and flat annulus configuration (*bottom*). 60

Figure 4-7: Results showing the incremental effects of (a) PH, (b) AD, (c) PM displacement – saddle annulus, and (d) PM displacement – flat annulus on the average von Mises stress (*left*) and the average maximum principle Green strain (*right*). S: saddle annulus; F: flattened annulus. 62

Figure 4-8: Comparison of the predicted PM tip reaction forces for various pathological study scenarios. 63

Figure 4-9: Cut-view results for all pathological scenarios considering the saddle annulus configuration. CVAP: cut view anterior-posterior; CVAS: cut view anterior-septal; CVPS: cut view posterior-septal. 65

Figure 4-10: Cut-view results for all pathological scenarios considering the flat annulus configuration. CVAP: cut view anterior-posterior; CVAS: cut view anterior-septal; CVPS: cut view posterior-septal. 67

Figure 4-11: (a) Overhead view and (b) angled view of the five chordae rupture scenarios resulting in leaflet prolapse with comparison to the healthy simulation result. 68

Figure 5-1: (a) Anatomy of the TV highlighting the three leaflets, (b) an illustration of leaflet segmentation for the baseline and GAG contribution investigations, and (c) an illustration of the six smaller sections excised for the regional variations investigation. Images were adapted from [59, 82]. 73

Figure 5-2: (a) CellScale BioTester system, (b) TV leaflet tissue mounted to the BioTester, (c) an illustration of the mounted tissue showing the four fiducial markers, and (d) a schematic of the extensive biaxial testing framework. Images were adapted from [59]. 74

Figure 5-3: (a) An illustration of the six smaller tissue sections that are mounted to the BioTester, and (b) a schematic of the biaxial testing and stress relaxation testing. Images were adapted from [82]..... 76

Figure 5-4: Baseline biaxial mechanical characterization results for the (a) TVAL, (b) TVPL, and (c) TVSL. * denotes statistically significant. Images were adapted from [59]. 81

Figure 5-5: Representative biaxial mechanical characterization results demonstrating the effect of loading rate on the (a) TVAL, (b) TVPL, and (c) TVSL mechanical response. Images were adapted from [59]. 82

Figure 5-6: Representative biaxial mechanical characterization results demonstrating the effect of temperature on the (a) TVAL, (b) TVPL, and (c) TVSL mechanical response. Images were adapted from [59]. 83

Figure 5-7: Biaxial mechanical characterization results demonstrating the tissue response of two different species (porcine and ovine) and two different age groups (juvenile and adult). Images were adapted from [59]. 84

Figure 5-8: Biaxial mechanical characterization results for the six smaller tissue regions of the TVAL. N.S. denotes not significant. Images were adapted from [82]. 85

Figure 5-9: Stress relaxation testing results for the six smaller regions of the TVAL. Image were adapted from [82]. 86

Figure 5-10: Alcian blue-stained histological images demonstrating the progression of the GAG constituent removal associated with various enzyme treatment durations. Scale bar = 100 μm. 87

Figure 5-11: Biaxial mechanical characterization results of the GAG contribution investigation for the TVAL in the circumferential and radial directions. N.S. denotes staistically non-significant, and * denotes statistically significant. Images were adapted from [115]. 88

Figure 5-12: Stress relaxation testing results of the GAG contribution study for the TVAL in the circumferential and radial directions. ** denotes nearly statistically significant ($0.05<p<0.10$). Images were adapted from [115]. 89

Figure 6-1: Schematic of the constitutive modeling framework..... 97

Figure 6-2: Schematic of the two-step differential evolution optimization algorithm. Image was adopted from [151]. 100

Figure 6-3: Predictions (dots) of the experimental data (shapes) using the Lee *et al.* model for the (a) TVAL, (b) TVPL, and (c) TVSL tissues using model parameters obtained from the training with *all biaxial mechanical data*..... 103

Figure 6-4: Predictions (dots) of the experimental data (shapes) using the Lee *et al.* model for the (a) TVAL, (b) TVPL, and (c) TVSL tissues using model parameters obtained from the training with *only the pure shear data*. 104

Figure 6-5: Predictions (dots) of the experimental data (shapes) using the Fung-type model for the (a) TVAL, (b) TVPL, and (c) TVSL considering model parameters obtained from the training with *all the biaxial loading protocols*..... 105

Figure 6-6: Predictions (dots) of the experimental data (shapes) using the Fung-type model for the (a) TVAL, (b) TVPL, and (c) TVSL considering model parameters obtained from the training with *only the pure shear loading protocols*.... 106

Figure C-1: Experimental photos of porcine hearts retrieved from a local slaughterhouse:

(a) whole heart is rinsed of blood with PBS solution; (b) a cut is made between the atria and ventricle to reveal both the mitral and tricuspid valves; and (c) blood clots are then removed from the heart before storage. 126

Figure C-2: Experimental photos of the opened porcine heart revealing the tricuspid valve with the anterior leaflet (TVAL), posterior leaflet (TVPL), and septal leaflet (TVSL). 127

Figure C-3: The (a) bulk leaflet is sectioned into a (b) 10 x 10 mm testing region (radial direction noted by surgical pen markers). (c) The leaflet thickness is measured. Specimens are mounted to (d) the biaxial testing system by (e) piercing the tissue with metal tines. After mounting, (f) fiducial markers are glued onto the surface of the tissue before (g) submersion in PBS solution at 37 °C. 128

Figure C-4: The preconditioning protocol is created by setting (a) the protocol name, (b) the testing control mode and force in the *X*-axis, (c) the preload conditions, (d) the *Y*-axis parameters to be the same as in the *X*-axis, and (e) the cycle parameters. 131

Figure C-5: The timing step requires (a) moving the tissue from the post preconditioning deformation to the peak membrane tension (and corresponding peak deformation) while simultaneously starting a stopwatch to record the stretch time. When the target force has been reached, (b) the post-preconditioning deformation is recorded. 132

Figure C-6: Schematic of the force-controlled biaxial testing protocols. 134

Figure C-7: Schematic of the displacement-controlled biaxial testing protocols. 136

Figure C-8: Schematic illustration of the stress relaxation testing protocol. 139

Figure C-9: Representative images illustrating the tracking of the coordinates of four fiducial markers during biaxial mechanical testing using a data image correlation (DIC) technique: (a) the tissue mounting configuration, (b) the configuration after the preconditioning step, and (c) the deformed configuration associated with the tissue specimen under mechanical loading. 141

List of Tables

Table 3-1: Numerical values for the anatomical dimensions used in the geometry creation. 32

Table 5-1: Percentage of glycosaminoglycans in the control and enzyme-treated tissue strips over a 160-minute treatment time. All quantities are reported as mean ± SEM. 88

Table A-1: Description of the abbreviations used throughout the Thesis. 115

Table C-1: Full testing parameters for all protocols of the force-controlled testing scheme. 135

Table C-2: Full testing parameters for all protocols of the displacement-controlled testing scheme..... 138

Acknowledgments

First of all, I would like to extend my sincerest gratitude to Dr. Chung-Hao Lee for providing me with this wonderful research opportunity. Throughout the last two years, he has devoted tremendous efforts and time guiding me towards my career goals and aspirations. This invaluable support and his broad knowledge of biomechanics has made this Thesis research possible, and I am grateful to continue the Ph.D. portion of my research journey under his mentorship and guidance.

I would also like to express my sincerest gratitude to my Thesis committee members: Dr. Zahed Siddique, Dr. Kuang-Hua Chang, Dr. Handan Acar, and Dr. Ryan Baumwart. Your mentorship, guidance, and collaborations throughout my time at the University of Oklahoma have significantly enhanced my experience. Additionally, I am grateful for your time, considerations, and suggestions for my Thesis work.

The countless hours in the lab and student office have been blessed by the friendships I have formed. It has been a great pleasure growing with my M.S. “brothers” Samuel Jett and Robert Kunkel—we finally made it! In addition, the countless others who I have grown close with throughout my time: Katherine Kramer, Colton Ross, Cortland Johns, Grace Duginski, among many others.

Finally, my sincerest thank you to my parents Shannon and Lisa, my sister Keely, my roommates Lawrence and Jonathan, and my close friends Dillon and Jordan. Your support and encouragement have eased my mind along this journey.

Thank you.

Abstract of the Thesis

Investigations of the Tricuspid Heart Valve Function: An Integrated Computational-Experimental Approach

by

Devin William Laurence

Master of Science in Mechanical Engineering

University of Oklahoma, Norman, OK, 2019

Dr. Chung-Hao Lee, Chair

The objective of this research is to employ both *in silico* modeling and *in vitro* experimental characterization methods to enhance the understanding of the biomechanical function of the tricuspid heart valve.

A finite element (FE)-based computational model of the tricuspid valve (TV) is first developed. Specifically, the geometry used in this computational model is based on parametric representations of the TV leaflets from porcine and ovine hearts and a parametric representation of the chordae tendineae. A nonlinear, isotropic constitutive model is used to describe of the mechanical behaviors of the TV leaflets, while the TV

chordae tendineae are modeled as a nonlinear, elastic solid.

The developed FE model of the TV apparatus is then used to simulate various pathological states including: (i) pulmonary hypertension, (ii) TV annulus dilation, (iii) papillary muscle displacement associated with right ventricular enlargement, (iv) flattening of the TV annulus, and (v) the rupture of the TV chordae tendineae. Numerical results from this study, as compared to available clinical observations, suggest that the TV annulus dilation and papillary muscle displacement resulting from right ventricular enlargement are key contributors to TV regurgitation. On the other hand, pulmonary hypertension resulted in the largest increase in TV leaflet stress (+65%) indicating pulmonary hypertension may be a key contributor to the adverse remodeling of the leaflet and myocardium tissues. In addition, the simulations of the chordae rupture scenarios reveal that those chordae tendineae attached to the TV anterior and septal leaflets may be more important to preventing TV leaflet prolapse.

Extensive biaxial mechanical testing of the TV leaflets is conducted to expand on the limited number of mechanical characterizations of the TV leaflets. These experimental efforts include: (i) a quantification of the TV leaflets' biaxial mechanical responses, (ii) an investigation of the loading-rate and temperature effects on the TV leaflet tissue mechanics, (iii) an examination of the influence of species and aging on the TV leaflet's mechanical properties, (iv) an evaluation of the spatial variations of the TV leaflet's tissue mechanics, and (v) a determination of the contribution of the glycosaminoglycans (GAGs) to the TV leaflet's mechanical responses. These *in vitro* experimental results suggest that (i) the TV

leaflets are more extensible than the mitral valve leaflets, (ii) the TV leaflets' responses depend slightly on the loading rate and temperature, (iii) the mechanical responses of the TV leaflets become stiffer with aging (+3.5%-6.1%), (iv) the TV leaflets exhibit spatial variance in the mechanical properties, and (v) the removal of the GAGs leads to an increased extensibility of the TV leaflets (+4.7%-7.6%).

Finally, a constitutive modeling framework, based on the hyperelasticity theory, is formulated to describe the mechanical behaviors of the heart valve leaflets from the acquired biaxial mechanical data. Through the differential evolution optimization, model parameters of two strain energy density functions commonly adopted in the soft tissue biomechanics society are estimated by fitting to the representative biaxial mechanical testing data. Results from this numerical study suggest that a refined strain energy density function may be warranted, as part of the future extensions, to fully capture the complex mechanical responses of the heart valve leaflet, especially under combined tensile and compressive loading.

CHAPTER 1 Introduction

1.1 Motivation

The tricuspid valve (TV) is an important component of the heart, which regulates the unidirectional blood flow between the right atrium (RA) and the right ventricle (RV). Specifically, the TV allows blood flow from the RA to the RV during diastole (*relaxation of the heart*) and then prevents the blood backflow into the RA during systole (*contraction of the RV*). Alterations to the anatomy or the sub-valvular components of the TV can result in regurgitation as the RV contracts. This regurgitant blood flow is undesired and often leads to a cascade of myocardium tissue growth and remodeling that may eventually lead to heart failure. Therefore, timely surgical intervention based on the fundamental understanding of TV pathologies is essential to the improvement of patient's survivability and the enhancement of the quality of life.

Functional tricuspid regurgitation (FTR) has been historically under-diagnosed and surgically ignored due to the pervasive expectation among surgeons and cardiologists that the FTR would be naturally resolved after correction of left-sided cardiac lesions. However, a recent study by Dreyfus *et al.* in 2005 [33] showed that FTR typically does not regress after successful surgical treatment of left-sided valvular heart disease and untreated FTR frequently progresses to late-severe FTR that further worsens long-term prognosis. Since this seminal clinical study, basic and clinical research for the TV has received more attention but is still very lacking compared to the mitral valve (MV) or the aortic valve

(AV). For example, studies exist for the MV or the AV that experimentally quantified the viscoelastic nature of the valve leaflet [46, 47, 131], the mechanical properties of the distinct tissue layers [132], and the contribution of the glycosaminoglycans (GAGs) to the valve leaflet tissue's mechanical responses [34]. Moreover, computer simulation studies have been developed for the MV for investigating the effects of selected constitutive models on the MV's closing behavior [85], as well as for evaluating the effects of surgical intervention on the overall valve's function [83]. Extensions of these ideas to the TV are critical to enhancing the current understanding of the TV function in both the healthy and diseased states.

1.2 Objective and Scope

The objective of this research is three-fold: (i) to develop a finite element (FE)-based computational modeling framework for investigating the biomechanical function of the TV, (ii) to characterize the mechanical properties of the TV leaflets, and (iii) to develop a constitutive model specific for describing the mechanical behaviors of the TV leaflets. The developments of this research are summarized as follows:

(1) *Development of a FE model for the TV*

In this work, a FE model of the TV has been created to simulate the TV systolic closure. The geometry of this FE model was created from a combination of a cubic B-spline representation for porcine TV leaflets and annulus, together with a

parametric representation of the TV chordae tendineae. The material model was selected to be nonlinear and transversely isotropic based on previous investigations for the TV. Clamped boundary condition for the TV annulus and papillary muscles (PMs) and transvalvular pressure loading condition were applied to mimic the physiological function of the TV, with a specific focus on the dynamic closure of the TV.

(2) *Numerical investigation of the diseased TV function based on in silico modeling*

The FE model developed in Research Task (1) was utilized to simulate various diseased scenarios, typically associated with FTR. The specific scenarios of interest were: (i) pulmonary hypertension, (ii) TV annulus dilation, (iii) PM displacements associated with the RV enlargement, (iv) flattening of the TV annulus, and (v) the rupture of the TV chordae tendineae. Results from this numerical study provide a systematic evaluation of the pathological TV biomechanical function, based on mechanics-related indices (such as tissue's stresses and strains) and clinically-relevant metrics (such as the tenting height and coaptation height).

(3) *Biaxial mechanical characterizations of the TV leaflets*

Similar methods to those previously used for the AV and MV leaflet tissues were applied to the TV leaflets to extensively quantify the biaxial mechanical properties. Specific investigations included: (i) a quantification of the TV leaflets' biaxial

mechanical responses, (ii) an investigation of the loading-rate and temperature effects on the TV leaflet tissue mechanics, (iii) an examination of the influence of species and aging on the TV leaflets' mechanical properties, (iv) an evaluation of the spatial variations in the TV leaflets' tissue mechanics, and (v) a determination of the contribution of GAGs to the TV leaflets' mechanical responses.

(4) *Development of a constitutive model for the TV leaflets' mechanical properties*

A constitutive modeling framework based on the hyperelasticity theory was developed for determining optimal constitutive model parameters for the acquired experimental data. The parameter estimation used a differential evolution optimization (DEO) algorithm tailored to the known shape of the search space. This constitutive modeling framework was used to investigate two common strain energy density functions to demonstrate how well they can model some of the extensive biaxial mechanical data acquired in our laboratory.

The remainder of this thesis is organized as follows. In Chapter 2, a literature review of topics relevant to the TV is presented. Specifically, the TV anatomy and function, FTR, clinical assessment and treatment of FTR, biaxial mechanical characterization methods, constitutive modeling of soft tissue mechanical response under the hyperelasticity framework, and computational modeling of heart valve function. Chapter 3 presents the developed FE-based computational modeling framework to simulate the healthy TV's systolic closure. Then, Chapter 4 presents the application of the developed FE-based

computational model to the investigations of the TV under various pathological conditions. Biaxial mechanical characterizations of the atrioventricular heart valve leaflets are presented in Chapter 5. In Chapter 6, the developed constitutive modeling framework, which utilizes the acquired experimental mechanical data to represent the TV leaflets' mechanical properties, is presented. Finally, Chapter 7 provides concluding remarks and suggested future extensions.

CHAPTER 2 Literature Review

2.1 Overview of the Tricuspid Valve Anatomy and Function

2.1.1 The Tricuspid Valve Anatomy

The TV is a complex structure located between the RA and RV of the heart (Figure 2-1a). Due to its anatomical location between the RA and RV, the TV is also commonly referred to as an atrioventricular heart valve (AHV) alongside the MV in the left side of the heart. The TV has three thin tissue leaflets known, based on their anatomical location, as the anterior leaflet (TVAL), posterior leaflet (TVPL), and septal leaflet (TVSL) (Figure 2-1b). Natural boundaries between the leaflets are formed by the commissures found where the leaflet free edge becomes closest to the valvular annulus. The TV leaflets are affixed to the heart via the rigid, ring-like valvular annulus. Additionally, the leaflets are attached to the chordae tendineae that anchor the leaflets to the PMs located on the RV wall. Each sub-valvular component has its own distinct properties further described in the following paragraphs.

The TV leaflets are known to have varying dimensions based on the leaflet and the region of the leaflet. A study by Khoiy *et al*. (2016) [65] measured the thickness of porcine TV leaflets and observed the TVSL was the thickest leaflet (491 ± 49 μm) followed by the TVPL (346 ± 61 μm) and the TVAL (313 ± 68 μm). The study by Stevanella *et al.* (2010) [135] showed that the porcine TV leaflet thickness values were comparable to measurements of human TV leaflet thicknesses.

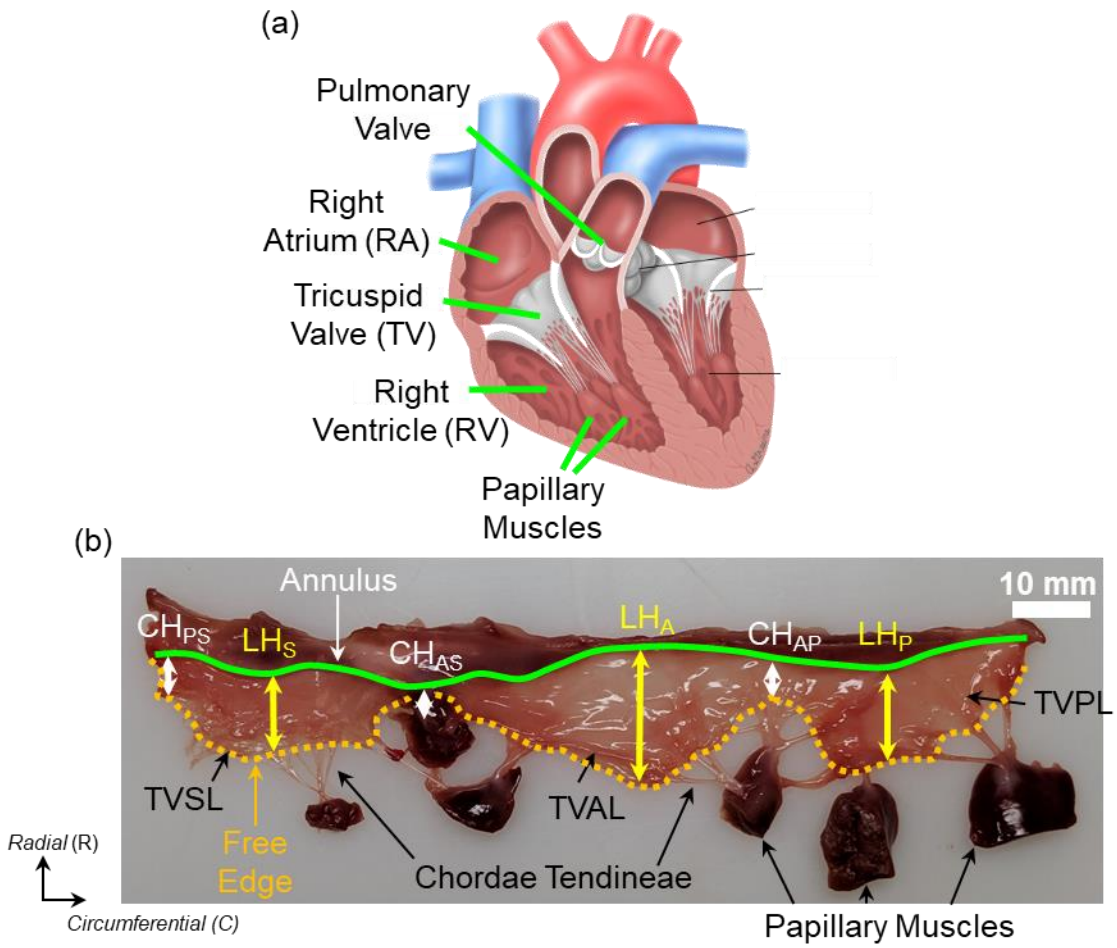

Figure 2-1: (a) Schematic of the TV within the heart chambers (image adapted from uptodate.com). (b) Excised porcine heart showing the key components of the TV, including the TV leaflets, annulus, and the chordae tendineae.

It has also been shown for the AV leaflets that the thicknesses vary regionally throughout the leaflet [23, 122], so it is reasonable to assume a similar regional variance is present for the TV leaflets. Moreover, Stevanella *et al.* (2010) [135] also quantified the leaflet heights (Figure 2-1b) for porcine hearts and showed that the TVAL had the largest leaflet height (19.93 ± 3.53 mm), followed by the TVSL (18.82 ± 3.22 mm) and the TVSL (18.62 ± 4.08 mm).

As previously discussed, the TV annulus is the ring-like structure to which the TV leaflets are affixed. *Ex vivo* studies for porcine hearts have shown that in the non-contracted state, the TV annulus has a circumference of 12.5 ± 1.5 cm and area of 11.4 ± 2.8 cm^2 [66]. The TV annulus' three-dimensional (3D) shape does not lie within one plane, rather it has a distinct saddle-like shape with clear high and low points. A study by Fukuda *et al.* (2006) [40] used real-time 3D echocardiography imaging to acquire the average TV annulus geometry for 15 healthy human patients (Figure 2-2). As illustrated in Figure 2-2, the authors observed distinct high points located between the TVAL and TVPL and between the TVAL and TVSL. Interestingly, the same study by Fukuda *et al.* (2006) also showed that, despite contracting, the TV annulus maintains this saddle-shape configuration throughout the cardiac cycle.

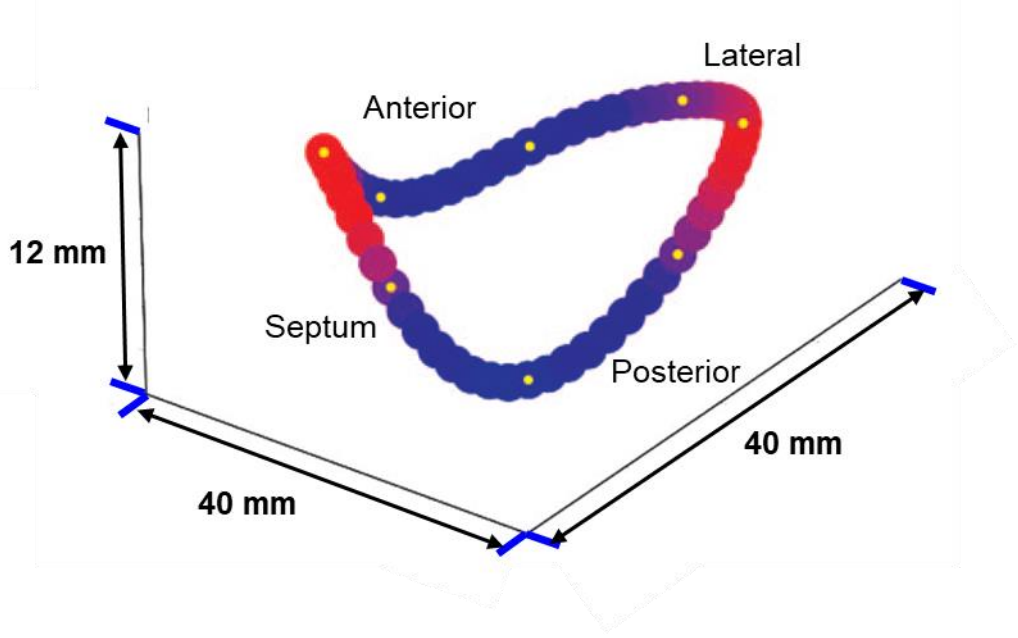

Figure 2-2: Annuloplasty ring for the TV shape, demonstrating a clear saddle-shaped TV annulus. Image was adapted from [40].

The chordae tendineae are string-like tissues with one end attaching to the ventricular side of the leaflets and the other end attaching to the PMs located on the RV wall (cf. Figure 2-1a). The seminal study by Silver *et al.* (1971) [124] provided the now commonly-used classification scheme for the TV chordae tendineae. In brief, the two thickest chordae tendineae attached to each leaflet are classified as *strut chordae*, the chordae tendineae attached near the leaflet free margin are classified as *marginal chordae*, and the chordae tendineae attached near the leaflet base are classified as the *basal chordae*. A recent morphological characterization of the chordae tendineae [110] revealed that the strut chordae were the thickest and longest chordae (Figure 2-3).

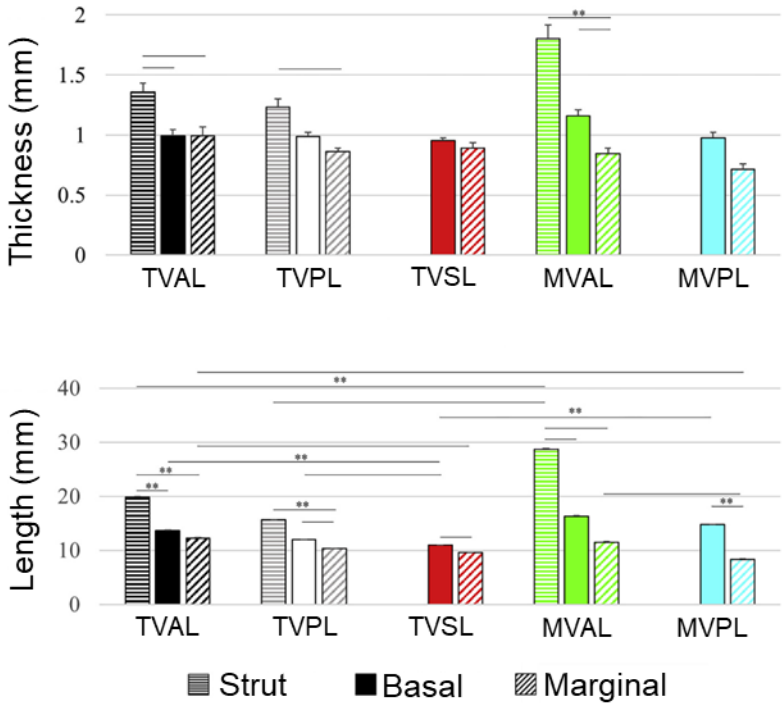

Figure 2-3: Average chordae tendineae thickness (*top*) and length (*bottom*) for each classification and each leaflet (MVAL: MV anterior leaflet, MVPL: MV posterior leaflet). Values are reported as mean ± the standard error of the mean (SEM). A horizontal bar denotes $p<0.01$, ** denotes $p<0.001$. Image was adapted from [110].

2.1.2 Tricuspid Valve Organ-Level Function

The primary function of the TV is to help facilitate the unidirectional flow of blood through the heart. During diastole, blood passes from the RA into the RV through the TV. Then, as the RV contracts during systole, the TV closes to prevent the backflow of blood into the RA. The TV leaflets are one of the sub-valvular components responsible for completely sealing the RA/RV orifice and preventing the blood backflow. The chordae tendineae aide in the closure of the TV leaflets by anchoring the leaflets to the PMs on the RV wall, thus preventing TV leaflet prolapse into the RA. The TV annulus provides a hinge point for the leaflets as they close and is known to contract similar to the RV. Modifications to the structure or function of these sub-valvular components can result in failed leaflet closure and allow for the backflow of blood into the RA. This backflow of blood, namely TV regurgitation, is further described in Section 2.2.

2.1.3 Microstructure of The Tricuspid Valve Leaflet

The TV leaflets have a complex microstructure consisting of distinct tissue layers and constituents. The first tissue layer closest to the atrium is the *atrialis*, followed by the *spongiosa*, the *fibrosa*, and the *ventricularis* (Figure 2-4). The atrialis and ventricularis layers are generally the thinnest of the four layers, whereas the fibrosa and spongiosa layers compose the majority of the tissue thickness.

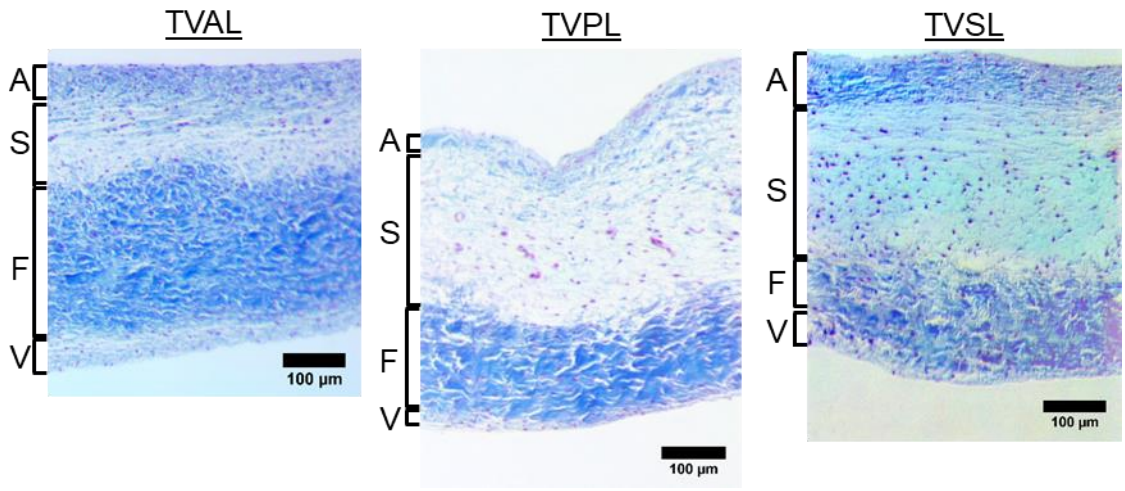

Figure 2-4: Histological images using Masson's Trichrome staining, illustrating the microstructure (dark blue: collagen fibers, black: nuclei, and red: cytoplasm) and layers (A: atrialis, S: spongiosa, F: fibrosa, and V: ventricularis) of the TV leaflets. Image was adapted from [59].

The TV leaflet tissues can be stained with Movat's Pentachrome using histological methods to reveal the collagen fibers, elastin fibers, the valvular interstitial cells (VICs), and the non-fibrous ground substance (Figure 2-5). With respect to the four tissue layers, the fibrosa is generally composed of collagen fibers, the atrialis and ventricularis are primarily elastin fibers, and the spongiosa is mostly GAGs, while the VICs are dispersed throughout the entire tissue. The collagen fibers have been hypothesized to be the primary load-bearing component for the AV contributing primarily in the leaflet's circumferential direction (cf. Figure 2-1b) [76, 121, 152]. On the other hand, the elastin fibers are believed to largely contribute to deformations in the radial direction [29, 30, 132]. Meanwhile, the GAGs have been shown to help with the timely recruitment of the collagen fibers in the arterial tissues [34, 89]. The VICs of the mitral valve have been shown to contribute to the active remodeling of the tissue in pathophysiological conditions [7, 10, 48, 78, 93].

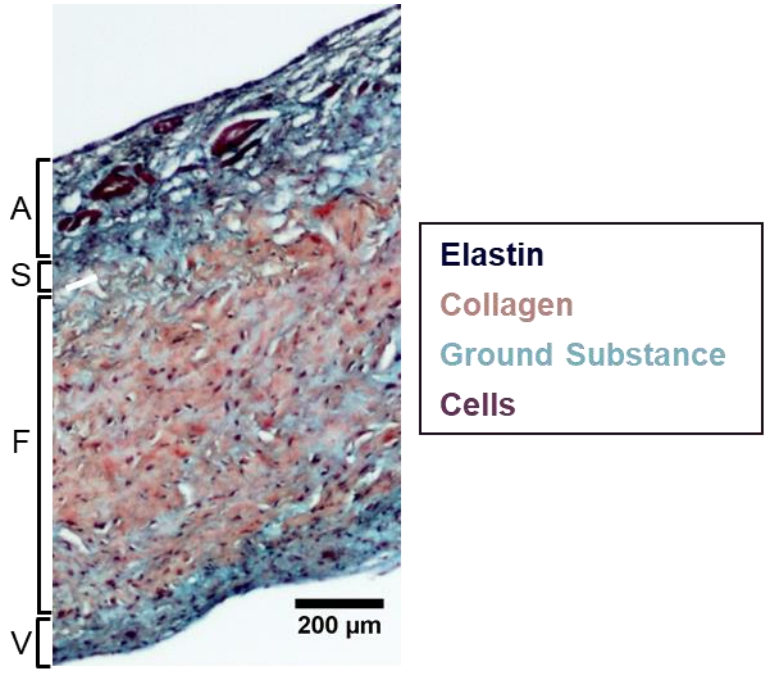

Figure 2-5: Movat's Pentachrome histological staining of the TVAL tissue, showing the complex microstructure. Image was adopted from [72].

2.2 Overview of Tricuspid Regurgitation

2.2.1 Tricuspid Regurgitation

Tricuspid regurgitation (TR) occurs when the TV leaflets are unable to fully close and prevent the backflow of blood into the RA during systole. TR can be classified by etiology into two categories: primary (organic) TR and secondary (functional) TR [5, 9, 103]. The regurgitation is considered as primary TR when there is some type of structural abnormality or damage to the TV apparatus that is the primary cause of TR [5]. This category is composed of congenital diseases such as Ebstein's anomaly and acquired diseases such as tricuspid leaflet flail resulting from chordae rupture. On the other hand, TR is classified as

functional TR (FTR) when there is no damage to the TV apparatus itself, but instead the TR is secondary to some alteration to the surrounding heart geometry [5, 9, 138]. For this reason, FTR is sometimes also called secondary TR. Some examples of FTR include TR resulting from RV enlargement, TV annulus dilation (AD), or even pulmonary hypertension (PH) (cf. Table 2 from Anwar *et al.* [5]).

FTR often progresses from a combination of three interlinked pathologies that typically stem from a pressure or volume overload in the RV (e.g., PH) [8, 52, 129]. First, as a direct result of the pressure or volume overload, the RV will remodel and become enlarged beyond the physiological configuration [8, 52]. Early studies by Come *et al.* [26] observed an ~60% increase in RV diameter in patients with TR. Additionally, the annulus will primarily dilate away from the septum to form a more circular shape as compared to the healthy elliptical shape, and the annulus will lose its saddle-like configuration to become much flatter [127, 142]. These alterations will continue to worsen resulting in PM displacement, leaflet tethering, reduced coaptation of the leaflets, and the formation or worsening of FTR [8, 127, 129, 138, 142].

TR has been historically ignored in the clinical setting despite affecting approximately 1.6 million Americans [136, 141]. This largely stems from the initial clinical assumption that treatment of left-sided heart lesions will cause right-sided lesions to naturally regress [15]. However, a study by Dreyfus *et al.* [33] in 2005 showed that this assumption was invalid and FTR will continue to progress after treatment of left-sided lesions. Since the time of Dreyfus' seminal study, the TV has received more attention in the clinical and research

fields, but the MV and AV still compose the majority of existing heart valve research (Figure 2-6).

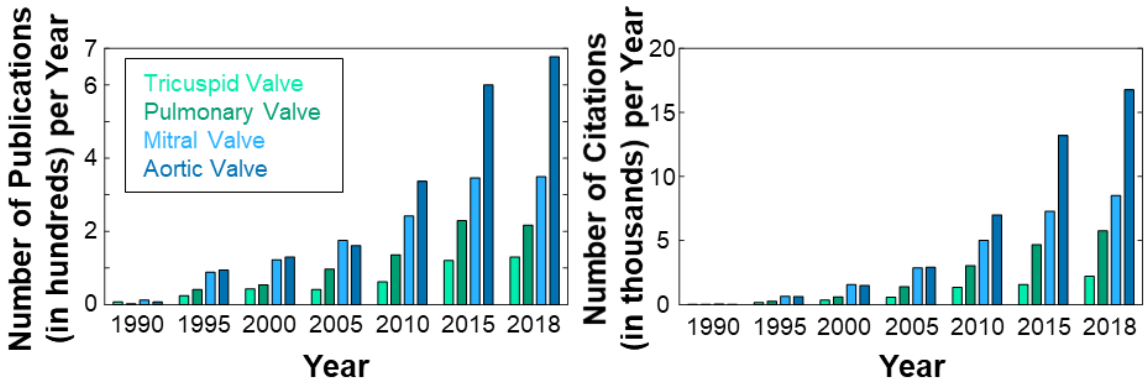

Figure 2-6: The number of publications (*left*) and number of total citations (*right*) since 1990 for the four heart valves. Data was adopted from *Web of Science*.

Furthermore, many questions still exist about the optimal time and methodology for treating the FTR [4, 18, 21, 31, 33, 99, 100, 114] and about how to mitigate the recurrence of TR after the surgical intervention [39, 40, 42, 68, 69, 88, 94, 104, 140]. As expected, there has been significant progress towards successfully answering these questions and improved patient-specific therapeutics. For example, recent clinical studies [9, 33, 40, 41] have worked towards better understanding the progression and proper assessment of FTR, *in vitro* and *in vivo* studies have worked towards quantifying relevant mechanical properties of the TV and its sub-valvular components (cf. Section 2.3), and more recently computational modeling studies have been explored to better understand aspects of the TV biomechanical function (cf. Section 2.5). Despite these recent strides towards improving the understanding of the TV function in healthy and pathophysiological states, gaps in the understanding the *underlying mechanisms* and *recurrence* of FTR still remain.

2.2.2 Clinical Assessment and Diagnosis

Clinicians rely on medical imaging modalities to accurately assess and diagnose TR. Several options exist for this application, such as echocardiography, magnetic resonance imaging (MRI) and computed tomography (CT). However, the most commonly used method is echocardiography with its many different classifications (e.g., transesophageal (TEE), transthoracic (TTE), 2D, 3D, etc.) [79, 80]. Selection of echocardiography is largely due to its ability for rapid imaging of the cardiac structures and subsequent comprehensive evaluation of the valve function and potential regurgitation. More detailed information about using echocardiography for assessment and diagnosis of TV function and regurgitation is discussed as follows.

The most commonly used method of echocardiography in assessing TV function is 2D transthoracic echocardiography (2DTTE). 2DTTE allows for different visualizations of the TV, RA, and RV geometries such as the right ventricular inflow, apical four-chamber and parasternal short-axis views [1, 79, 80]. The essential difference between these methods is the placement of the echocardiography probe to reveal different perspectives of the heart geometry. For example, the apical four-chamber view entails placing the echocardiography probe near the apex of the heart to reveal the four chambers of the heart [36]. Interestingly, despite these 2DTTE views typically with defined probe placement based on external body landmarks, it has been shown that different combinations of the TV leaflets are possible within the 2D image (Figure 2-7) [1].

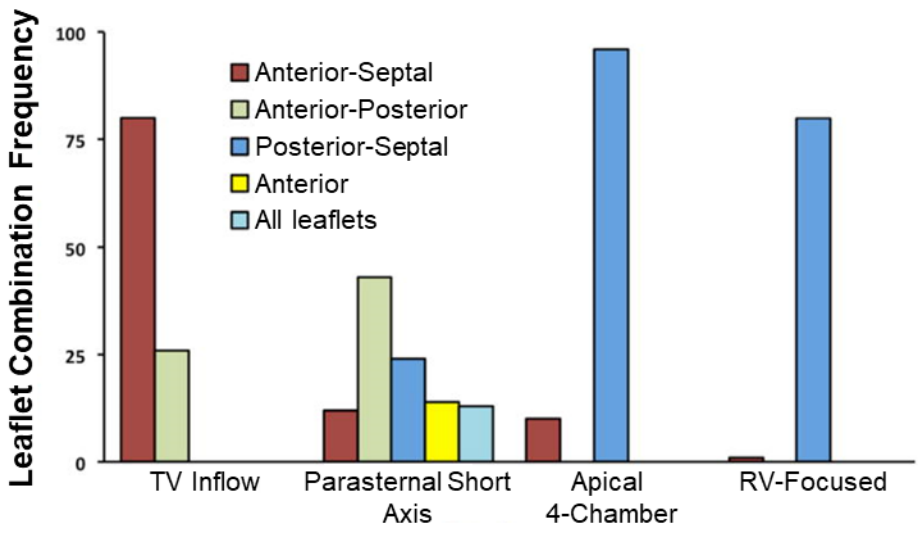

Figure 2-7: The observed probability that a leaflet combination appears on a given 2DTTE imaging perspective. Image was adapted from [1].

Additionally, these 2DTTE visualizations can be paired with color flow imaging methods (e.g., color flow Doppler) to reveal the potential regurgitant flow of blood through the TV (Figure 2-8). Although these color flow imaging methods can visualize different sizes or intensities of regurgitant flow, it is recommended to only use them for diagnosis of TR, rather than the assessment of the severity of TR. Instead, more quantitative metrics or values are typically used for determining the severity of TR. Clinicians can use 2DTTE with color flow Doppler imaging to perform *the flow convergence method* and visualize the proximal isovelocity surface area. It is suggested there is severe TR if there is a proximal isovelocity surface with a radius >9 mm and mild TR if the radius is <5 mm [79, 144]. As of 2010, this flow convergence method was the most popular quantitative method for determining MV regurgitation, but other methods did exist [79].

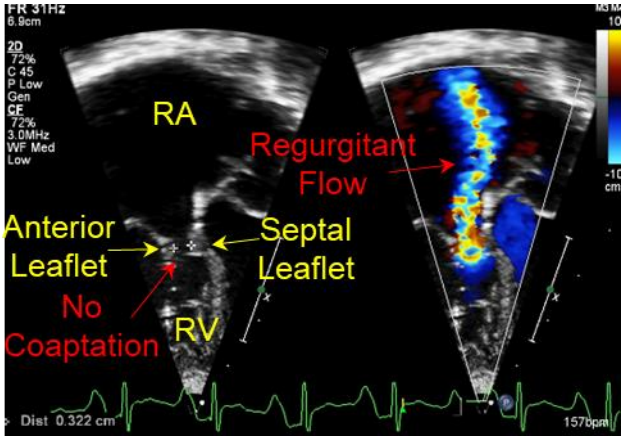

Figure 2-8: 2DTTE (*left*) and color Doppler imaging (*right*) of the four-chamber view of an infant patient with pulmonary atresia. Image courtesy of Children's Heart Center at the OU Health Sciences Center.

Some investigations suggest determining the size of the vena contracta of the TR (smallest diameter of the regurgitation through the TV) [143], evaluation of the blood flow through the hepatic vein [45, 98], or continuous wave Doppler of the TR jet. Despite the evolving methods for diagnosing and assessing TR, it is still an under-diagnosed problem. In 2016 it was shown that only 8,000 of the 1.6 million Americans affected by TR were surgically treated [136, 141]. Therefore, enhancements of existing methods or development of new, innovative diagnosis and assessment methods are required to fully meet the clinical needs.

2.2.3 Clinical Treatment of Tricuspid Regurgitation

Section 2.2.1 illustrated the continued worsening of TR if it remains untreated; thus, it is necessary to have effective clinical repair options to prevent this pathophysiological remodeling. Two common approaches for surgically treating FTR share the same philosophy of fixing the TV annulus in a contracted position to restore the full leaflet closure. The first method was introduced by Carpentier *et al.* (1971) [19] and involves

surgically suturing a soft-plastic annuloplasty ring to the TV annulus, whereas the second approach was introduced by De Vega *et al.* (1973) [28] and involves surgically placing a continuous suture (suture annuloplasty) on the TV annulus to constrict its dimensions. Both of these annuloplasty-based methods unfortunately suffer from a recurrence of the TR (~20%) approaching 5-10 years after the operation [11, 87, 111]. This suggests the annuloplasty-based methods do not fully address all of the needs for repairing the FTR, and the changes induced by fixing the annulus in a contracted position could alter the mechanical state of the valve in an undesired manner. In the scenario where the chordae tendineae have rupture resulting in flail or prolapse of the TV leaflets into the RA, other treatment methods are typically considered. These methods include: (i) replacing the damaged chordae tendineae with polytetrafluoroethylene-fabricated chordae tendineae, (ii) shortening the chordae to prevent flail/prolapse, and (iii) moving chordae tendineae from non-prolapsing TV leaflets to the prolapsing leaflet, among others. These procedures have had great results for operating on the MV chordae tendineae [109, 126, 128], but have their shortcomings such as mis-matching of mechanical properties with the native chordae or rupture of native chordae tendineae [24, 25, 139].

2.3 Mechanical Properties of the Heart Valve Leaflets

The mechanical properties of the heart valve leaflets provide insight into the function of the leaflet tissues and open the door for investigations in computational modeling and improved therapeutics. The MV and the AV have been the subject of most mechanical characterization papers, but the TV has started receiving more attention in the last decade.

This section will provide an overview of the major mechanical characterization studies for the MV and AV leaflets that eventually led to the recent studies for the TV. Then, those recent studies for the TV leaflet tissues are discussed.

2.3.1 The Mitral and Aortic Valve Leaflets

The early mechanical characterizations of the MV and AV leaflets were focused on determining the *uniaxial* mechanical properties (Figure 2-9). Early uniaxial tension studies for the MV and AV leaflets revealed a distinct, nonlinear, exponential-like response of the tissue [22, 95, 96, 123]. The study by Kunzelman *et al.* (1992) [74] found that the mechanical properties varied with orientation of the tested sample with the circumferential direction stiffer than the radial direction (i.e., the tissue was *anisotropic*). Later, the study by May-Newman *et al.* (1995) [90] quantified the mechanical properties of the MV leaflets under a *biaxial* tension protocol (Figure 2-10). Specifically, May-Newman *et al.* excised porcine MV leaflets that were then mounted to their biaxial testing system using a series of sutures attaching the four sides of the tissue structure to the system. Each tissue underwent 10 cycles of a biaxial testing protocol during which the tissue was cyclically loaded until it showed rapid stiffening. Afterwards, each tissue was also tested using a uniaxial testing protocol for comparisons. Results from their work (Figure 2-10) showed that there were distinct differences in the mechanical responses determined from the uniaxial and biaxial testing protocols.

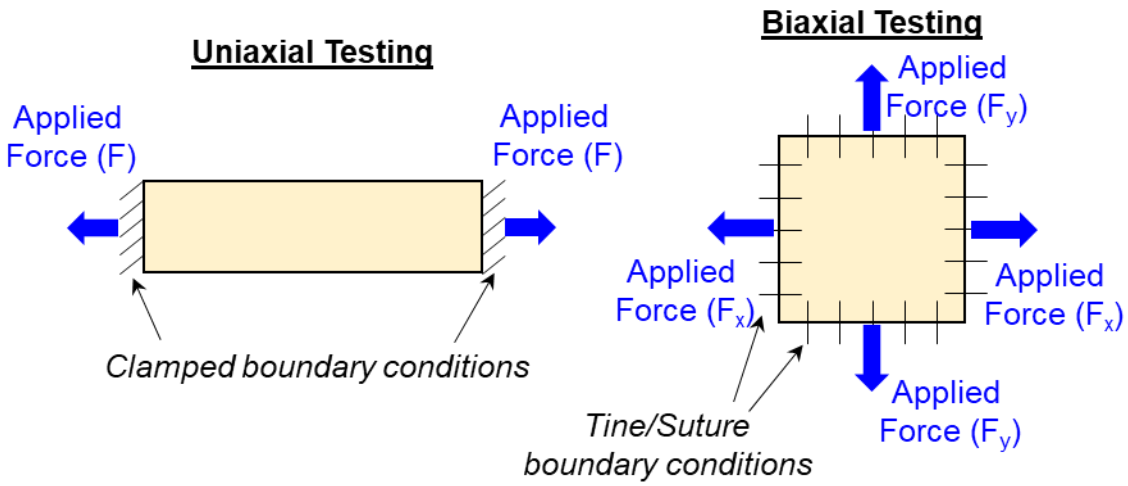

Figure 2-9: Schematic of the experimental setups of typical uniaxial testing (*left*) and biaxial testing (*right*).

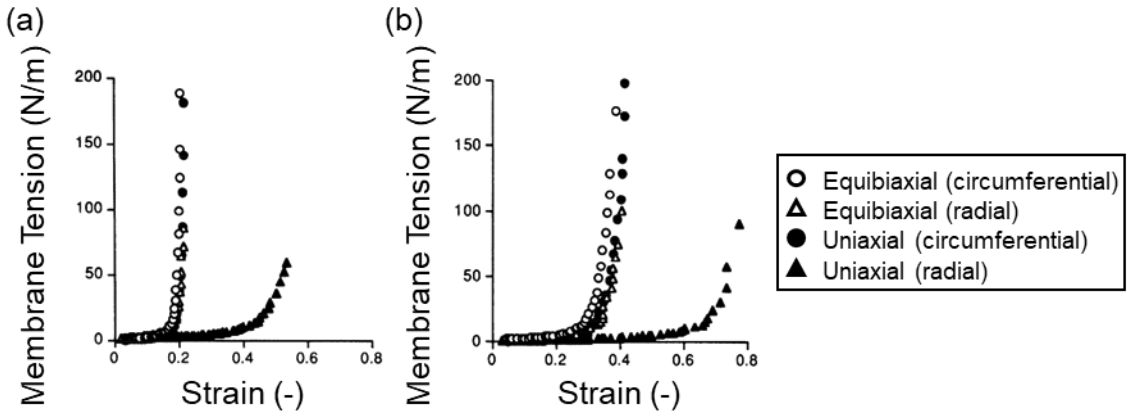

Figure 2-10: Comparison between the uniaxial and biaxial mechanical testing of the MV leaflet tissues. Images were modified from [90].

Under the biaxial testing scheme, the tissue was shown to have anisotropic properties with the circumferential direction stiffer, but the authors also observed some *coupling* between the mechanical response in the two tissue directions. This coupling effect was evident due to the circumferential loading of the tissue affecting the mechanical response in the radial direction (making it appear "stiffer"), but the converse was not true for the radial loading.

Since the time of May-Newman's seminal work on quantifying the biaxial mechanical properties of the MV leaflet tissues, the mechanical characterizations have focused on attempting to quantify certain key aspects of the tissues' mechanical responses. Grashow *et al.* (2006) [47] hypothesized that the MV tissues' mechanical response may depend on loading rate. Thus, they developed an experimental setup to examine the mechanical response of the MV anterior leaflet at varying strain rates (0.9-18 N/s) and demonstrated that the MV leaflet tissue showed minimal difference in its mechanical responses under varying loading rates. Later in 2006, Grashow *et al.* [46] also tested the stress-relaxation and creep behaviors of the MV leaflet tissues to further understand the viscoelastic properties. Interestingly, the results from this study showed that the MV tissues exhibit a clear stress relaxation behavior, but an almost negligible creep response. Meanwhile, Stella *et al.* (2007) [132] mechanically tested the individual layers of the AV leaflets and demonstrated that the ventricularis layer primarily contributed in the radial directions at higher stress levels while the fibrosa layer had a mechanical response that was similar to the intact tissue. More recently, a study by Eckert *et al.* (2013) [34] used an enzymatic degradation procedure to remove the GAGs from the AV leaflet tissues for subsequent mechanical testing. The results from this study interestingly noted that the GAGs appeared to not play a significant role in the biaxial mechanical properties of the AV leaflet tissues. Rather, the GAGs interact with the surrounding collagen fibers at low stresses and not once the fibers were fully straightened. These mechanical testing studies provided the heart valve biomechanics community with a wealth of information regarding the mechanical response of the *MV* and the *AV*.

2.3.2 The Tricuspid Valve Leaflets

While there have been several detailed experiments investigating the biaxial mechanical properties of the AV and MV leaflets, only three exist for the TV leaflets. The first study by Heyden *et al.* (2015) [51] provided a survey of the mechanical responses for all the four heart valves' leaflet tissues subject to uniaxial and biaxial mechanical testing. The stress-strain results from this study did not have the clear toe region in which large deformations correspond to a small increase in stress, nor do they have the clear transition from the low-stress toe region to the high-stress region. Nevertheless, this study was the first to provide mechanical characterizations for the TV leaflet tissues. The second study by Khoiy *et al.* (2016) [65] focused specifically on the TV leaflet tissues providing averaged biaxial mechanical data for 10 porcine hearts. The averaged data sets showed the nonlinear, anisotropic mechanical response with a clear toe region and transition point to the high-stress region for all tested loading ratios (Figure 2-11). Semi-quantitative comparisons were made between the three TV leaflets revealing that the TVAL and TVPL shared similar stiffnesses in the circumferential but not the radial direction. Also, the TVSL appeared to be the most compliant tissue in the circumferential direction but was only more compliant in the radial direction than the anterior leaflet. More recently, the study by Pham *et al.* (2017) [108] involved biaxial mechanical characterizations of TV leaflet tissues from 12 human hearts. Within this study, the authors were able to compare the mechanical response of the leaflet tissues from the four heart valves and revealed that the TV leaflets were the most extensible and isotropic. As previously stated, the mechanical characterization studies for the TV are significantly lacking compared to the MV or the AV.

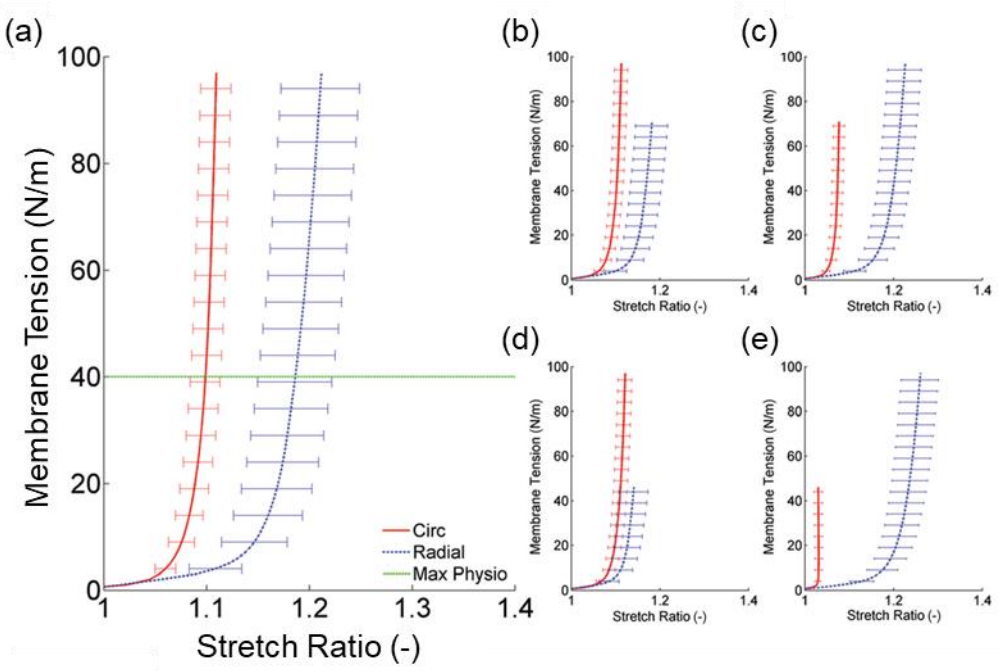

Figure 2-11: Representative data from [65] for the TVAL tissue under (a) the equibiaxial loading protocol (i.e., T_{circ}:T_{rad} = 1:1), (b) T_{circ}:T_{rad} = 1:0.75 loading protocol, (c) T_{circ}:T_{rad} = 0.75:1 loading protocol, (d) T_{circ}:T_{rad} = 1:0.5 loading protocol, and (e) T_{circ}:T_{rad} = 0.5:1 loading protocol.

2.4 Constitutive Modeling

Constitutive models provide a relationship between the stress and strain of a material. For the heart valve leaflets, these models are formulated under the hyperelasticity framework, in which a strain energy density function (SEDF) is defined for the material. The specific SEDF is then transformed to an expression relating the stress and strain that represents the mechanical response of the tissue. Numerous papers have worked towards formulating SEDFs that describe the complex mechanical response of the heart valve leaflets. These

studies take one of two methods for describing the mechanical response of the soft tissue. The first is a *phenomenological* modeling approach where the mechanical response of the tissue is represented by a series of arbitrary constants that may contain no inherent information about the material's mechanical properties. The second is a *microstructure-informed* modeling approach that is based on the response of each constituent to provide the bulk response.

2.4.1 Common Constitutive Models for the Heart Valves

The first study for the MV was by May-Newman and Yin (1998) [91] where they determined a functional form for the strain energy density of the leaflet tissues. Experimentally, the authors used a series of constant strain invariant biaxial mechanical tests to help determine the optimal form of the SEDF. Through this method, they arrived at a similar SEDF as the early works by Fung *et al.* (1979) [43], except using the invariants of the right Cauchy deformation tensor **C**:

$$W = c_0\left(\exp\left\{c_1(I_1-3)+c_2(\alpha-1)^4\right\}-1\right), \tag{2.1}$$

where $I_1 = trace(\mathbf{C})$ is the first strain invariant and $\alpha = \sqrt{I_4}$ is related to $I_4 = \mathbf{N}\bullet\mathbf{C}\bullet\mathbf{N}$, which is the fourth invariant of **C**, and c_0, c_1, and c_2 are material constants. Shortly thereafter, Holzapfel, Gasser, and Ogden (HGO) proposed a new SEDF for the arterial wall tissues that are analogous to the heart valve tissues [44, 54]:

$$W = \frac{c}{2}\left(I_1-3\right)+\frac{k_1}{2k_2}\left[\exp\left\{k_2\left[\kappa I_1+\left(1-3\kappa\right)I_{4i}-1\right]^2\right\}-1\right], \tag{2.2}$$

where c, k_1, and k_2 are the material constants, κ describes the alignment of the fibers (κ=0: well-aligned fibers; κ=1/3: randomly-aligned fibers), and i denotes the fiber family of

interest (*i*=1-2). Prot *et al.* (2007) [112] later proposed another SEDF for describing the biaxial mechanical properties of the MV leaflet tissues:

$$W = \mu\left(I_1 - 3\right) + c_0\left[\exp\left\{c_1\left(I_1 - 3\right)^2 + c_2\left(I_4 - 1\right)^4\right\} - 1\right], \tag{2.3}$$

where μ, c_0, c_1, c_2 are material constants. The most recent phenomenological model proposed for the heart valve leaflets came in the 2014 study by Lee *et al.* (2014) [83] and took the form:

$$W = C_{10}\left(I_1 - 3\right) + \frac{c_0}{2}\left\{\delta\exp\left[c_1\left(I_1 - 3\right)^2\right] + \left(1-\delta\right)\exp\left[c_2\left(I_4 - 1\right)^2\right] - 1\right\}, \tag{2.4}$$

in which C_{10}, c_0, c_1, and c_2 are material constants, and δ describes the alignment of the collagen fibers about the preferred orientation (δ=1 is purely isotropic; δ=0 is purely anisotropic).

On the other hand, the microstructure-informed constitutive models that have been used for the MV or AV leaflets [13, 35, 85, 152] can be summarized by the general form

$$\mathbf{S} = \int_{-\frac{\pi}{2}}^{\frac{\pi}{2}} \Gamma(\theta) S_f\left[E_f(\theta)\right]\mathbf{N}\otimes\mathbf{N}d\theta + \mu_m\left(\mathbf{I} - C_{33}\mathbf{C}^{-1}\right) . \tag{2.5}$$

Here, **S** is the second Piola-Kirchhoff stress tensor, $\Gamma(\theta)$ is the orientation distribution function for the fiber ensemble, S_f is the fiber ensemble stress that is a function of the fiber strain E_f, $\mathbf{N}(\theta)$ is a unit vector describing the preferred fiber orientation, μ_m is the elastic modulus of the matrix components, **I** is the second-order identity tensor, and **C** is the right-Cauchy deformation tensor. This constitutive model can generally provide very accurate representations of the leaflets' mechanical responses [13, 35, 85, 152], but it is computationally expensive compared to the phenomenological approaches.

2.5 Computational Modeling of the Heart Valve Function

Computational models provide an exciting avenue of combining the information presented in this Chapter to predict the heart valve dynamic function. The first 3D FE model for the MV was reported over two decades ago in a study by Kunzelman *et al.* (1993) [75], whereas the first AV FE model was developed over three decades ago by Hamid *et al.* (1987) [50]. These early numerical studies contained many assumptions regarding the leaflet's material and geometrical properties that have since been addressed. For example, Kunzelman's paper for the MV described the anisotropy of the tissue by increasing the Young's modulus in one direction; in contrast, more recent MV computational models have fully-mapped, regionally-varying fiber architectures with complex constitutive models to more realistically represent the valve's function [83, 85, 113]. Kunzelman's early study also utilized an idealized representation of a porcine MV while a recent study by Wang and Sun (2013) [147] modeled a patient-specific MV geometry from clinical CT-sliced image data. Additionally, fluid-structure interaction (FSI) models have since been utilized for more accurate predictions of the MV [77, 81], AV [27], or bioprosthetic valve [57, 61] closure. These advances are closely mirrored for the AV with the development of a structural constitutive model [13], patient-specific modeling [97, 146], and the FSI models [27, 49, 102]. Nevertheless, as emphasized throughout this chapter, the TV has received far less attention compared to the MV and TV resulting in a significant disparity in current computational modeling work.

2.5.1 Computational Models of the Tricuspid Valve

The *first* bio-solid model published for the TV was from Stevanella *et al.* (2010) [135]. The authors used a parametric representation of the *ex vivo* TV geometry that was subsequently discretized into an FE-suitable mesh. The leaflets were represented by 40,300 three-node triangular plane-stress shell elements and the chordae tendineae were represented by a series of two-node truss elements. To simulate valvular closure, Stevanella *et al.* prescribed a time-dependent physiological pressure traction to the ventricular side of the leaflets while the annulus contracted in accordance with previous values [53]. These simulations were performed using the commercial ABAQUS/Explicit dynamic FE software package. Results from the FE model showed stress values less than 100 kPa, peak strains of ~52%, and PM forces ranging from 0.37-0.75 N. It should be noted that these simulations used material properties for the MV leaflets, so the mechanical values may not be representative of the TV mechanical values.

The next study for computationally modeling the TV came seven years later in Aversa and Careddu (2017) [6]. In this study, the authors took a different approach than Stevanella's study and used *3DE imaging data to inform their bio-solid model geometry*. The FE mesh consisted of three-node triangular plane-stress shell elements for the TV leaflets and a series of truss elements to represent the chordae. For simulating TV closure, a time-dependent pressure traction was applied to the ventricular surface, the annulus was prescribed to contract based on their *in vitro* measurements, and the PMs were assumed to have no rigid body motion. Results of their FE model showed an incomplete closure of the TV leaflets at peak systole although the previous model by Stevanella *et al.* (2010) properly

showed leaflet closure. Furthermore, the stress and strain results were irregular with belly stress values near 300 kPa and peak strains of 0.4 occurring near the chordal attachments. Aversa and Careddu suggested these observations were due to the inability to properly define the free margin and commissures of the leaflet, thus causing the chordae to not behave in the proper manner.

Kamensky *et al.* (2018) [62] were the next group to perform bio-solid modeling of the TV and the *first group to investigate the diseased TV*. Within this study, they used a similar parametric representation of the leaflets to that used in Stevanella *et al.* (2010) [135]. Specifically, the authors used B-spline surfaces and curves to represent the TV and chordae geometry within an *isogeometric computational framework*. To simulate the TV closure, they applied a constant transvalvular pressure (TVP) of 25 mmHg to the ventricular surface. Using this isogeometric framework, the authors simulated the *healthy* TV geometry with no modifications and a *chordae rupture* scenario in which they ruptured one of the chordae attached to the TVAL. Results from the chordae rupture scenario showed a significant prolapse of the TVAL into the RA. Although this study is brief in its application, it is the first scenario simulating the TV closure within an isogeometric framework and considering a pathological modification. It illustrates the potential benefits of computational modeling to the clinical setting in understanding the diseased TV.

More recently, Kong *et al.* (2018) reported a more clinically-oriented study [71] that aimed to develop a *patient-specific FE framework using clinical CT imaging data*. The geometries of three patients that were suspected of having coronary artery disease were incorporated

into their FE modeling framework, in which eight-node hexahedral elements and two-node truss elements were used for the TV leaflets and the chordae tendineae, respectively. Due to limited spatial and temporal resolutions of the CT imaging modality, the determination of patient-specific chordae geometry may not be feasible. Therefore, they implemented a chordae configuration based on *ex vivo* measurements of the chordae tendineae. For simulating the TV closure, a pressure traction of 23.7 mmHg was prescribed to the ventricular side of the TV leaflets, and the dynamic motion of the TV annulus and PMs obtained from the medical imaging data was prescribed. The results of the FE simulations varied between the three patients' geometries and when comparing with the previous simulation studies. The average stress in the central area of each leaflet ranged from 24-91 kPa, which relatively agrees with the values from Stevanella *et al.* (2010) [135] but is much lower than the values presented in Aversa and Careddu (2017) [6]. Furthermore, the average strain in the central area of the leaflets (0.12-0.32) was typically much lower than previous simulation studies (Stevanella *et al.*: ~0.52; Aversa and Carredu: 0.40). These stark differences between TV closure amongst the three patients underscore the necessity for patient-specific modeling to enhance the clinical perspective of TV function.

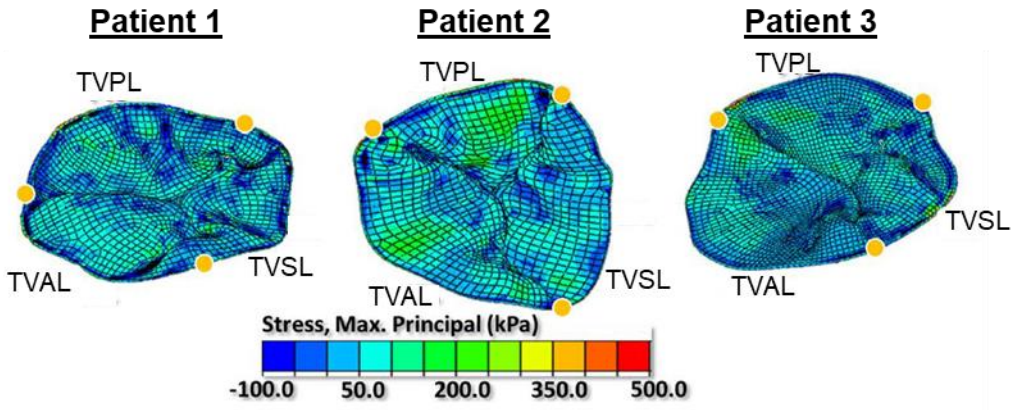

Figure 2-12: FE simulation results from [71] for the three patients' data sets.

CHAPTER 3 Finite Element Model of the Tricuspid Valve

Computational models have previously been employed for understanding the biomechanical function of the TV. The work by Stevanella *et al.* [135] in 2010 provided the first computational model of the TV, but simply used it for general observations of the TV closing behavior. Later, the work by Kong *et al.* (2018) [71] took the first step towards patient-specific computational modeling of the TV. Within this study, they successfully segmented three patients' clinical imaging data, meshed the resulting geometry, and simulated the valve closure. The most recent study by Singh-Gryzbon *et al.* (2019) [125] took the first steps towards fluid-structure interaction computational modeling of the TV. The geometry used within their study was acquired from micro computed tomography (μ-CT) imaging of an excised porcine valve considering "healthy" conditions. They then attempted to predict a TV regurgitation scenario by displacing the PM tips a distance determined from Spinner *et al.* (2011) [130]. These studies are a first step in modeling the complex biomechanical function of the TV considering healthy and a regurgitant state, but they have not comprehensively investigated the diseased TV.

This chapter summarizes recent work in developing a FE model of the TV that is generally classified as: (i) solid component only (i.e., no fluid-structure interactions), (ii) nonlinear in geometry and material properties, (iii) large deformations, and (iv) contact between the leaflet surfaces. This chapter provides specific details of these points by describing the generation of the model geometry and FE mesh (Section 3.1), detailing the selected material models for the TV leaflets and chordae (Section 3.2), providing a detailed

description of the FE simulation boundary conditions and loading (Section 3.3), presenting some results showing the closure of a healthy TV geometry (Section 3.4), and concluding with some brief discussion (Section 3.5).

3.1 Geometry and Finite Element Mesh

The geometry and mesh used to represent the TV is considered in two parts: (i) the TV leaflets, and (ii) the TV chordae tendineae. We have followed similar procedures to our previous study modeling the TV biomechanical function within an isogeometric analysis framework [62]. The key difference lies in the creation of a FE mesh that discretizes the TV geometry. Section 3.1.1 describes the creation of the TV leaflet geometry and FE mesh, Section 3.1.2 details the creation of the TV chordae tendineae geometry and FE mesh, and Section 3.1.3 provides the combined, finalized FE geometry.

3.1.1 Tricuspid Valve Leaflets

Cubic B-splines and surfaces have previously been shown to provide an accurate representation of the AHV leaflet geometry and extremely convenient when using segmented geometry acquired from imaging data [32, 63, 85]. Thus, we elected to use cubic B-splines and surfaces to represent the TV leaflets. Specific parameters for describing each leaflet height and commissure height (cf. Figure 3-1) were taken from a representative porcine heart and are provided below in Table 3.1.

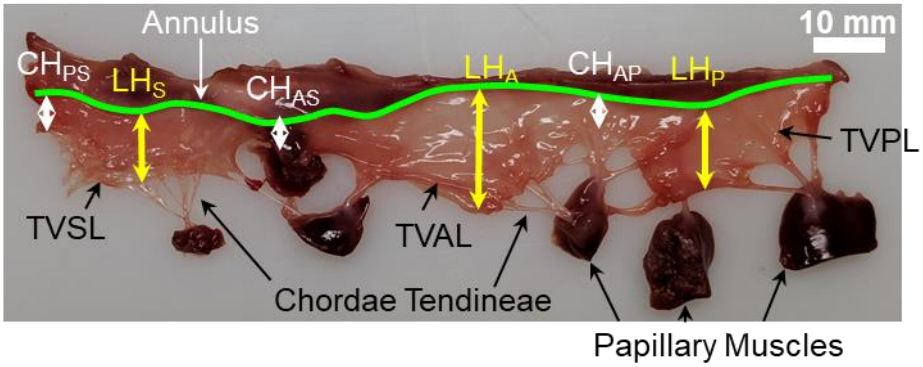

Figure 3-1: Experimental photo of an excised porcine TV with highlighted key anatomical features and dimensions.

Table 3-1: Numerical values for the anatomical dimensions used in the geometry creation.

LH_S	LH_A	LH_P	CH_{PS}	CH_{AS}	CH_{AP}
13 mm	14 mm	14 mm	9 mm	9 mm	9 mm

These parameters help describe the dimensions of the leaflets but provide insufficient information about the saddle shape of the TV annulus. Therefore, we further used μ-CT imaging data for an ovine TV fixed in the closed position to describe the annulus shape. The acquired annulus shape and parametric representation for the TV leaflets were combined, resulting in the final TV leaflet geometry considering the saddle-shaped annulus. This geometry was discretized using ABAQUS/CAE (Dassault Systèmes) with 8850 four-node shell (S4) elements. The thickness for each leaflet was taken from Jett *et al.* (2018) [59]; specifically, the TVAL was 0.52 mm, the TVPL was 0.46 mm, and the TVSL was 0.37 mm.

3.1.2 Chordae Tendineae

The chordae tendineae are extremely difficult to accurately segment from imaging data due

to their small dimension and proximity to one another. It is common to instead use an idealized representation of the chordae tendineae with certain assumptions [64]. In this study, we have followed this approach and idealized the chordae tendineae as 11 chordae tendineae originating from the three papillary muscle tips (modeled as single nodes). These 11 main chordae tendineae then branch twice into series of smaller segments before they insert into the TV leaflet geometry. As for discretizing this geometry into a FE mesh, the chordae tendineae segments were broken up into a series of 3D truss elements (T3D2) with a diameter of 0.46 mm.

3.1.3 Finite Element Computational Mesh

The FE meshes describing the TV leaflets and chordae tendineae were combined using ABAQUS/CAE. It is imperative to ensure the two meshes align properly for the subsequent FE computational model. Therefore, care was taken to ensure the chordae tendineae and TV leaflet meshes shared a node where the two meshes contacted one another. This guaranteed the compatibility of the meshes and allowed for the two meshes to interact while simulating TV closure. The resulting FE mesh for the TV is provided in Figure 3-2 illustrating the TV leaflets and the 11 chordae tendineae originating from the three papillary muscle tips.

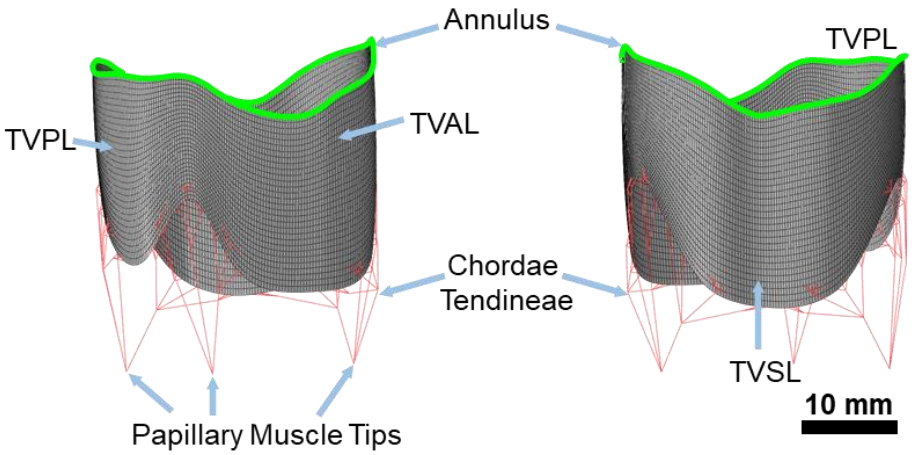

Figure 3-2: FE mesh for the combined TV leaflet and chordae tendineae geometries.

3.2 Material Model

The selection of a specific material model for representing the mechanical behavior of the TV leaflets or chordae tendineae has been shown to have an impact on the closing behavior of AHV leaflets [85]. However, in certain scenarios it can be detrimental to consider a highly complex, microstructurally-based material model due to the significant increase in required computing time. As highlighted in Chapter 1, the scope of the computational modeling work described in this chapter and Chapter 4 is to provide a *parametric* investigation of different diseased/pathological states on the biomechanical function of the TV. Thus, for the purpose of this study it is reasonable to use a simplified material model that only considers the transversely isotropic mechanical behavior rather than the anisotropic mechanical response shown in Section 2.3. The TV leaflets were assumed to be incompressible, and an exponential SEDF was used:

$$W = \frac{c_0}{2}(I_1 - 3) + \frac{c_1}{2}(e^{c_2(I_1-3)^2} - 1) - \frac{p}{2}(I_3 - 1). \quad (3.1)$$

Here c_0, c_1, and c_2 are material properties, I_1 is the first invariant of the right Cauchy-Green deformation tensor **C**, and p is the penalty parameter to enforce the incompressibility condition, i.e., $I_3 = 1$. The material properties adopted for this numerical study were soured from [62], which are c_0=10 kPa, c_1=0.209 kPa, and c_2=9.046. On the other hand, the chordae tendineae were modeled using a nonlinearly elastic material model with an elastic modulus of 40 MPa and a Poisson's ratio of 0.30.

The TV material model was implemented into ABAQUS via the VUMAT subroutine. To verify the implementation of the material model into the computational framework, we performed a simplified simulation considering one four-node element undergoing equibiaxial tension. This element was assumed to have two planes of symmetry (Figure 3-3a), while the displacement is applied in both the *x*- and *y*-directions. Simulations results agree perfectly with the analytical solutions (Figure 3-3b), indicating the successful implementation of the material model as described in Eq. (3.1) into the VUMAT subroutine.

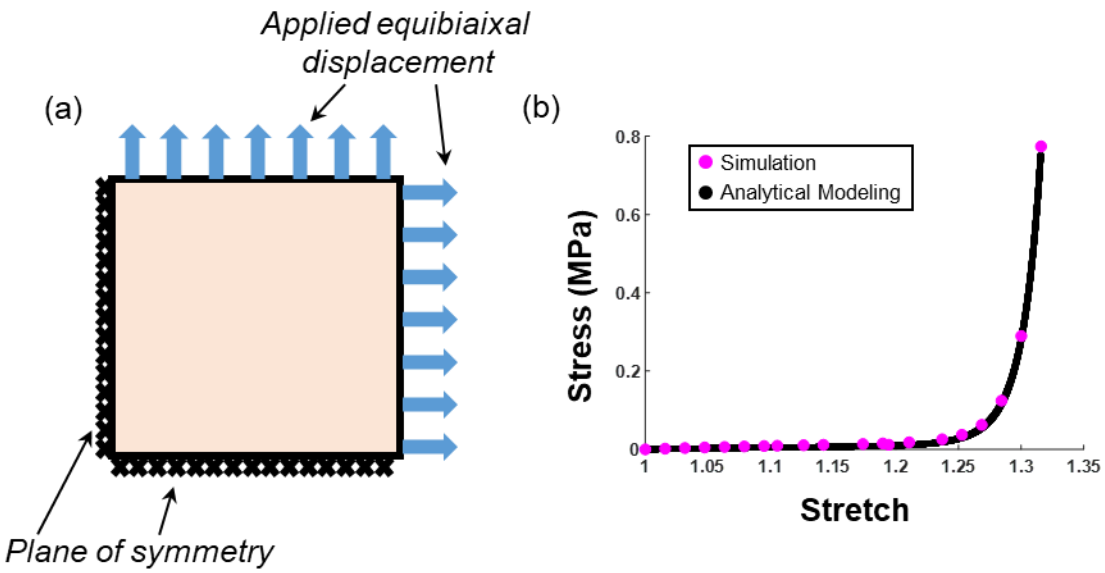

Figure 3-3: (a) FE simulation setup of a equibiaxial displacement problem to validate the implementation of the VUMAT subroutine. (b) Comparison between the analytical solutions and the FE simulation results.

3.3 Boundary and Loading Conditions

TV closure is a complex dynamic process as described in Section 2.1.2. Briefly, the TV leaflets close as a result of the developing hemodynamics and transvalvular pressure gradient as the RV contracts, the annulus contracts in a uniform manner maintaining its distinct saddle-shaped configuration, and the papillary muscle tips follow the contractile motion of the RV. Some previous studies have carefully modelled each of these dynamic motions. For example, [135] modeled the time-dependent transvalvular pressure gradient curve that develops as the RV contracts using a time-dependent pressure curve and [62, 71] the dynamic motion of the annulus by prescribing displacements to the annulus nodes

with similar approaches used for the PM movement. The purpose of the present study is to determine the effect of various pathological states on the *closed* TV geometry and mechanics. It is reasonable to make certain simplifications to the boundary and loading conditions that reduce the complexity of the simulation. The boundary conditions used for this FE simulation scenario are described as follows.

An *in vivo* study has shown that the developed transvalvular pressure gradient within the right ventricle nonlinearly changes over time and reaches a maximum value of approximately 25 mmHg [60]. For our developed FE model, we selected to apply a constant transvalvular pressure gradient of 25 mmHg to the ventricular side of the leaflets over a time of 0.4s, which corresponds to the approximate time of systole. Furthermore, we have assumed the annulus nodes were fixed and the nodes representing the papillary muscle tips were pinned to ensure no rigid body motion. The ABAQUS self-contact algorithm with a contact penalty parameter of 0.5 was used to model the contact between any two of the three TV leaflets throughout the systolic closure process. It was assumed that the chordae tendineae would not contact with the leaflet surface during the simulations. The loading and boundary conditions are summarized in Figure 3-4.

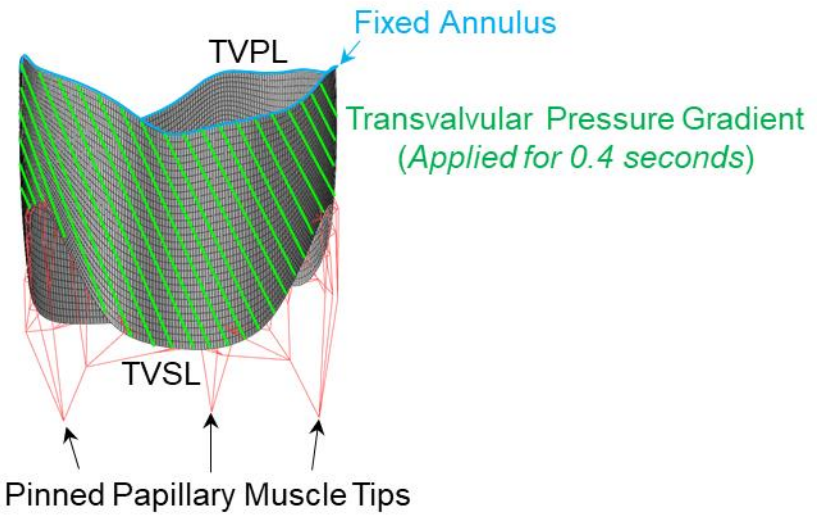

Figure 3-4: Boundary and loading conditions for the FE simulation of the TV systolic closure.

3.4 Simulation of Healthy TV Closure

The details outlined in the previous three sub-sections were combined within an ABAQUS input file and solved using the ABAQUS/Explicit solver. The simulation results from this healthy simulation scenario are presented in this section. First, general observations of the simulation results are provided in Section 3.4.1 including the closed geometry, the coaptation, and clinical values for the coaptation between any two leaflets. Then the computed engineering mechanics metrics (the von Mises stress and the maximum principle Green strain) are presented and analyzed in Section 3.4.2. The von Mises stress σ_{VM} and maximum in-plane Green strain $E_{principle,\max}$ are defined as follows:

$$\sigma_{\mathrm{VM}} = \sqrt{\sigma_x^2 + \sigma_y^2 - \sigma_x \sigma_y + 3\sigma_{xy}^2}\ , \tag{3.2}$$

$$E_{principle,\max} = \max\left(\frac{E_x + E_y}{2} \pm \sqrt{\left(\frac{E_x - E_y}{2} \right)^2 + \left(\frac{E_{xy}}{2} \right)^2} \right), \tag{3.3}$$

where σ_x and E_x are the Cauchy stress and Green strain in the x-direction, σ_y and E_y are the Cauchy stress and Green strain in the y-direction, and σ_{xy} and E_{xy} are the shear components of the Cauchy stress and Green strain. The results presented in this section provide a necessary baseline for comparisons to be made with diseased/pathological scenarios as presented in Chapter 4.

3.4.1 Simulation Results – Geometrical Metrics

The FE simulation results modeling the healthy scenario demonstrated excellent closure of the three TV leaflets and the ABAQUS contact algorithm successfully captured the complex contact throughout systole (Figure 3-5). The contact between any two leaflets is generally located near the corresponding commissure, e.g., coaptation between the TVAL and TVPL is located near the anterior-posterior commissure. Furthermore, the chordae tendineae supported the TV leaflet closure ensuring the TV leaflets did not prolapse into the right atrium.

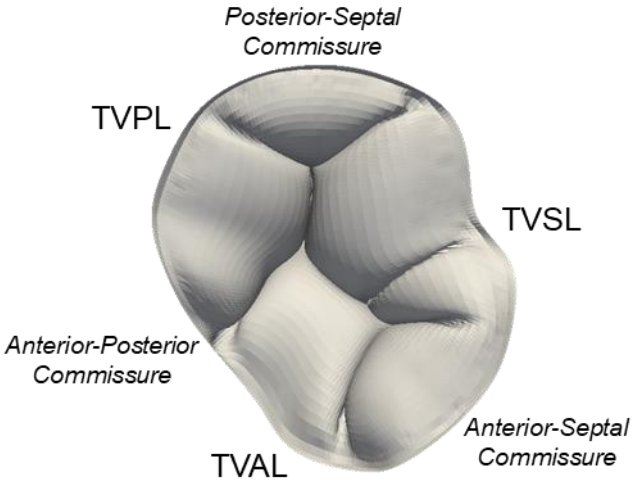

Figure 3-5: Resulting closed TV geometry from the FE simulation.

When observing the closed TV geometry, one will notice from Figure 3-5 that the closed TV geometry is complex with a clear coaptation line and a wrinkle in the TVSL geometry. The coaptation line can be analyzed at various places along the leaflet contact (into the plane of Figure 3-5) by taking different slices in ParaView (Kitware). Figure 3-6 presents the TV leaflet coaptation pattern at three different locations. This figure demonstrates that generally the coaptation pattern is consistent at different points along the leaflet contact. While this observation does not have any inherent value to understanding the simulation, the shape of the coaptation line along the leaflet contact can be compared in diseased/pathological states to elucidate the corresponding changes.

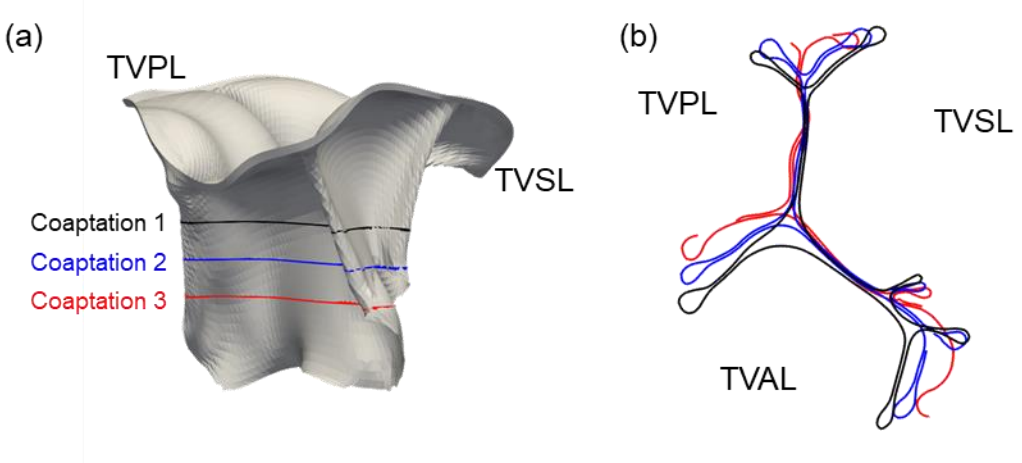

Figure 3-6: (a) Illustration of the three slices made for viewing the TV coaptation, and (b) visualization from above the TV of the leaflet coaptation at the three locations.

One clinical method for understanding the shape of the closed TV geometry is calculating different quantitative values from a 2D projection of the leaflet closure often taken from 2DTTE medical imaging. These values can also be calculated for the FE simulation results by taking three "slices" through the closed TV geometry where any two leaflets are contacting one another (Figure 3-7a). The resulting 2D contour of the closed geometry can then be analyzed to quantify the *tenting area* (TA), *tenting height* (TH), and the *coaptation height* (CH) (Figure 3-7b).

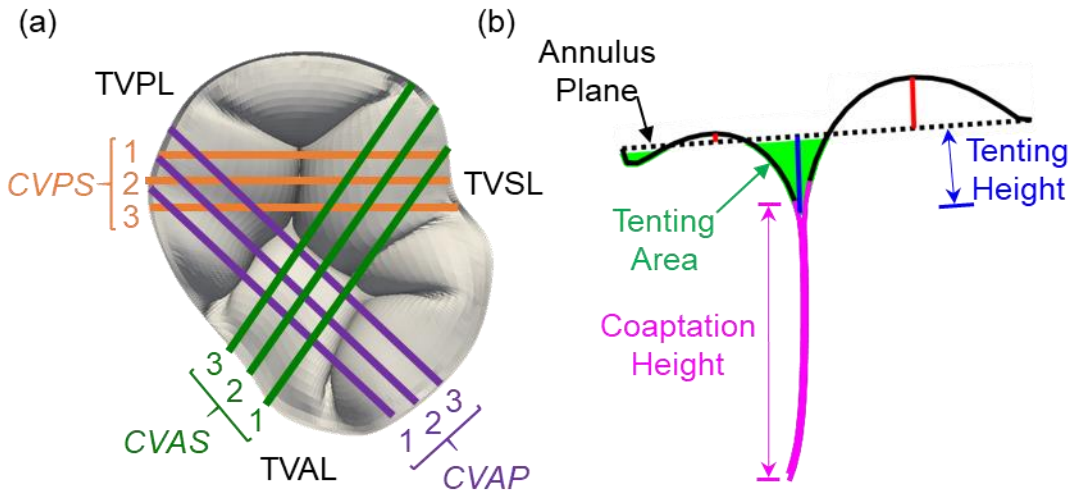

Figure 3-7: (a) Illustration of the three slices per coaptation between two leaflets, and (b) definition of geometrical values for each slice. (CVAP: Cut View Anterior-Posterior, CVAS: Cut View Anterior Septal, CVPS: Cut View Posterior Septal).

Two comparisons are made using these values: (i) comparisons between the slices of the three leaflet contact scenarios, and (ii) comparisons between the slices within one leaflet contact scenario. These comparisons provide a fundamental understanding of how the quantitative values vary throughout the model, which is later used in comparisons to diseased scenarios.

Figure 3-8a shows the three quantitative geometrical values, including the tenting area, tenting height, and the coaptation height, for the three different leaflet contact scenarios considering the "middle" slice (e.g., CVAP-2 or CVAS-2). The numerical values are provided in Figure 3-8b-d.

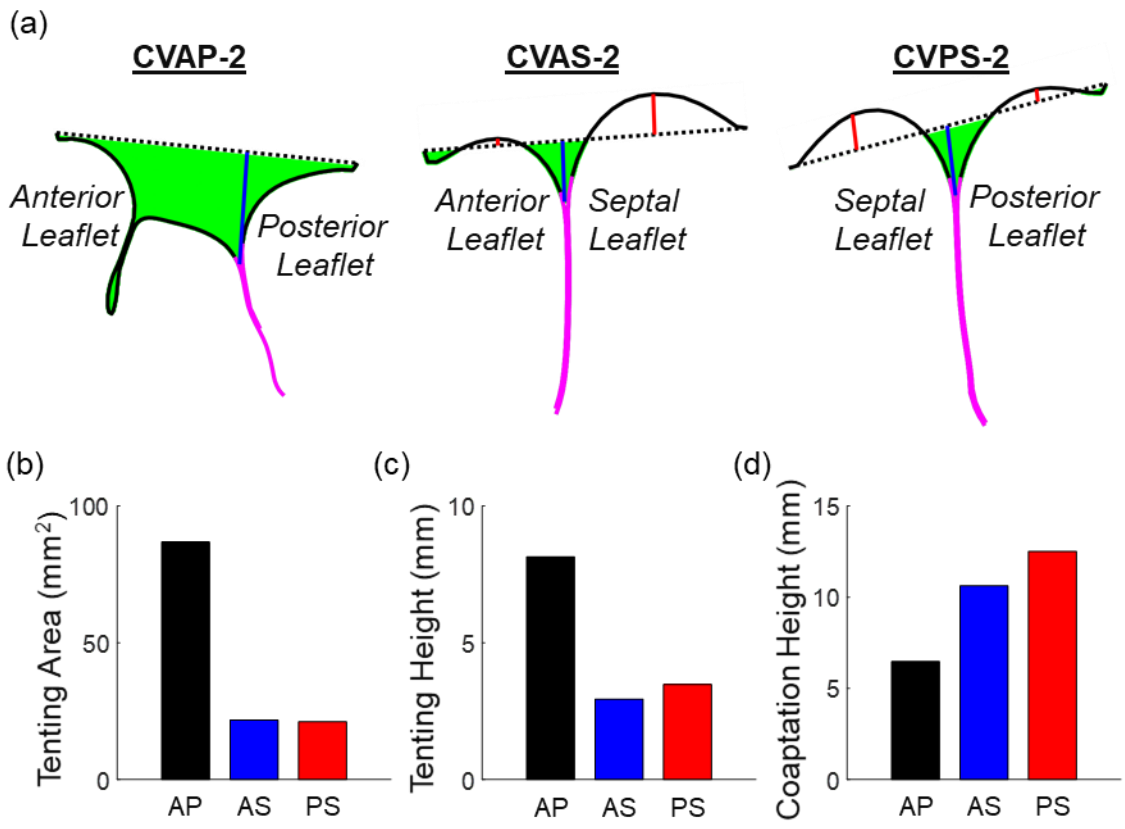

Figure 3-8: (a) Representative slice views for each coaptation for the healthy simulation and (b) the corresponding quantitative values for each view in (a).

The tenting area and the tenting height are consistently greater, and the coaptation height is consistently lower for the contact between the TVAL and TVPL (CVAP), indicating that the TVAL and TVPL are contacting one another much lower below the annulus plane than the other two leaflet contact scenarios, and that the contact length between the leaflets is much smaller. This is also reflected in the corresponding slices views for each of the leaflet contact scenarios. On the other hand, when comparing between the contact of the TVAL and TVSL (CVAS) and TVPL and TVSL (CVPS), we observe that the quantitative values are relatively similar within the same order of magnitude. The quantitative values can also be compared to those determined in clinical studies, but it should be noted that the hearts

within the clinical setting are human heart valves while the FE model presented is for porcine heart valves. Clinical studies have observed the tenting height to be 4.6 ± 2.1 mm [137], while clinical recommendations state that tenting area >100 mm^2 suggest TV regurgitation [79]. The healthy simulation values fall within a similar range compared to the clinical observations.

In addition, Figure 3-9 presents the three quantitative values (tenting area, tenting height, and coaptation height) at three different points along each of the three leaflet contact scenarios. At first glance, one will notice that the tenting area and tenting height results have unique trends within one leaflet contact scenario. CVAP shows a general increase as one moves from CVAP-1 to CVAP-3 while CVAS and CVPS show a decrease from CVAS-1 to CVAS-2 and an increase to CVAS-3. The coaptation height results are starkly different: the CVAP scenario shows a large decrease in coaptation height from CVAP-1 to CVAP-2, contrarily the CVAS scenario shows a large increase from CVAS-1 to CVAS-2, and the CVPS scenario shows a very minimal decrease in coaptation height from CVAS-1 to CVAS-3. The changes of these quantitative values across the leaflet contact scenario provides enhanced information of the leaflet contact that may be unobtainable using conventional clinical 2D methods.

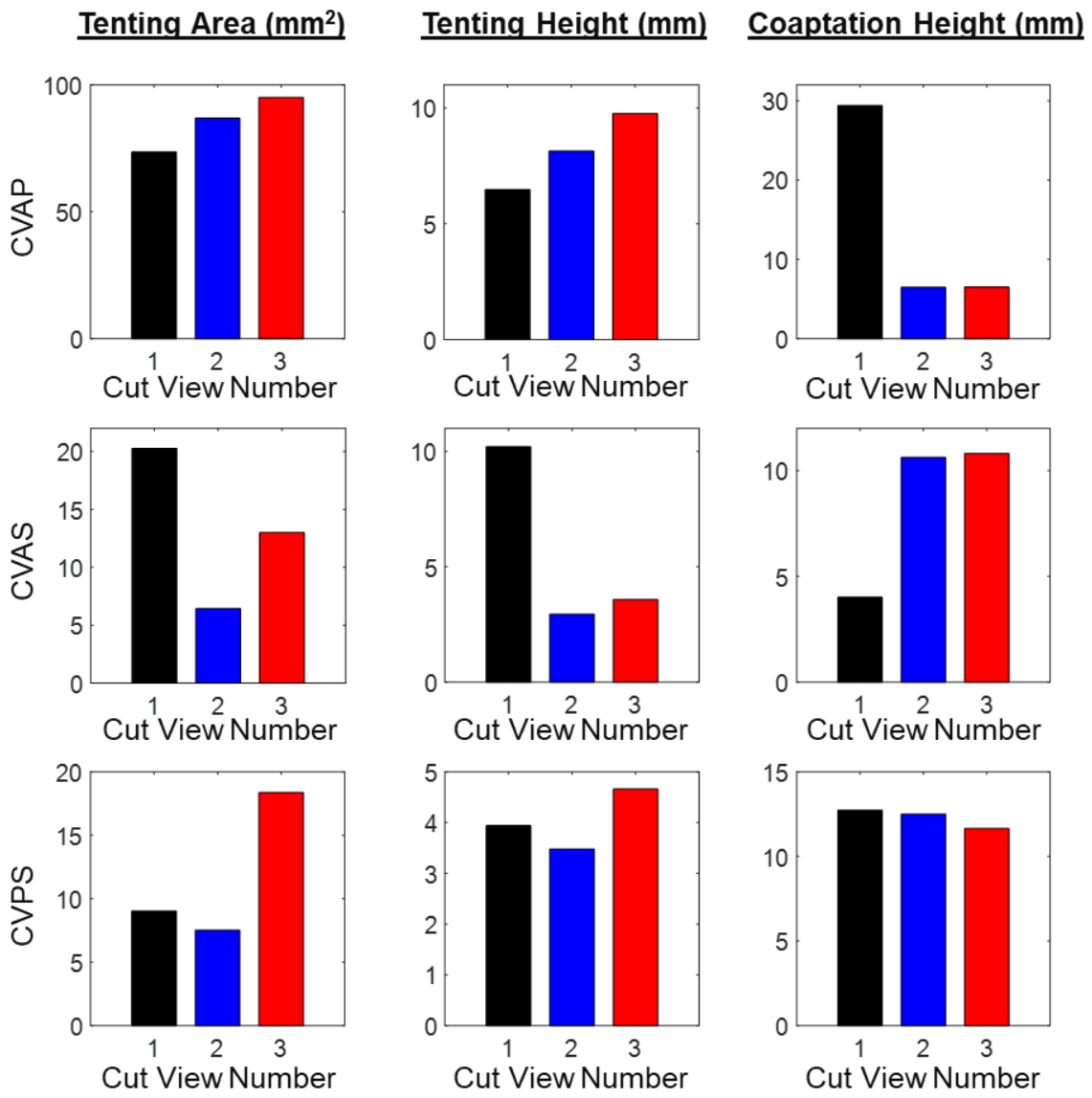

Figure 3-9: Quantitative geometrical values for each cut view (cf. Figure 3-7) of each coaptation between two leaflets.

3.4.2 Simulation Results – Engineering Mechanics Metrics

Section 3.4.1 provided a thorough presentation of the resulting FE geometry while this section will focus specifically on the computed engineering mechanics metrics. Three mechanical values were of interest within this study: (i) the leaflets' von Mises stress, (ii)

the leaflets' Green strain, and (iii) the PM reaction force. The contours and quantitative values are further elaborated in the ensuing paragraphs.

The contour of the von Mises stress and Green strain projected onto the closed TV geometry is provided in Figure 3-10. One will notice there is large variations in the stress values with the maximum values appearing near the annulus and the minimum values generally occurring near the commissures.

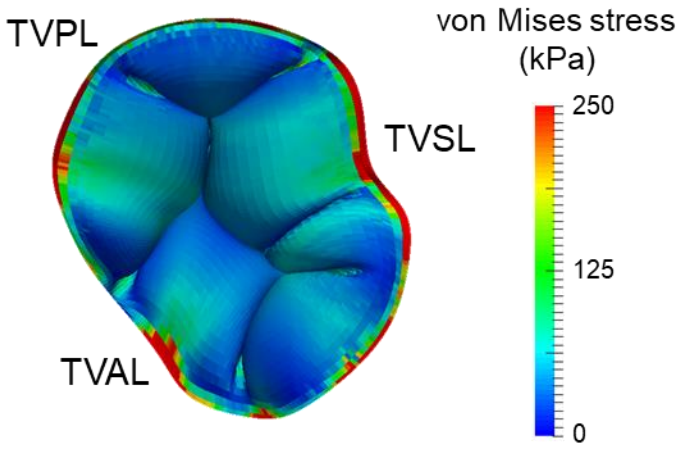

Figure 3-10: The von Mises stress contour of the closed TV geometry obtained from the FE simulation.

A maximum leaflet stress of ~125 kPa appears to be similar between the three leaflets. This value is generally larger than previous computational studies for the TV (12-100 kPa) [71, 125, 135], but it agrees with previously approximated *in vivo* leaflet stress values that are 125 kPa [59, 65]. Additionally, we have averaged the von Mises stress values across all leaflet elements to provide a generalized metric of the stress within the TV leaflet

geometry, which will prove useful in Chapter 4 for easily comparing the simulation scenarios. For the healthy simulation in this chapter, the average von Mises stress was computed to be 52.2 ± 73.1 kPa.

The second mechanical value determined was the Green strain for each TV leaflet element, and the corresponding contour plot is provided in Figure 3-11. One will quickly notice that the contour follows a similar pattern to the results for the von Mises stress (Figure 3-10).

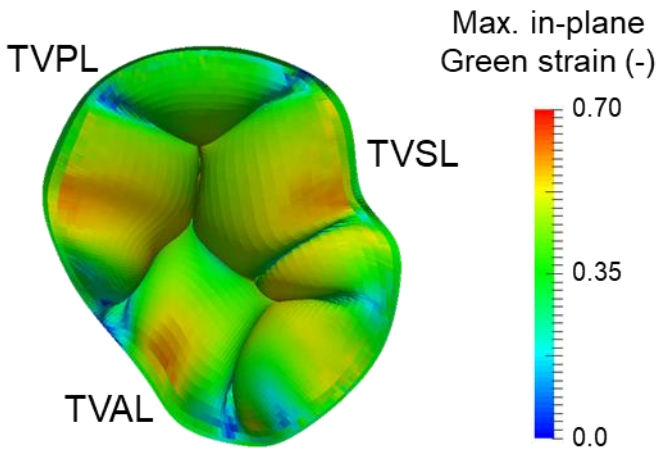

Figure 3-11: Maximum in-plane Green strain contour of the closed TV geometry obtained from the FE simulation.

The major difference is that the maximum Green strain is in the belly region (~0.55) of the TV leaflets rather than the annulus as it was for the von Mises stress. Nevertheless, the minimum Green strain values are located near the leaflet commissures. The magnitude of the maximum strain value is relatively large compared to previous studies (+12%-52%) [71, 125, 135], but this could arise due to the selection of an isotropic material model.

Furthermore, a similar approach is utilized to average the Green strain across all TV leaflet elements to provide a metric of the leaflet strain, arriving at a value of 0.37 ± 0.12.

The final mechanical value computed for this FE simulation that will be used in comparisons within Chapter 4 is the PM reaction forces. These values were selected rather than the chordae forces or stresses so later it could be easily understood how the ensemble of chordae tendineae originating from a PM are affected by a disease or pathology scenario. The PM reaction forces for the healthy scenario were found to be 0.30 N for the anterior-posterior PM, 0.47 N for the anterior-septal PM, and 0.35 N for the posterior-septal PM.

3.5 Discussion

This chapter has described the development of a FE model for the TV. The geometry and mesh were informed from a parametric representation of a porcine TV leaflets and medical imaging data for the annulus shape. An incompressible, transversely isotropic, exponential material model was selected to represent the leaflets' mechanical response while a nonlinear elastic material model was selected for the chordae tendineae. FE simulations were performed using the ABAQUS/Explicit solver by fixing the annulus and PM tips and prescribing a constant transvalvular pressure gradient of 25 mmHg to the ventricular side of the leaflet mesh. Finally, some general observations were made for the FE simulation results. The quantification of the geometrical values presented in Section 3.4.1 has not been done before in literature for the tricuspid valve. The von Mises stress and Green strain values for the FE simulations presented in this chapter were larger than those found in the

previous studies [71, 125, 135]. These differences could arise from the definition of the FE model geometry or material properties; however, the maximum von Mises stress (~125 kPa) in this study is close to previous approximations for the *in vivo* stress (125 kPa) using the Laplace's law. This developed FE model is utilized in Chapter 4 to consider diseased/pathological states with comparisons to the healthy scenario in this chapter.

CHAPTER 4 Finite Element Simulations of the Diseased Tricuspid Valve

In silico and *in vitro* methods have been employed to understand FTR and the corresponding underlying mechanisms. For example, the work by Spinner *et al.* (2011-2012) [129, 130] used an *in vitro* flow system to prescribe different states of annulus dilation (AD) and PM displacement to determine how each disease scenario contributes to TR. The later work by Casa *et al.* (2013) [20] made a similar study to quantify how pulmonary hypertension (PH) and annulus dilation affected the TV biomechanical function through determining the *tenting area (TA)* and *coaptation area* (analogous to the CH defined in Chapter 3). The *in silico* work by Kamensky *et al.* (2018) [62] examined the effect of chordae rupture on the TV's closing behavior, whereas the work by Singh-Gryzbon *et al.* (2019) [125] displaced the PM tips to create a state of TR using an FSI computational model. These studies have been successful in instigating a state of TR either in an *in vitro* flow loop or through an *in silico* computational model. However, none of the studies have provided a comprehensive study into how various pathologies associated with FTR (i.e., PH, AD, PM displacement, and/or chordae rupture) affect the closing geometry and biomechanical quantities of the functioning tricuspid valve. The objective of the work presented in Chapter 4 is to utilize the FE computational model developed in Chapter 3 to simulate various diseased states for determining how each affects the biomechanical function of the TV. Section 4.1 describes the different pathological study scenarios. Section 4.2 presents the FE simulations results pertinent to the determination of the effects of pathologies on the TV closing behavior. Results of the progression of the pathology to

determine the progressive changes are presented in Section 4.3, followed by discussions of the FE simulation results and study limitations in Section 4.4.

4.1 Study Scenarios of Various Pathological Conditions

Five different pathological scenarios were considered in this study: (i) PH, (ii) flattened annulus shape, (iii) AD, (iv) PM displacement, and (v) chordae rupture. The first four scenarios were selected since they are typically associated with FTR that stems from PH, while the fifth scenario was chosen as it is another mechanism by which FTR can be initiated. The PH, flattened annulus, and chordae ruptures scenarios were prescribed by modifying the FE simulation mesh or input. On the other hand, the AD and PM displacement were prescribed by a separate FE simulation prior to simulating TV closure. For these three scenarios, the altered (diseased) geometry was the stress-free reference configuration for the subsequent TV closure FE simulations. Specific details for prescribing all five pathological conditions in the FE simulations are discussed as follows.

4.1.1 Pulmonary Hypertension

The healthy scenario presented in Chapter 3 used a transvalvular pressure gradient of 25 mmHg applied to the ventricular surface of the leaflet mesh. Pulmonary hypertension is defined as an increase in the transvalvular pressure gradient within the right side of the heart from 25 mmHg up to a maximum of ~45 mmHg [92]. For the purpose of this study scenario, pulmonary hypertension associated with a transvalvular pressure gradient of 40 mmHg is considered. Additionally, simulations considering different degrees of PH, i.e.,

25 mmHg, 30 mmHg, 35 mmHg, and 40 mmHg, were also performed to investigate the progression of pulmonary hypertension.

4.1.2 Flattened Annulus

It is known that the TV annulus will become flattened as it dilates away from the septum due to the alteration in the TV geometry. Therefore, all simulation scenarios have considered either a saddle annulus shape (typically in a healthy TV) or a flattened annulus shape (diseased). The flattened annulus shape was created using our parametric geometry modeling framework, and a comparison of the TV annulus geometry between the saddle and flattened shapes is illustrated in Figure 4-1.

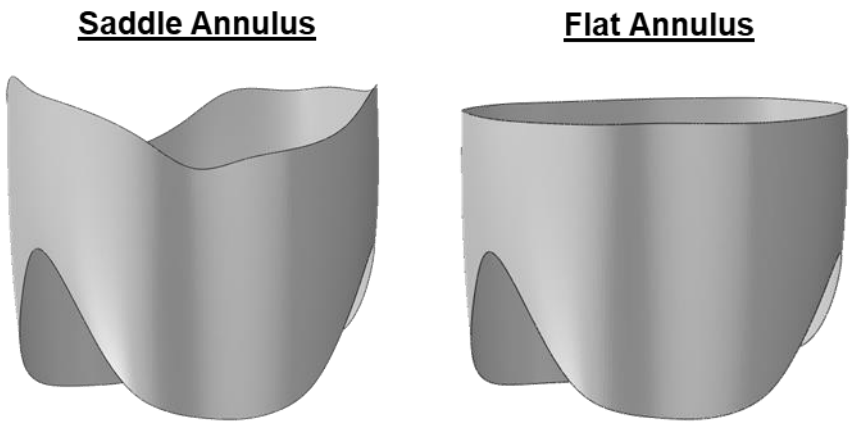

Figure 4-1: The saddle annulus shape (*left*) and the flattened annulus shape (*right*) considered in the FE simulations.

4.1.3 Annular Dilation

It has been shown that the annulus will typically dilate away from the septum, by moving from an elliptical shape to a more circular one [106, 142]. The assumed mechanism of this

anisotropic dilation is that the septum is fixed and will not dilate like the free wall of the right ventricle. This assumption has not been tested, so two types of AD were considered: (i) uniform AD where the annulus dilates equally in all directions (Figure 4-2a), and (ii) non-uniform AD where the annulus dilates primarily away from the septum (Figure 4-2b).

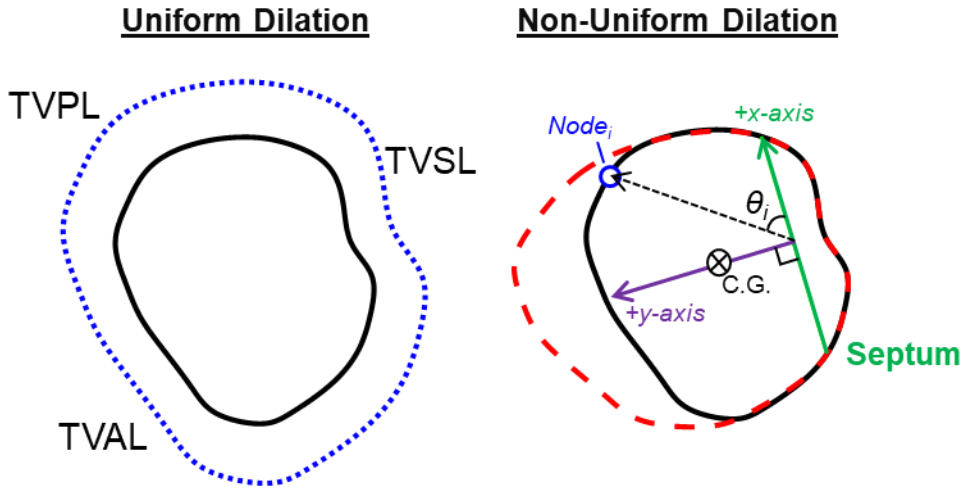

Figure 4-2: Schematic of the uniform AD scenario (*left*) and the clinically-observed non-uniform AD scenario (*right*).

The uniform AD was prescribed in a separate simulation prior to simulating the TV closure. First, the healthy, saddle-shaped TV annulus was uniformly dilated resulting in a 40% increase in the annulus circumference. Specifically, displacements were prescribed on the annulus nodes, while constraining the papillary muscle nodes. Increments of 10% increase in the TV annulus circumference up to the maximum 40% were considered to investigate the progression of the uniform annular dilation.

The non-uniform AD was prescribed in a similar manner to the uniform AD scenario. The key difference is that the annulus nodes were displaced away from the septum in a non-

uniform manner. The saddle shape of the annulus was not considered in the calculations for the non-uniform AD, so a 2D representation of the annulus was created (cf. Figure 4-2). In brief, the septum line was created based on the location of the septal leaflet. Then, the annulus' center of geometry was determined, and a local coordinate system (cf. *x*- and *y*-axes in Figure 4-2 (*right*)) was created based on the septum line and its normal. The new coordinates for the dilated annulus nodes were computed by the following equation:

$$\begin{bmatrix} x_i^{new} \\ y_i^{new} \\ z_i^{new} \end{bmatrix} = \begin{bmatrix} x_i^{old} \\ \left\{\alpha \cdot \sin\left(\theta_i\right)+1\right\} y_i^{old} \\ z_i^{old} \end{bmatrix},\ i = 1 - N_{node}, \tag{4.1}$$

where x_i^{old}, y_i^{old}, and z_i^{old} are the *original x*, *y*, and *z* coordinates for the i^{th} annulus node (*Node i*) , respectively, x_i^{new} y_i^{new}, and z_i^{new} are the *new x*, *y*, and *z* coordinates for *Node i*, respectively, θ_i is the corresponding angle between the *x*-axis and the line connecting the local coordinate system's origin to *Node i*, N_{node} is the number of annulus nodes, and α is the decimal equivalent of the percentage annulus circumference increase (e.g., 0.40 corresponding to a 40% increase). Those annulus nodes located "below" the septum line were assumed to not dilate in accordance with clinical observations. The initial FE simulation was then performed to dilate the healthy annulus nodes to these new, pathological locations by prescribing the quantified displacements and fixing the PMs. Non-uniform AD scenarios in intervals of 10% up to a maximum value of 40% were considered for comparisons.

4.1.4 Papillary Muscle Displacement

A study by Spinner *et al.* (2012) [129] quantified different anatomical dimensions of the TV and the RV using 3D echocardiography for healthy patients and patients with tricuspid

regurgitation. Within this study, Spinner *et al.* realized that for those patients with TR, the papillary muscles often displace laterally away from the septum, as well as apically towards the RV apex. A similar two-step simulation approach was utilized as described in Section 4.1.3. Rather than displacing the annulus nodes, the PM tips were displaced longitudinally and apically (Fig. 4-3) according to those values found in Spinner *et al.* (2012). FE simulation results for: (i) only the longitudinal PM displacement, (ii) only the apical displacement, and (iii) the combined apical and longitudinal PM displacements are presented in Sections 4.2-4.3. These three scenarios were also considered in intervals of 20% (i.e., 20%, 40%, etc.) of the maximum PM displacement value found in Spinner *et al.* (2012). The average body surface area used to transform the index values in Spinner *et al.* (2012) to real displacement values was 1.79 m^2 [118].

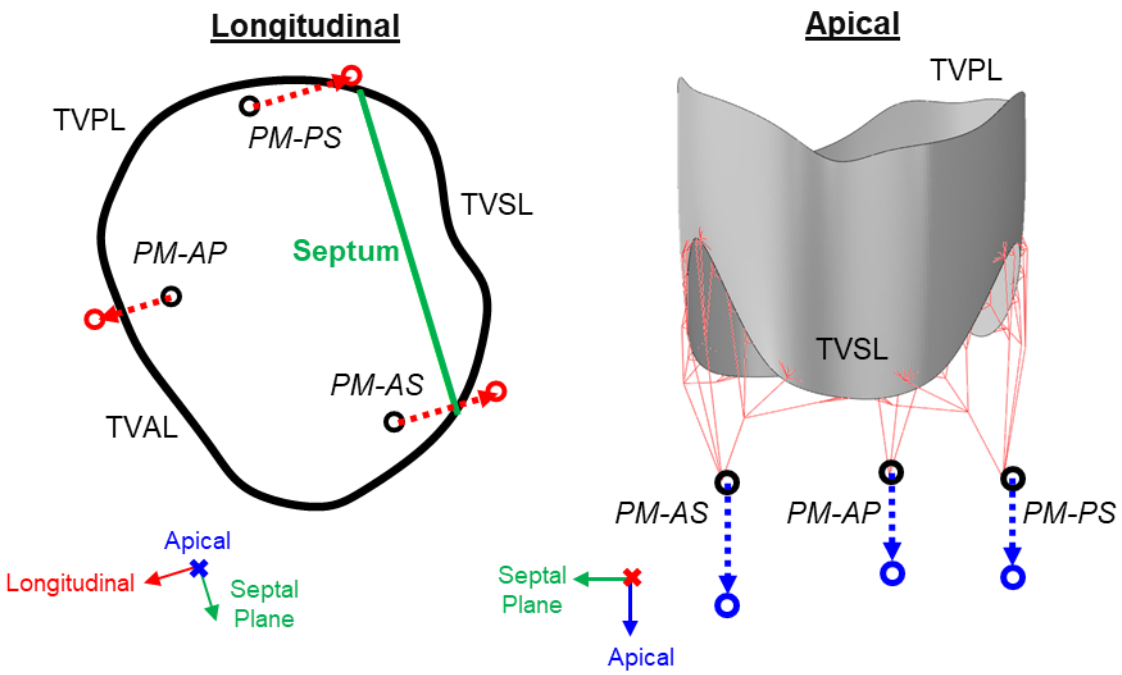

Figure 4-3: Two scenarios for the PM displacement: the longitudinal displacement perpendicular to the septum line (*left*), and the apical displacement towards the apex of the heart (*right*).

4.1.5 Fully-Diseased Scenario

It is expected that a fully-diseased TV has some combination(s) of the previously-described pathologies that contribute to the presence of tricuspid regurgitation. Therefore, a study scenario was simulated with all of the previously mentioned pathologies included. The applied transvalvular pressure gradient was increased to 40 mmHg for PH, the annulus was non-uniformly dilated to a +40% scaled value, the PMs were displaced longitudinally and apically, and the annulus shape was flattened.

4.1.6 Chordae Tendineae Rupture

The previous study by Kamensky *et al.* (2018) [62] simulated a scenario where one particular group of chordae tendineae was ruptured. This simulation was primarily for demonstration of their developed contact algorithm, and therefore, they did not provide a thorough investigation of different chordae tendineae rupture scenarios. Hence, we aim to provide a more comprehensive examination of which chordae tendineae, when ruptured, contribute to the prolapse of the TV leaflets. To accomplish this, we have classified 11 different "chordae groups" (Figure 4-4). A FE simulation was performed where one of these chordae groups was "ruptured" by removing the corresponding truss elements.

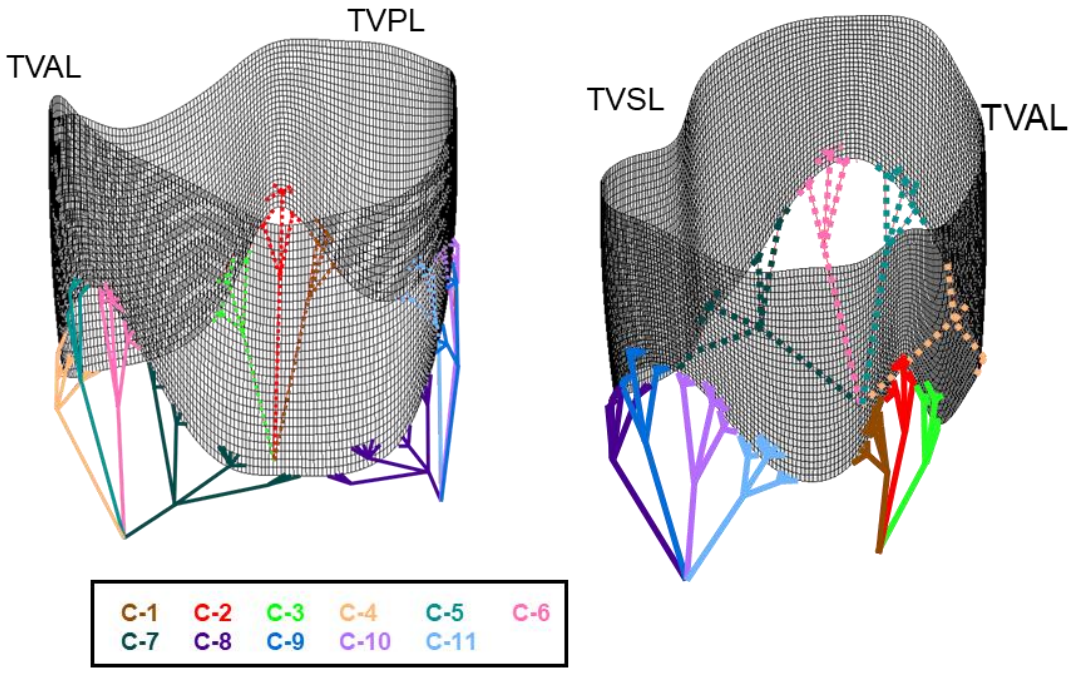

Figure 4-4: Definition of the eleven chordae tendineae groups.

The initial results of FE simulations of rupturing only one group of chordae tendineae did not produce any TV leaflet prolapse, so we modified this pathological study scenario to

rupture combinations of two chordae groups, leading to 55 total simulation cases to determine which scenarios resulted in the TV leaflet prolapse.

4.2 FE Simulation Results of Various Pathological Scenarios – Engineering Mechanics Metrics

The von Mises stress and the Green strain were averaged for all TV leaflet elements. Figure 4-5 provides the minimum, maximum, and average von Mises stress and Green strain for each scenario considered. The PH scenario resulted in the largest increase in average von Mises stress (86.2 ± 116.2 kPa, +65%) compared to the healthy scenario with a saddle-shaped TV annulus (52.2 ± 73.1 kPa) while the uniform AD scenario had the largest increase (74.6 ± 76.7 kPa, +47%) compared to the healthy scenario with a flattened annulus shape (50.8 ± 72.0 kPa). For the Green strain, the uniform AD had the largest increase (0.477 ± 0.119, +27%) compared to the healthy scenario with a saddle annulus (0.377 ± 0.124) and the uniform AD had the largest increase (0.471 ± 0.119, +29%) compared to the healthy scenario with a flattened annulus (0.364 ± 0.124). The PM displacement scenario had a minimal effect on the von Mises stress considering the saddle-shaped annulus (0.53.6 ± 61.5 kPa, +2.6%) and the flattened annulus shape (48.2 ± 51.4 kPa, -5.1%). Similar trends were observed for the Green strain considering the saddle-shaped annulus (0.413 ± 0.118, +10%) or the flattened annulus (0.402 ± 0.120, +10%). Additionally, the apical and longitudinal displacements provide unique changes to both mechanical values that, when summed, do not equal the change resulting from the combined displacement. Nevertheless, the magnitude of change in the combined PM

displacement scenario was always greater than the individual displacement scenarios. As for the AD scenarios, the uniform scenario had a larger impact (+16%-47%) on the mechanical values compared to the non-uniform scenario (+13%-29%).

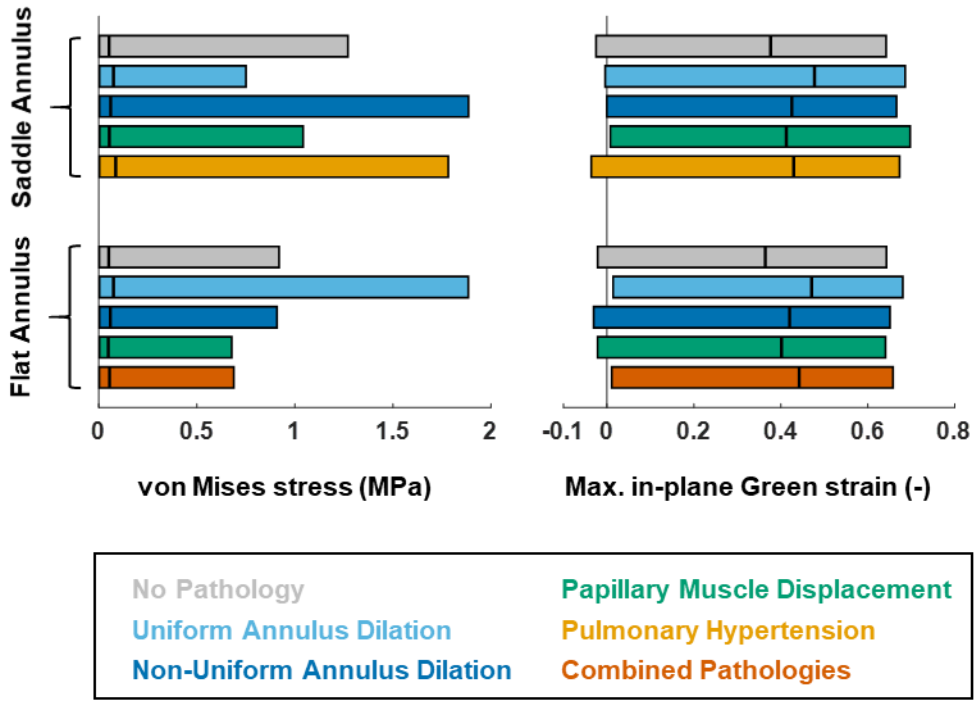

Figure 4-5: Comaprison of the minimum, maximum, and mean stress and strain values for all pathological study scenarios.

This observation may provide some new insight into why the TV generally dilates away from the septum. It may be obvious that the non-uniform displacement away from the septum is largely because the septum is more difficult to displace than the RV free wall. However, the non-uniform AD scenario results in smaller changes in the mechanical environment, which would also be a more favorable scenario from a mechanics perspective. Although the fully diseased scenario was a combination of all pathological scenarios, it did not have the largest magnitude of change for either the von Mises stress or the Green strain. This result suggests that the pathologies may interact in a complex manner

and further investigations into the different pathological combinations are warranted.

The contours of the von Mises stress for each simulated scenario are provided in Figure 4-6. Each study scenario has a unique resulting contour. For example, the uniform AD scenario with a saddle annulus shows a general increase in the TV leaflet stress (58.1 ± 71.8 kPa) compared to the healthy scenario with a saddle-shaped TV annulus (52.2 ± 73.1 kPa).

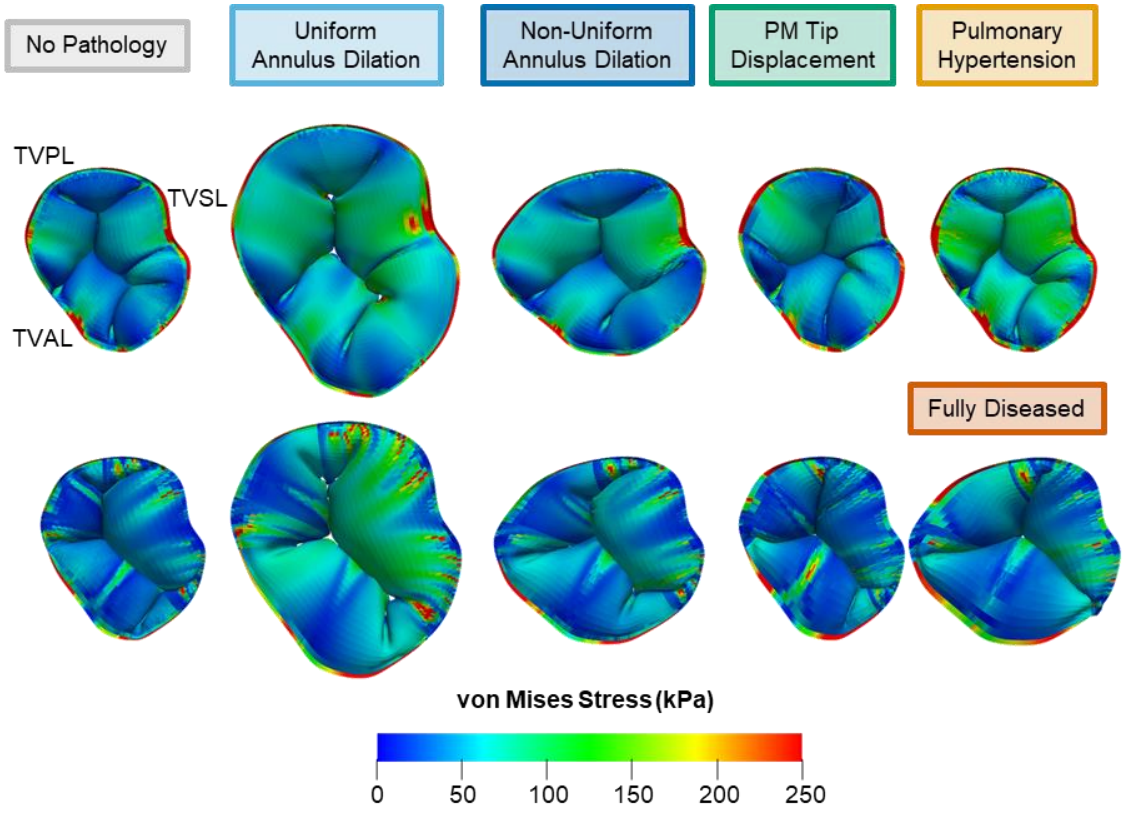

Figure 4-6: Results of the pathological FE simulations for the saddle annulus configuration (*top*) and flat annulus configuration (*bottom*).

There is also some stress concentration near the annulus on the TVSL (Figure 4-6). Interestingly, the flat TV annulus scenarios generally appear to form "stripes" in the stress contour. It is unclear the cause of these stress patterns. It is also important to note that the

von Mises stress and the Green strain contours are very similar for each study scenario. The presented contours provide an excellent general representation of the mechanical values for qualitative comparisons and could be used eventually for informing development of scenario-specific replacement options.

To further observe the progression of the pathologies, the average von Mises stress and Green strain values are plotted for the different increments (Figure 4-7). Results for the PH and AD scenarios show that the increase in stress and strain follows a linear relationship, but the results for the PM displacement scenarios are more complex. The first thing to note is that it appears each type of displacement (apical, longitudinal, and combined) has a different relationship with increasing displacement magnitude. Taking the flat TV annulus and PM displacement scenarios as an example, the stress generally follows a decreasing trend for the three displacement types. The stress of the longitudinal displacement scenario appears to have a more linear trend than the apical or combined displacements. Additionally, when looking at the trends for the Green strain the apical and combined displacements appear to have similar, plateauing trends while the stress in the longitudinal displacement scenario has a more exponential trend. Nevertheless, for all PM displacement scenarios, the combined scenario generally has a larger magnitude of change compared to the apical or longitudinal displacements.

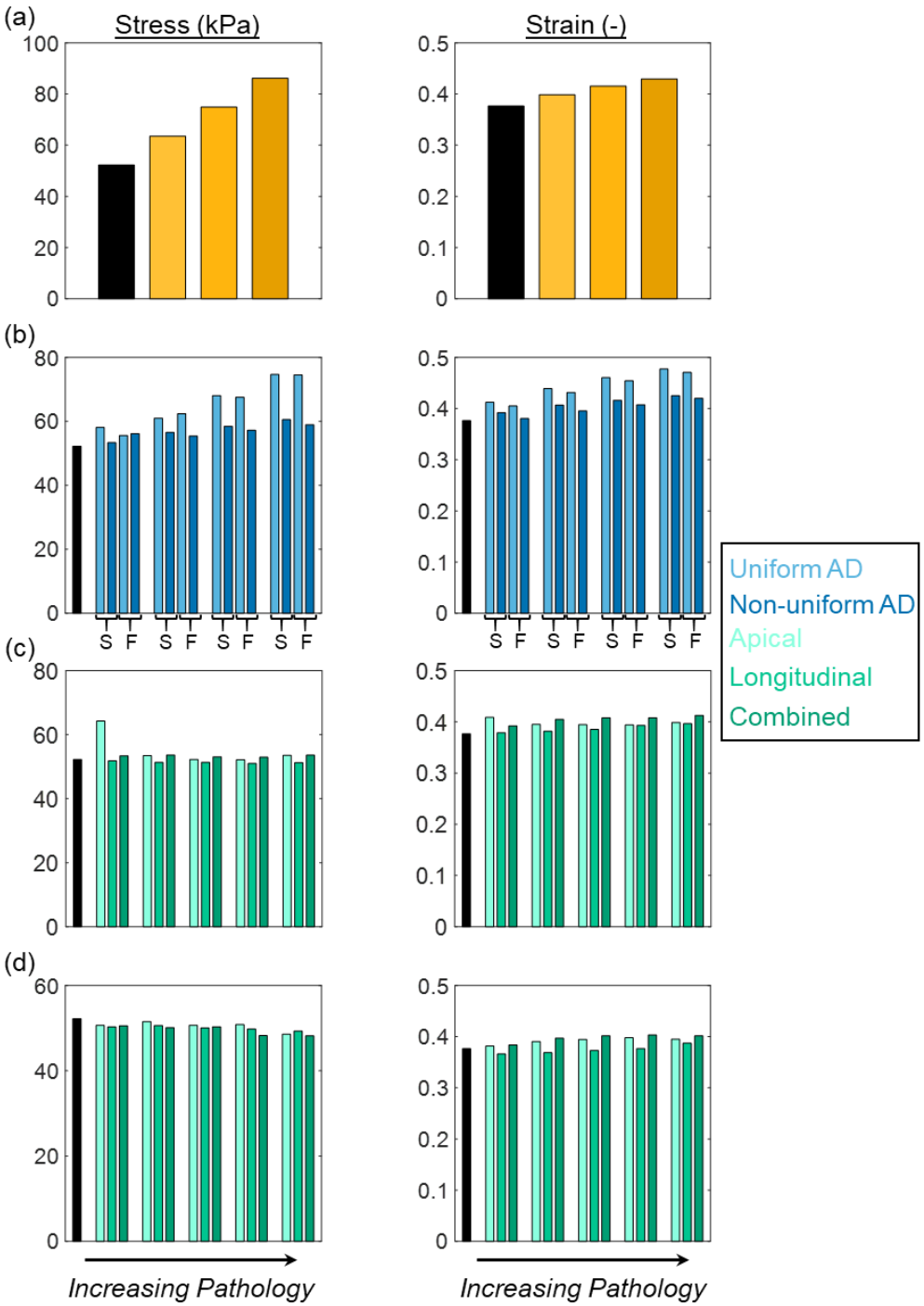

Figure 4-7: Results showing the incremental effects of (a) PH, (b) AD, (c) PM displacement – saddle annulus, and (d) PM displacement – flat annulus on the average von Mises stress (*left*) and the average maximum principle Green strain (*right*). S: saddle annulus; F: flattened annulus.

Finally, comparisons of the PM tip reaction forces are made between the simulation scenarios (Figure 4-8). For all scenarios, the uniform AD scenario had the largest increase in reaction force (+58%-170%) while the PM displacement scenario generally has the least change (5%-26%). Furthermore, the majority of the pathological study scenarios showed an increase in PM tip reaction force except for posterior-septal PM in the non-uniform AD of the saddle annulus and the anterior-septal PM in the PM displacement scenario for the flat annulus.

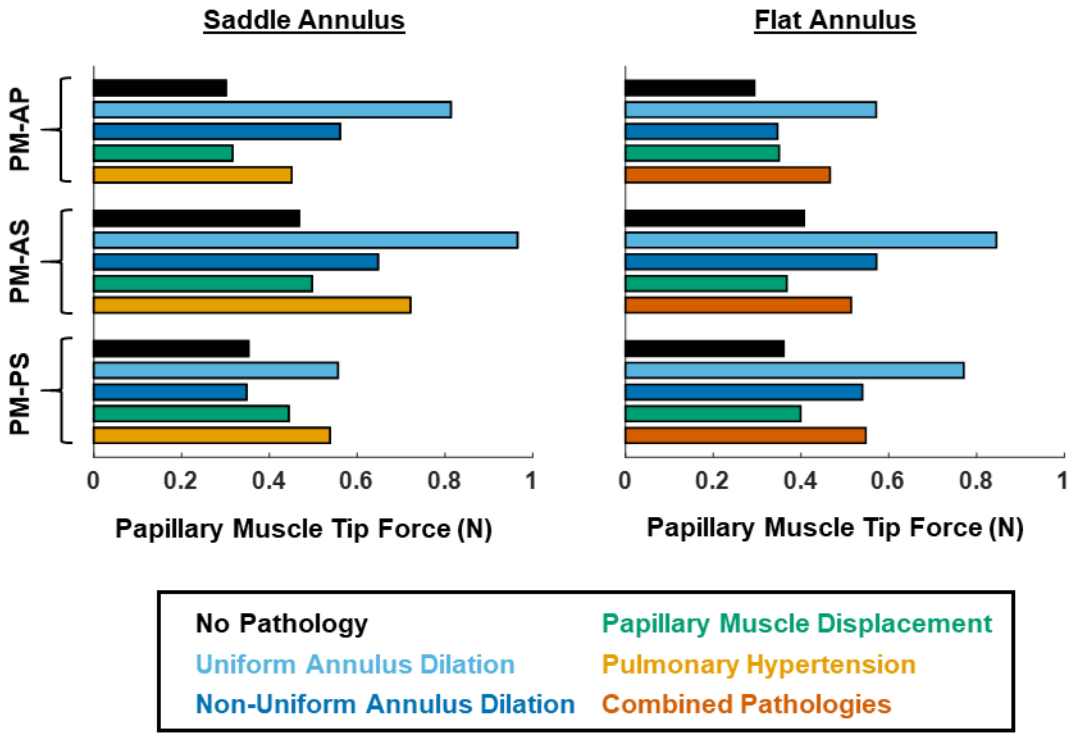

Figure 4-8: Comparison of the predicted PM tip reaction forces for various pathological study scenarios.

4.3 FE Simulation Results of Various Pathological Scenarios – Geometrical Metrics

Figure 4-5 illustrated the large variations in the closed TV geometry amongst the different study scenarios. A similar approach as outlined in Section 3.4.1 was followed to compare the geometrical metrics of the 9 slice views (3 per coaptation between two leaflets). Figure 4-9 presents the results for the saddle annulus configuration while Figure 4-10 presents the results for the flattened annulus configuration.

Different comparisons can be made from the results in Figure 4-9 or 4-10, but instead this section will focus on the key observations that may be more clinically relevant or impactful. The first key observation is that the uniform AD scenario commonly has a larger magnitude change compared to the non-uniform AD scenario. The larger magnitude is often something that is undesirable (e.g., an increase in the tenting area or a decrease in coaptation height), indicating that the non-uniform AD scenario may be more favorable. Second, the PH scenario typically has a decrease in the tenting area and the tenting height but an increase in the coaptation height. These changes demonstrate that PH causes the leaflets to make contact closer to the annulus plane and there is more contact between the leaflets. This alteration to the closing behavior of the leaflets is not something that directly contributes to the development of AD, which is typically an increase in the tenting area and a decrease in the coaptation height.

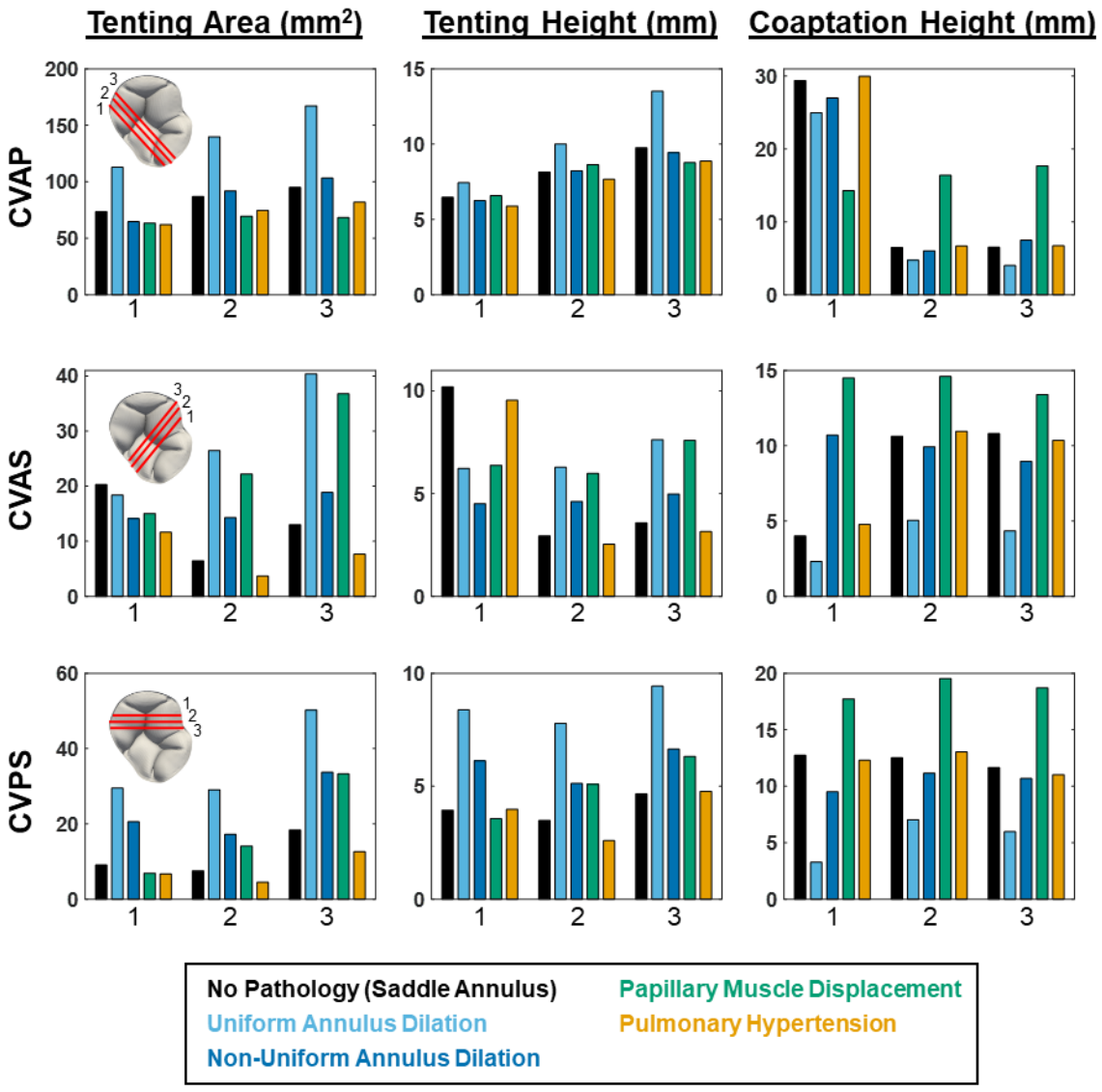

Figure 4-9: Cut-view results for all pathological scenarios considering the saddle annulus configuration. CVAP: cut view anterior-posterior; CVAS: cut view anterior-septal; CVPS: cut view posterior-septal.

Third, the non-uniform AD scenario generally has an increase in the tenting height and the tenting area, but a decrease in the coaptation height. This trend is the opposite of the PH scenario, suggesting that the non-uniform AD contributes to the development of the tricuspid regurgitation. Specifically, the leaflets are making less contact farther below the

TV annulus plane indicating that the leaflets are becoming tethered and eventually will be unable to fully close. The next major observation is that the PM displacement results in an increase in the tenting area, tenting height, and the coaptation height. This result is some interesting combination of the previous two, but it should be noted that the leaflets were stretched as a result of the apical PM displacement that could account for the increase in coaptation height. The increase in tenting area and tenting height suggest that the PM displacement may also contribute to the formation of TV regurgitation, similar to the non-uniform AD scenario. Finally, Section 4.2 showed that the mechanical changes associated with the *fully diseased scenario* do not represent a direct combination of all pathologies; however, for the geometrical values (Figure 4-10) it appears that the fully diseased scenario may more closely resemble a combination of all pathologies. For example, the CVAP-3 cut view shows the tenting area, tenting height, and coaptation height increase. It should be noted that the trends in the geometrical metrics for the fully diseased scenario appear to change between the selected cut views. This may imply that the interaction of these combined pathologies is complex, and one pathology may have more of an effect within a certain area of the closed TV geometry. For example, the CVAP cut view shows a decrease in the tenting area that is indicative of PH while the CVAS cut view has an increase in the tenting area that is representative of the AD and PM displacement scenarios.

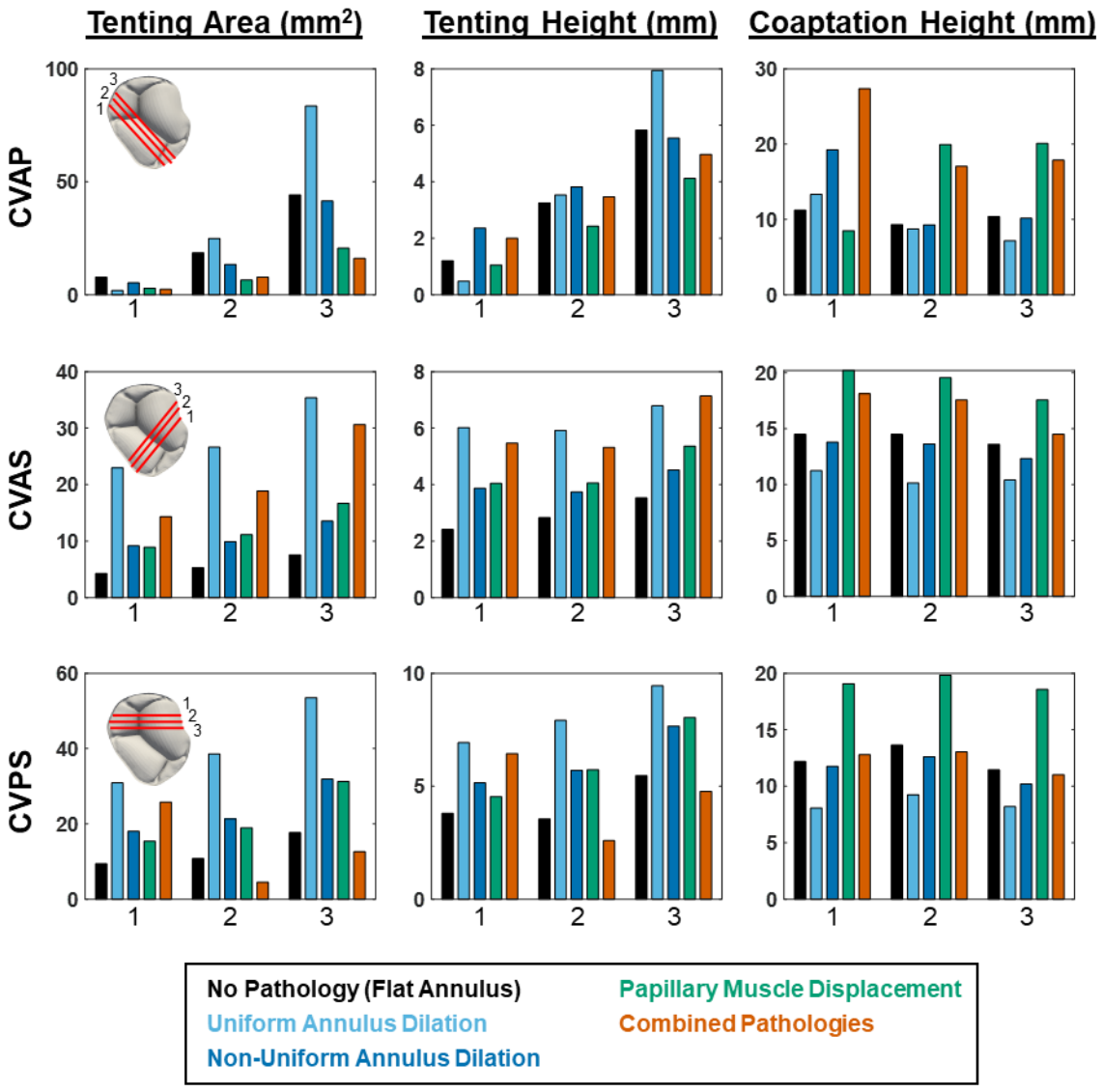

Figure 4-10: Cut-view results for all pathological scenarios considering the flat annulus configuration. CVAP: cut view anterior-posterior; CVAS: cut view anterior-septal; CVPS: cut view posterior-septal.

4.4 Chordae Rupture Scenario Results

The five chordae rupture scenarios that resulted in prolapse of the TV leaflets into the right atrium are presented in Figure 4-11. Two of these scenarios were the rupture of chordae

that were attached to the TVAL (C-3, C-4, and C-5) while the other three scenarios were the rupture of chordae attached to the TVSL (C-6, C-7, C-8, C-9). There were no scenarios where the rupture of chordae attached to the TVPL resulted in the leaflet prolapse.

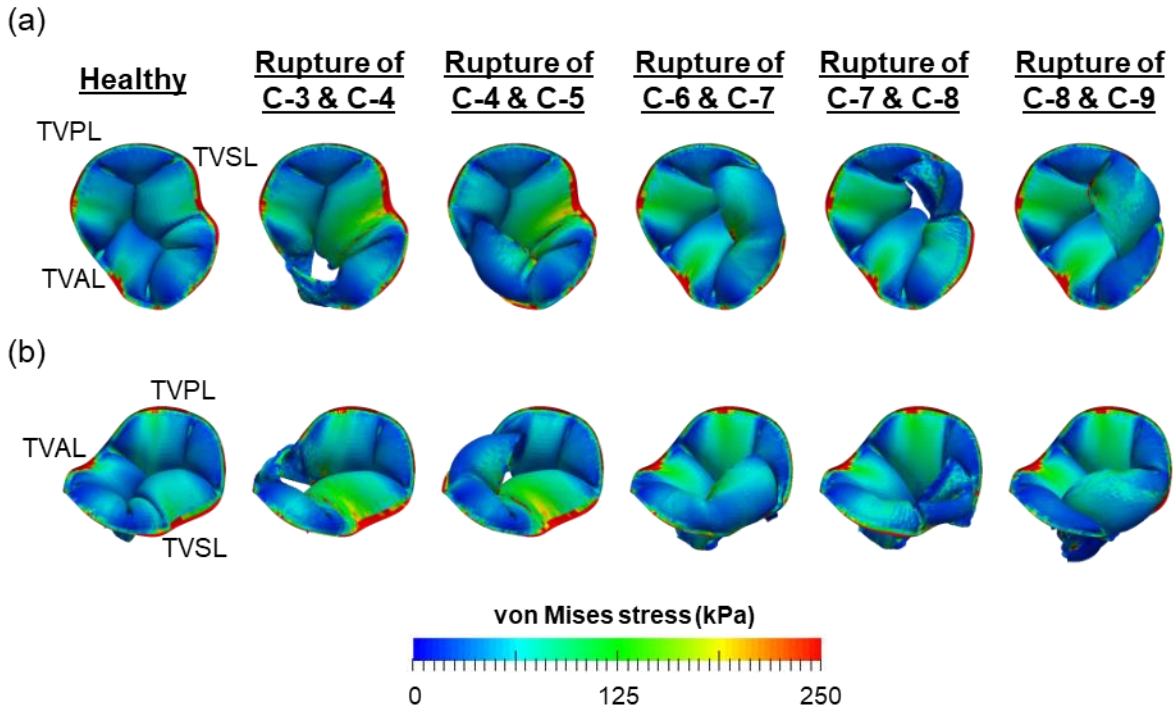

Figure 4-11: (a) Overhead view and (b) angled view of the five chordae rupture scenarios resulting in leaflet prolapse with comparison to the healthy simulation result.

It is important to note that all combinations of chordae rupture resulting in prolapse contained chordae that were next to one another. For example, there were no scenarios with prolapse where one chordae tendineae group attached to the TVSL and one chordae tendineae group attached to the TVPL were ruptured. Moreover, the leaflets that did not prolapse into the right atrium showed an increase in belly leaflet stress likely resulting from the unimpeded deformation of the tissue due to lack of contact with another surface. This was especially the case when the TVSL prolapsed into the atrium. When the TVAL

prolapsed, the high stress region near the annulus of the TVSL appeared to become slightly larger. Further *in vitro* studies would be necessary to understand how the rupture of these chordae also affect the dynamic motion of the annulus since it is evident the mechanical values near the annulus are changing.

4.5 Discussion

In this chapter, various pathological scenarios typically associated with functional tricuspid regurgitation were, *for the first time*, simulated in a systematic manner by using the FE model developed in Chapter 3. The scenarios of interest were: (i) PH, (ii) AD, (iii) PM displacement, (iv) a flattened TV annulus, (v) a combination of all pathologies, and (vi) chordae tendineae rupture. The FE simulation results for these scenarios (except for the chordae tendineae rupture) were analyzed to determine each individual pathology's effect on the mechanical stress and strain values of the leaflets and on the closed TV geometry. Key observations from these numerical studies include: (i) the combined effect on the mechanical values of each pathology demonstrated in the fully diseased scenario does not appear to be a simple combination of the independent parts, (ii) uniform AD generally had larger effects (+16%-47%) than the non-uniform AD (+13%-29%) on the mechanical values, (iii) the non-uniform AD and PM displacement scenarios showed changes in geometrical values (increased tenting area and tenting height) that indicate the formation of a regurgitant TV geometry, and (iv) the chordae tendineae associated with the TVAL and TVSL appear to have a higher potential, when ruptured, to allow for the TV leaflet prolapse. These results provide an improved understanding of how various pathologies alter the biomechanical function of the TV, *which has yet been done within an in silico*

framework in tricuspid heart valve biomechanics community.

Nevertheless, there are a handful of limitations that need to be addressed. First, the material model selected for the leaflets was transversely isotropic and assumed to be homogeneous across the leaflets. It is known that the atrioventricular heart valves are anisotropic, and Chapter 5 will demonstrate the regionally-varying mechanical properties of the TV leaflets. Therefore, it necessary to select a more accurate material model with optimal parameters determined through constitutive modeling as described in Chapter 6. Second, the annulus and PMs were assumed to be fixed, which is not representative of the *in vivo* behavior of these components. Future extensions are warranted to quantify and implement these dynamic motions. Third, before this model can be used in a *patient-specific* predictive method, extensive validations are needed to ensure the model is accurate in its predictions. Although the model works in its current form for providing a parametric survey of how those pathologies affect the TV biomechanical function, the refinements listed in the previous two points together with experimental validations will further enhance the predictability of our model. One other minor limitation includes considering only the bio-solid component of the TV and not considering the fluid-solid interactions. Future extensions for this work are addressed in Chapter 7.

CHAPTER 5 Biaxial Mechanical Characterizations of the Tricuspid Valve

Biaxial mechanical testing has previously been used to understand the biaxial mechanical response of porcine TV leaflets [51, 65] and human TV leaflets [108]. These studies revealed the TV leaflets behaved similarly to the MV as it was nonlinear and anisotropic with the circumferential direction being stiffer than the radial direction. However, the investigations involving the biaxial mechanical response of the TV leaflets are significantly limited compared to the MV or AV leaflets. For example, studies for the MV leaflets have investigated the viscoelastic properties (rate-dependent, stress-relaxation, and creep) and revealed the mechanical response was not rate-dependent and the tissue did not exhibit a significant creep behavior, but instead had a significant stress-relaxation response [46, 47]. Furthermore, studies for the AV leaflets investigated the mechanical properties of the distinct tissue layers [132] and the contributions of the GAGs to the AV leaflet mechanical response [34]. Therefore, the objective of this Chapter is to present our biaxial mechanical characterizations of the TV leaflets to address the lack of information. Specifically, the *baseline* biaxial mechanical responses including the rate, temperature, and species effects, the *regional variations* in the mechanical response, and the *GAG contribution* to the bulk leaflet mechanical response. First, the methods corresponding to each study are presented in Section 5.1, then the primary results/findings are presented in Section 5.2, and finally some discussion is provided in Section 5.3.

5.1 Methods

5.1.1 Tissue Acquisition

Healthy, adult porcine hearts (80-140 kg, 1-1.5 years of age, equal female: male ratio) were obtained from a local USDA approved slaughterhouse (Country Home Meat Co., Edmond, OK). Hearts were obtained on the same day of excision from the animal, promptly cleaned of clots, and placed in a freezer at -14 °C. This freezing-based storage procedure was adopted according to previous studies, which demonstrated a minimal effect of freezing on the mechanical properties of arterial and skin tissues [38, 133, 149]. For dissection, hearts were thawed, and the TV leaflets were excised (Figure 5-1a). For the baseline experiments, all three leaflets were excised while for the regional variations and GAG contribution study only the TVAL was excised. Next, the leaflets were laid flat and sectioned based on the investigation. The baseline and GAG contribution studies used a central 8mm x 8mm or 10 x 10 mm region (Figure 5-1b), respectively, while the regional variations study used six smaller (6 x 6 mm) regions (Figure 5-1c). The excision and sectioning procedure were repeated for adult ovine and juvenile ovine hearts for the baseline investigation. The sectioned tissue samples were then stored in phosphate-buffered saline (PBS) solution and refrigerated in a 4 °C environment for testing within two days of dissection. Prior to testing, the samples were removed from the PBS solution and the thickness was measured three times using a digital caliper and averaged for later stress calculations.

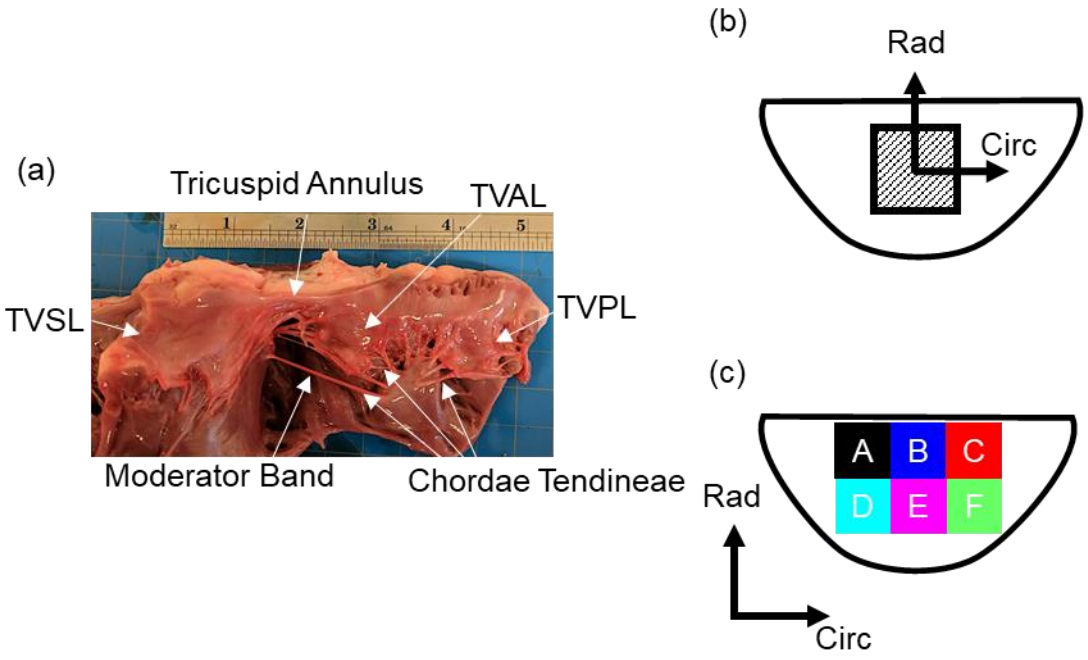

Figure 5-1: (a) Anatomy of the TV highlighting the three leaflets, (b) an illustration of leaflet segmentation for the baseline and GAG contribution investigations, and (c) an illustration of the six smaller sections excised for the regional variations investigation. Images were adapted from [59, 82].

5.1.2 Baseline Investigation

The sectioned porcine, adult ovine, or juvenile ovine samples were mounted to the biaxial mechanical testing system (BioTester – CellScale, Canada) (Figure 5-2a-b) by a set of five-tined Biorakes creating an effective edge length of 6.5 x 6.5 mm (Figure 5-2c). Care was taken to ensure the circumferential and radial direction aligned with the *x*- and *y*-axis of the system. Four small glass beads (300-500 µm diameter) were applied using super glue to the surface of the tissue in a square array for later digital image correlation (DIC) methods (cf. Section 5.1.5) (Figure 5-2c). The tissues were then submerged in a bath of PBS and

underwent an extensive biaxial mechanical characterization protocol (Figure 5-2d). The protocol consists of 8 preconditioning protocols, considering a preload of 1% of the maximum value, to ensure repeatable stress-stretch curves and 8 repetitions of various loading ratios (T_{circ}:T_{rad} = 1:1, 1:0.75, 0.75:1, 1:0.5, 0.5:1). T_{circ} and T_{rad} are the applied membrane tensions in the circumferential and radial directions.

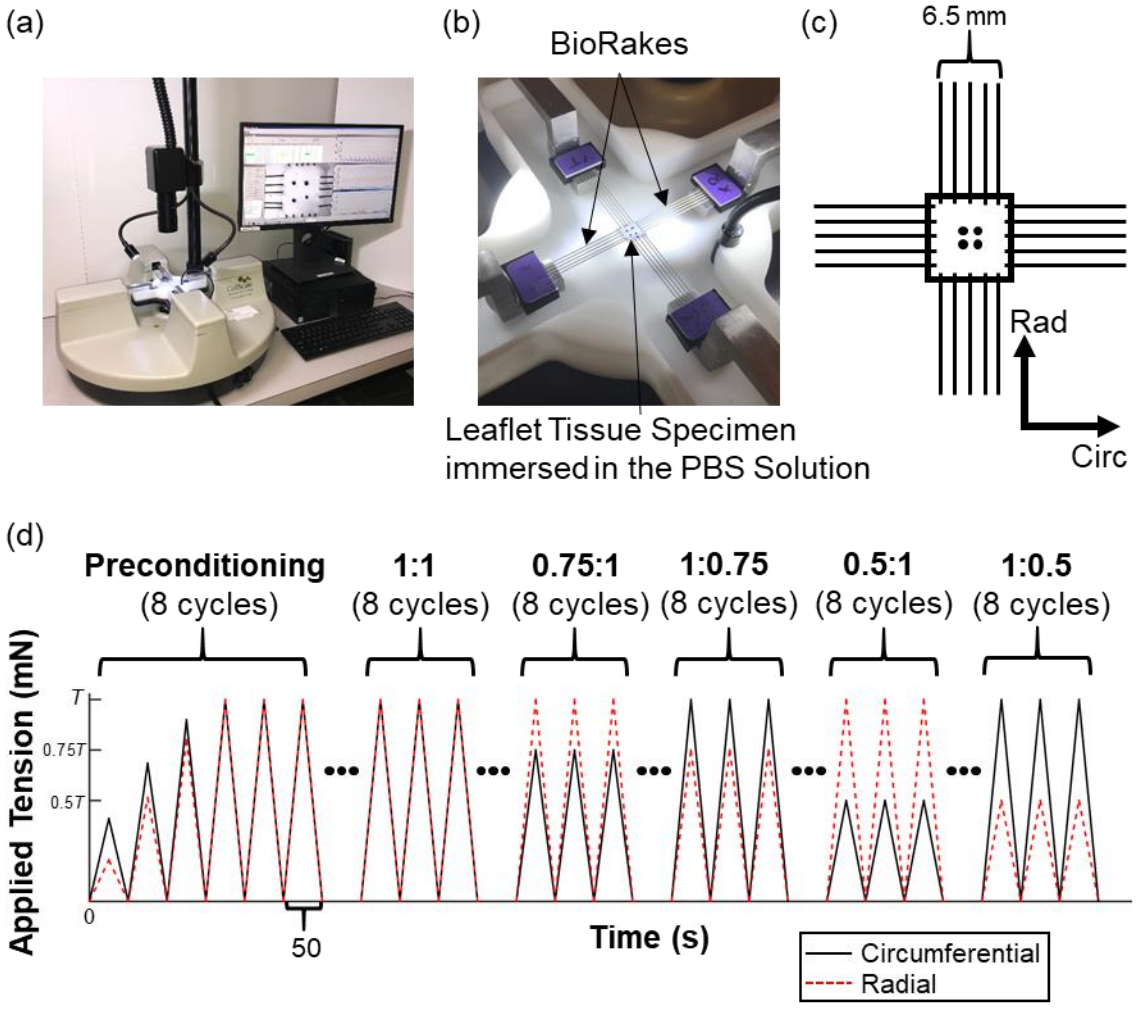

Figure 5-2: (a) CellScale BioTester system, (b) TV leaflet tissue mounted to the BioTester, (c) an illustration of the mounted tissue showing the four fiducial markers, and (d) a schematic of the extensive biaxial testing framework. Images were adapted from [59].

The peak membrane tensions ($T_{circ,max}$ and $T_{rad,max}$) were calculated by using the approximate *in vivo* stress (115 kPa for the TV leaflets), which was determined from the Laplace's Law for a spherical surface and the tissue's thickness. Specifically, for the Laplace's Law of a spherical surface, the TV leaflets were assumed to have a mean radius of curvature of 2 cm and a transvalvular pressure gradient of 40 mmHg [65]. Throughout the test, the Biorake separation distance and load cell force readings were continuously recorded while a series of 1280 x 960 pixel images were collected at 15 Hz. Two other testing scenarios were also tested besides the described baseline testing: (i) the temperature effect and (ii) the loading rate effect. To quantify the effect of temperature, the porcine heart valve tissues were tested at PBS temperatures of 27 °C, 32 °C, and 37 °C. For the loading rate effect, loading rates of 2.29 N/min, 4.42 N/min, and 7.92 N/min were tested. Results from these quantifications are presented in Section 5.2.1.

5.1.3 Regional Variations Investigation

The six smaller delimited regions of the TVAL tissue were mechanical tested to quantify the regional variations. To do so, each 6 x 6 mm specimen was mounted to the BioTester machine creating an effective edge length of 4 x 4 mm (Figure 5-3a). A four-node fiducial marker array was then created on the surface of the tissue using a surgical pen. Then, a two-step force-controlled biaxial testing procedure was used to characterize the mechanical behavior of the TVAL tissue regions (Figure 5-3b). First, a preconditioning protocol was used to restore the valve leaflet tissue to its *in vivo* configuration, in which $T_{circ,max}$ and $T_{rad,max}$ were applied in each direction at a rate of 2.29 N/min for 8 repeated loading/ unloading cycles with a preload as 2.5% of $T_{circ,max}$ and $T_{rad,max}$. Next, five varying loading

ratios ($T_{circ,max}$:$T_{rad,max}$ = 1:1, 0.75:1, 1:0.75, 0.5:1, and 1:0.5) with 8 loading/unloading cycles were employed to investigate all possible physiological tissue deformations.

All tests were performed in a bath of PBS at a temperature of 37 °C. Similar to the baseline testing, Biorake tine separation and load cell readings were continuously recorded while a series of 1280 x 960 pixel images were collected at a rate of 15 Hz using a high-resolution charge-coupled device (CCD) camera.

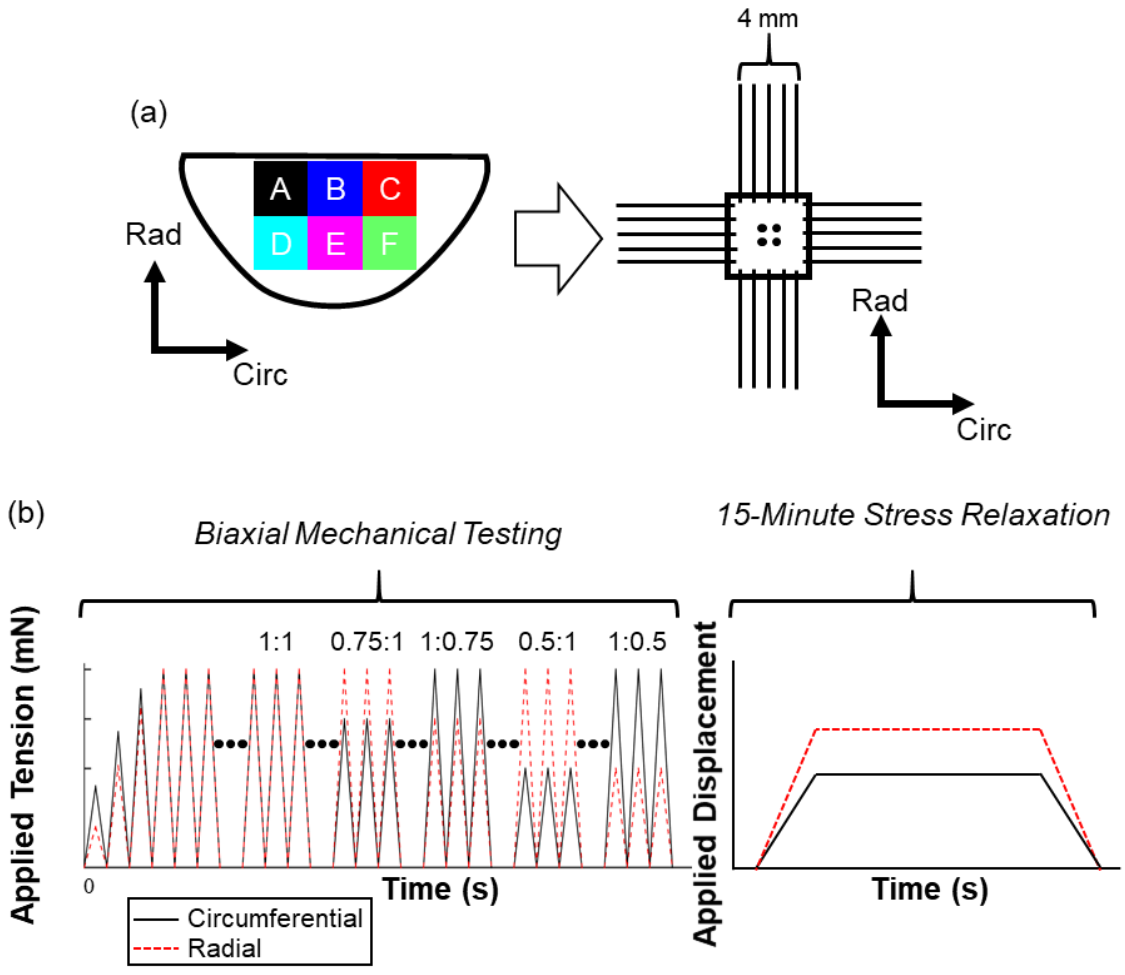

Figure 5-3: (a) An illustration of the six smaller tissue sections that are mounted to the BioTester, and (b) a schematic of the biaxial testing and stress relaxation testing. Images were adapted from [82].

Additionally, stress-relaxation testing was employed to observe the viscoelastic properties of each region. In the stress-relaxation testing, the tissue is loaded to $T_{circ,max}$ and $T_{rad,max}$ using the maximum displacements previously recorded. Then, the specimens were held to relax over 15 minutes and load cell readings were collected at a rate of 5 Hz. Results for this regional variation investigation are presented in Section 5.2.2.

5.1.4 GAG Contribution Investigation

This investigation aims to quantify the contribution of GAGs to the tricuspid valve leaflet mechanical response. Eckert *et al.* (2013) [34] previously quantified the contribution of GAGs to the *aortic valve* leaflet tissue's mechanical responses using an enzyme-based GAG removal method. In this study, Eckert *et al.* used different tissues for the "control" and "treated" groups, therefore introducing potential variances arising from different tissue specimens. Our investigation follows a similar enzyme-based GAG removal method but aims to address the limitation of Eckert *et al.* by using the same leaflet tissue before and after enzyme treatment. The details of this new three-step experimental method are discussed as follows.

A three-step experimental protocol was utilized to quantify the contribution of the GAGs to the TV leaflet mechanical response. First, the 10 x 10 mm samples were mounted to the biaxial testing system creating an effective testing size of 7 x 7 mm. A similar mechanical characterization protocol to the regional variation investigation was utilized with the only differences being the biaxial protocols used ($T_{circ,max}$:$T_{rad,max}$ = 1:1, 0.5:1, and 1:0.5), the number of cycles (n=10) per loading cycle, and the loading rate (4.42 N/min). Second, the

tissues were treated with an enzyme (Hyaluronidase type VI-S and Chrondroitinase ABS) for 100 minutes to remove the majority (>50%) of the GAGs. The removal of GAGs was quantified using an Alcian blue stain with typical histological methods. Third, the treated tissue was mounted to the system with an effective testing size of 5.5 x 5.5 mm to avoid effects from mounting prior to GAG removal treatment. The same mechanical characterization protocol that was used before the enzyme treatment was used again to determine differences in the tissue's mechanical response after GAG removal. Results from this investigation are presented in Section 5.2.3.

5.1.5 Stress and Strain Calculations

To quantify the strains of the tissue under the biaxial mechanical testing, the captured images were analyzed using the DIC-based technology in the LabJoy software of the BioTester system. This analysis method quantifies the time-dependent positions of the four fiducial markers as

$$\mathbf{x}_I(t) = \mathbf{X}_I + \mathbf{d}_I(t), \quad I = 1\text{-}4, \tag{5.1}$$

where the $\mathbf{X}_I$'s and the $\mathbf{x}_I$'s are the marker positions in the undeformed (reference) configuration and the deformed configuration, respectively, and the $\mathbf{d}_I$ is the displacement vector of the I^{th} fiducial markers. These time-dependent displacements were then used to calculate the corresponding in-plane tissue strain. In brief, the four fiducial markers were used as a four-node bilinear FE, and the deformation gradient tensor $\mathbf{F}$ was computed based on a previously-developed strain calculation [14, 119]

$$\mathbf{F} = \mathbf{F}(\mathbf{X}, t) = \frac{\partial \mathbf{x}}{\partial \mathbf{X}} = \begin{bmatrix} \sum_{I=1}^{4} B_{xI} u_I(t) & \sum_{I=1}^{4} B_{yI} u_I(t) \\ \sum_{I=1}^{4} B_{xI} v_I(t) & \sum_{I=1}^{4} B_{yI} v_I(t) \end{bmatrix}. \tag{5.2}$$

Here, B_{xI}'s and B_{yI}'s are the shape function derivatives associated with node *I* with respect to the *x*- and *y*-coordinates. The deformation gradient **F** was used to calculate the corresponding tissue stretches in the circumferential (λ_{circ}) and radial directions (λ_{rad}) by taking the square root of the principal values of the right Cauchy-Green deformation tensor $\mathbf{C} = \mathbf{F}^T\mathbf{F}$.

The experimental stretch values were decomposed to further elucidate the mechanical function of the valve. Previous studies have demonstrated a preconditioning effect that is an inelastic deformation of soft tissues within the first few cycles of loading [65], but they have not directly quantified the inelastic deformation. Therefore, the stretch values in all of the investigations were decomposed into (i) the *preconditioning stretch* (λ_{circ}^{0-1} and λ_{rad}^{0-1}) that is the deformation of the tissue from the mounted configuration (Ω_0) to the post-preconditioned configuration (Ω_1), (ii) the *mechanical stretches* (λ_{circ}^{1-peak} and λ_{rad}^{1-peak}) defined as the tissue deformation from the post-preconditioned configuration to the peak stretch, and (iii) the *peak stretch* (λ_{circ}^{0-peak} and λ_{rad}^{0-peak}) defined as the tissue stretch from the original mounting configuration to the peak loading. These three stretches have the following relationship

$$\lambda^{0-peak} = \lambda^{0-1}\lambda^{1-peak}. \tag{5.3}$$

To calculate the stress values at each kinematic state, the load cell values were transformed to the first Piola-Kirchhoff (first-PK) stress tensor **P** through

$$\mathbf{P} = \frac{1}{L \cdot t}\begin{bmatrix} f_{circ} & 0 \\ 0 & f_{rad} \end{bmatrix}, \tag{5.4}$$

where L is the specimen's effective edge length, t is the tissue thickness measured prior to the biaxial mechanical testing, and f is the load cell force reading. Other stress values can be calculated such as the second Piola-Kirchhoff (second-PK) stress tensor $\mathbf{S} = \mathbf{F}^{-1}\mathbf{P}$ or the Cauchy stress $\boldsymbol{\sigma} = J^{-1}\mathbf{P}\mathbf{F}^{T}$ for comparisons with different studies.

5.1.6 Statistical Analysis

Data, such as the TV leaflet tissue stretch, were expressed as mean ± standard error of the mean (SEM). Various comparisons were made for each investigation with statistical analyses to determine significance. The one-way analysis of variance (ANOVA) was used to make comparisons of the decomposed stretch values between the three TV leaflets (baseline investigation) and the six delimited tissue regions (regional variances investigation). Additionally, the non-parametric Mann-Whitney U test was used to make comparisons of the decomposed TV leaflet tissue stretches before and after enzyme treatment. In our statistical analyses, $p<0.05$ is considered *statistically significant*, while $0.05 \leq p < 0.10$ is considered *nearly statistically significant*.

5.2 Results

5.2.1 Baseline Investigation

Results from the baseline investigation for the three heart valve leaflets undergoing equibiaxial tension are provided in Figure 5-5. All leaflets had the nonlinear, anisotropic mechanical response expected for collagenous soft tissues. In general, the TV leaflets were more compliant than the MV leaflets at their respective physiological loadings in both the

circumferential and radial directions. For the TV leaflets, the TVSL was the most compliant in the circumferential direction (λ_{circ}^{0-peak} =1.374), the TVPL was the most compliant in the radial direction (λ_{rad}^{0-peak} =1.788), and the TVAL was the stiffest in both the circumferential and radial directions (λ_{circ}^{0-peak} =1.210 and λ_{rad}^{0-peak} =1.651).

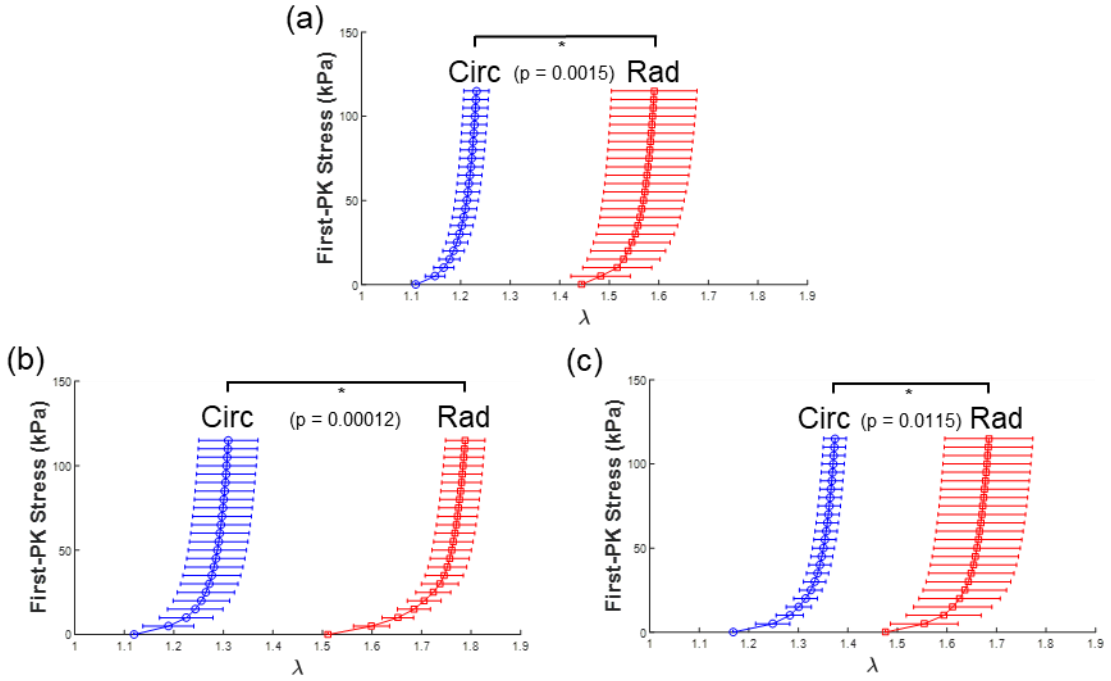

Figure 5-4: Baseline biaxial mechanical characterization results for the (a) TVAL, (b) TVPL, and (c) TVSL. * denotes statistically significant. Images were adapted from [59].

Comparing the mechanical response of the tissues under the different loading rates (Figure 5-6), three observations could be drawn from the results. (i) The preconditioning stretches increase as the loading rate increases in the radial direction (+4.7%, p=0.424). (ii) The mechanical stretches decrease as the loading rate increases in the circumferential (-2.0%, p=0.587) and radial (-2.6%, p=0.576) directions. (iii) With an increased loading rate, the

circumferential peak stretch decreases (-1.6%, p=0.728) while the radial peak stretch increases (+2.0%, p=0.823). These results suggest the tissues have a slight dependence on the loading rate.

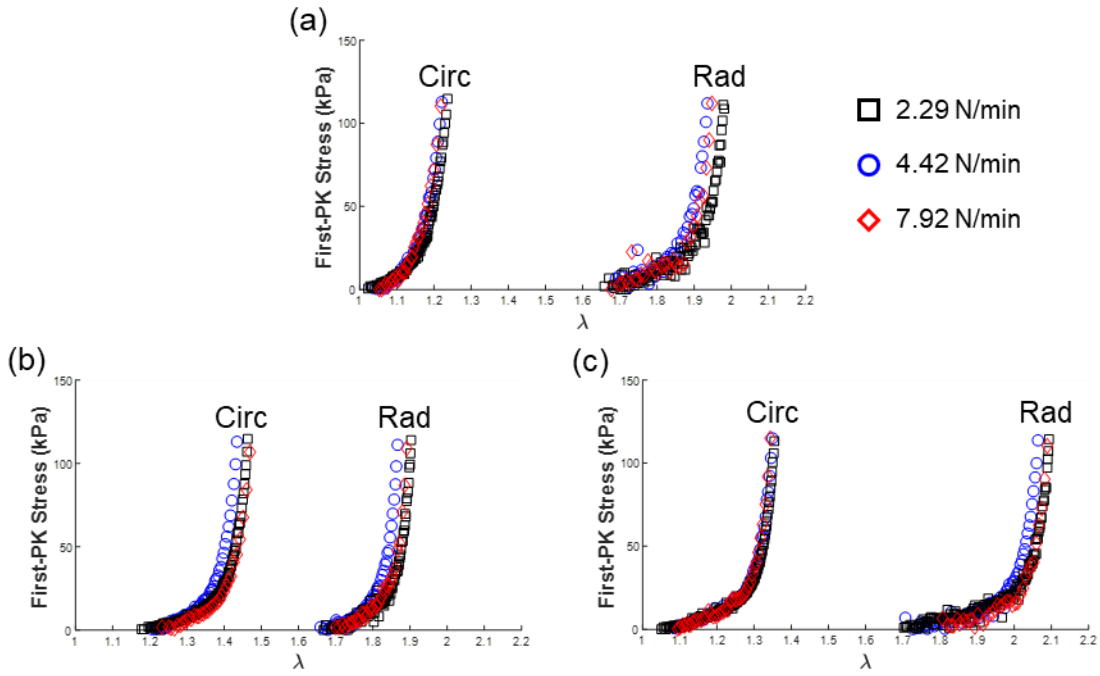

Figure 5-5: Representative biaxial mechanical characterization results demonstrating the effect of loading rate on the (a) TVAL, (b) TVPL, and (c) TVSL mechanical response. Images were adapted from [59].

The results from the varying temperature depended on the stretch component and the tissue's preferred fiber orientation direction (Figure 5-7). However, three observations could be made: (i) increasing temperature resulted in a decrease of the circumferential (-3.4%, p=0.275) and radial (-3.7%, p=0.623) preconditioning stretch; (ii) the mechanical stretches increased in the radial direction (+26.6%, p=0.623); and (iii) the peak stretches appeared independent of the testing temperature. These interesting trends suggest the necessity of keeping the testing temperature constant throughout and between tests and

using the physiological temperature to more accurately capture the biaxial mechanical response.

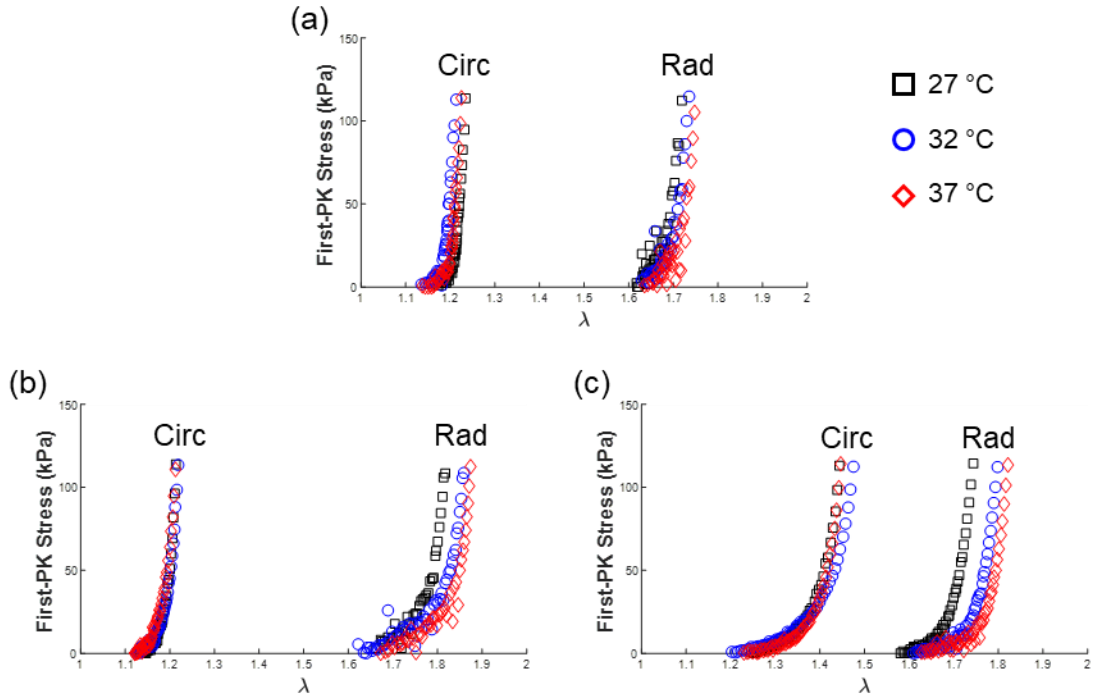

Figure 5-6: Representative biaxial mechanical characterization results demonstrating the effect of temperature on the (a) TVAL, (b) TVPL, and (c) TVSL mechanical response. Images were adapted from [59].

The mechanical response of the TV leaflets for different species did not have a consistent trend (Figure 5-8). For the leaflet-specific trends: (i) the circumferential preconditioning stretches were *significantly* lower for the porcine TVAL than the adult (-16.5%, p=0.028) and juvenile (-21.3%, p=0.010) ovine TVAL, (ii) the radial preconditioning stretches were *significantly* lower for the porcine TVAL compared to the adult ovine (-11.5%, p=0.057) and juvenile ovine (-14.5%, p=0.040) tissues and (iii) the juvenile ovine tissues had larger preconditioning stretches compared to the adult ovine tissues (λ_{circ}^{0-1} : +6.1%, p=0.522; λ_{rad}^{0-1} : +3.5%, p=0.555). These results indicate the mechanical properties may become stiffer

with age and there are variances amongst different species, which should be considered when selecting tissues for mechanical characterization.

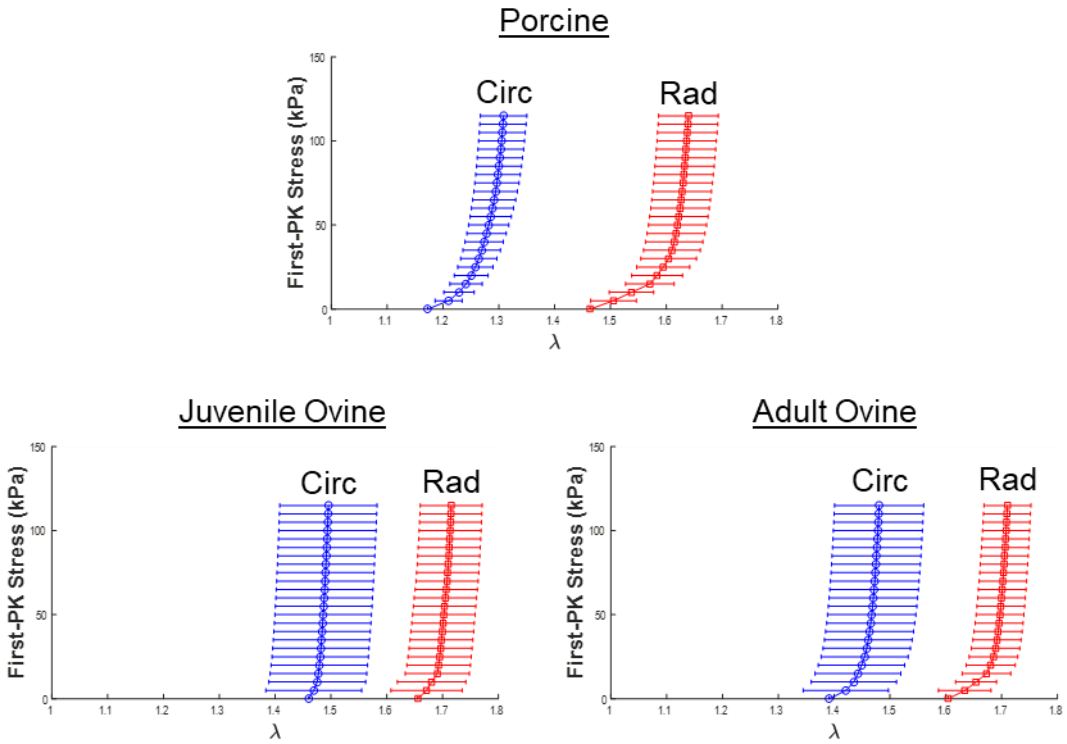

Figure 5-7: Biaxial mechanical characterization results demonstrating the tissue response of two different species (porcine and ovine) and two different age groups (juvenile and adult). Images were adapted from [59].

5.2.2 Regional Variations

Membrane tension-stretch plots for the six tested regions are provided in Figure 5-9. One will quickly notice that the mechanical response of the six regions are noticeably different. Comparing the anisotropy index (ratio of the peak radial stretches to the peak circumferential stretches) between the six regions, the central regions (i.e., Regions B and E) are more anisotropic than the edge regions (i.e., Regions A, C, D, and F). This

comparison was also supported by observing the central regions had a greater difference *peak tissue stretch* in the circumferential and radial directions (0.107-0.12) than the edge regions (0.01-0.07) for the TVAL.

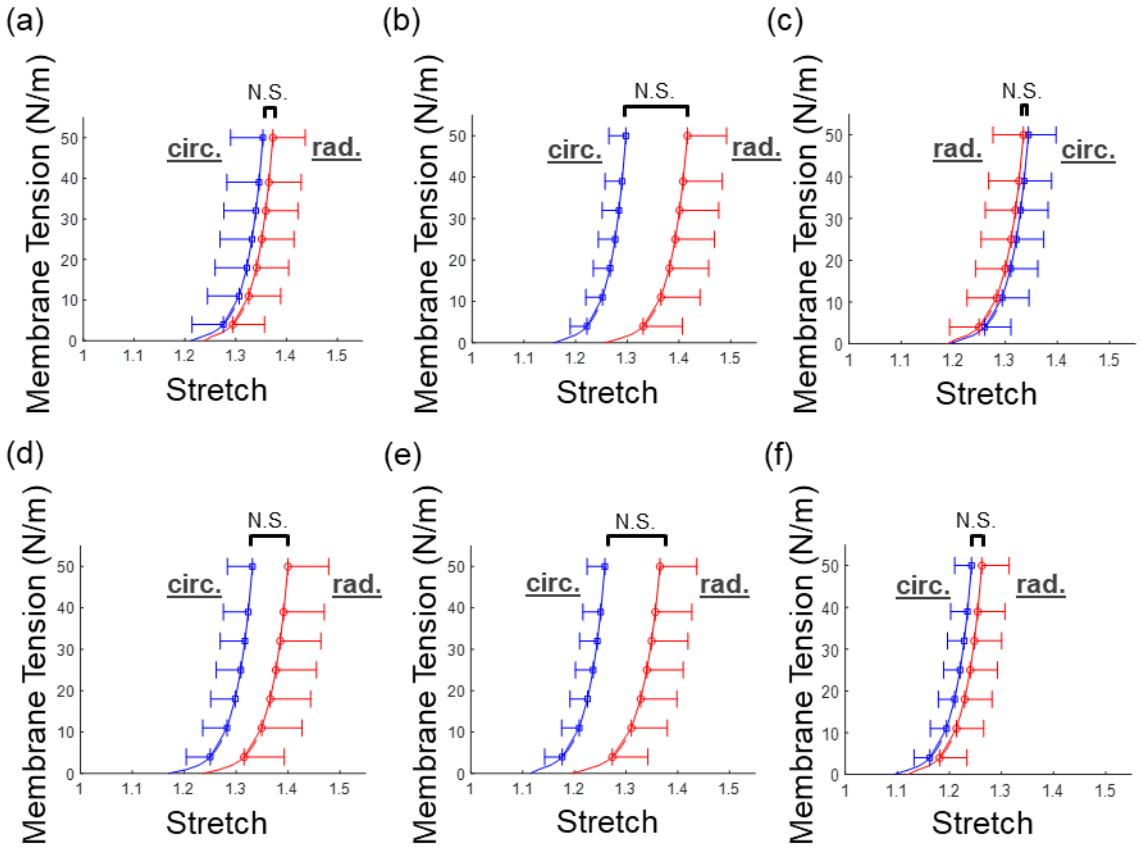

Figure 5-8: Biaxial mechanical characterization results for the six smaller tissue regions of the TVAL. N.S. denotes not significant. Images were adapted from [82].

The stress relaxation results for the six tested regions are provided in Figure 5-10. The central regions appeared to have differences in the stress relaxation behavior compared to the edge regions, but it was not found to be statistically significant. The results from these two types of mechanical characterizations indicate that the mechanical response is heterogeneous and does vary across the leaflet tissue. Further discussion of the results for this study are provided in Section 5.3.2.

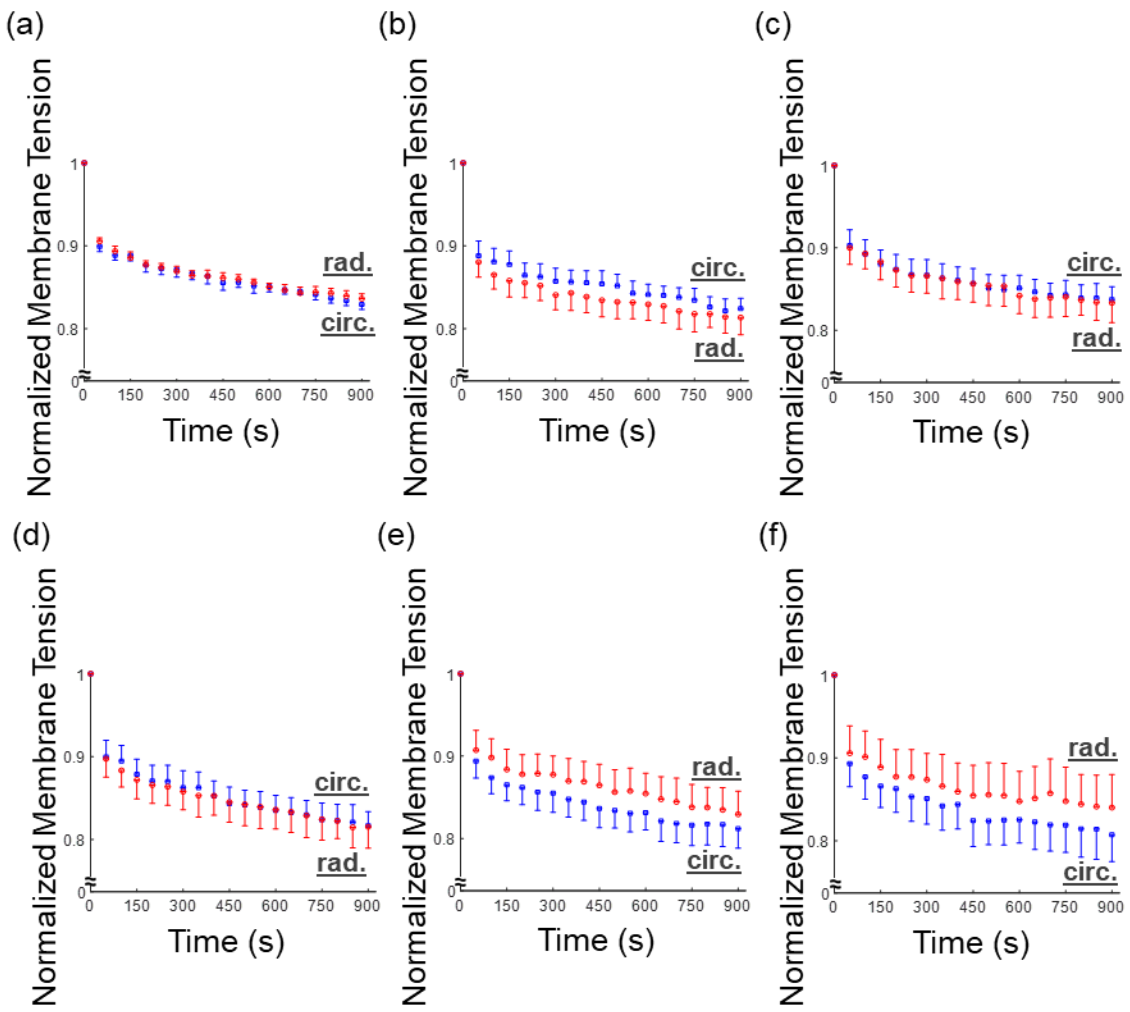

Figure 5-9: Stress relaxation testing results for the six smaller regions of the TVAL. Image were adapted from [82].

5.2.3 GAG Contribution to the TV Mechanics Responses

Images of the Alcian blue-stained TV tissues at 20-minute intervals until 120 minutes of treatment time are provided in Figure 5-11. One will notice the GAGs (stained in blue) are quickly removed from the tissue before it appears the treatment stagnates.

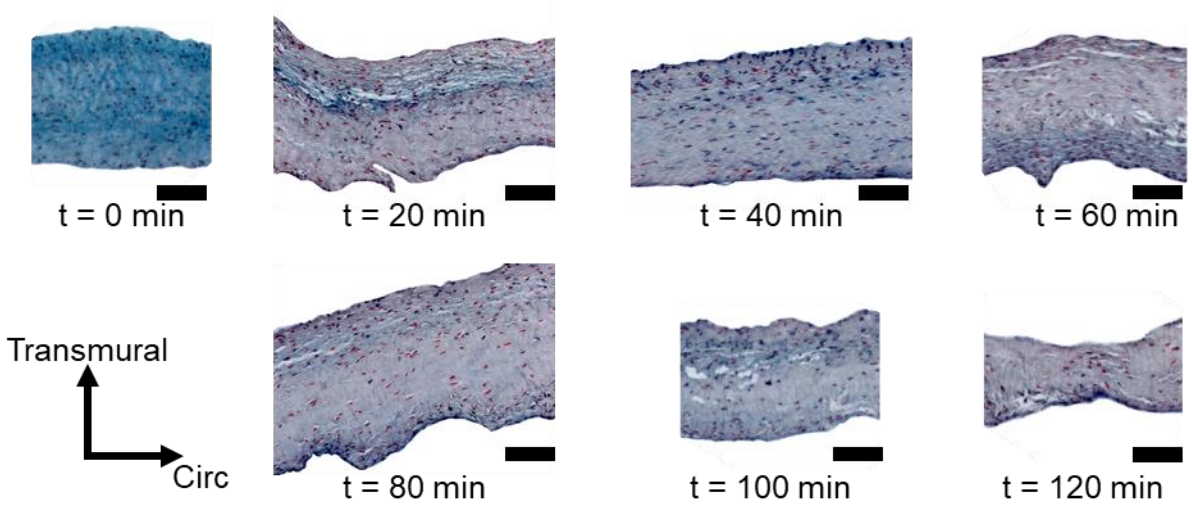

Figure 5-10: Alcian blue-stained histological images demonstrating the progression of the GAG constituent removal associated with various enzyme treatment durations. Scale bar = 100 μm.

The corresponding quantitative values for the removal of the GAG constituents of the TVAL tissues are provided in Table 5-1. The enzyme removal process achieves >50% removal after 20 minutes of treatment, but we elected to use a longer treatment time (100 minutes) to ensure that all of the GAGs were removed from the TVAL tissues.

The removal of GAGs had a significant effect on the biaxial mechanical response of the TV leaflet tissues (Figure 5-12). The peak tissue stretches were shown to be larger in both tissue directions for the treated tissues compared to the control tissues. The percent difference in the circumferential peak stretch was 4.7% ($p=0.132$), whereas the percent difference in the radial peak stretch was 7.6% ($p=0.015$). This trend was also observed in the non-equibiaxial protocols.

Table 5-1: Percentage of glycosaminoglycans in the control and enzyme-treated tissue strips over a 160-minute treatment time. All quantities are reported as mean ± SEM.

Time (minutes)	GAGs in Tissue Strip (%)	Tissue Strip Thickness* (mm)	GAG Reduction w.r.t. Control (%)
0 (Control)	45.16 ± 1.08	0.126 ± 0.003	—
20	16.94 ± 2.57	0.179 ± 0.060	62.49
40	11.66 ± 0.64	0.124 ± 0.004	74.19
60	14.31 ± 0.88	0.259 ± 0.006	68.30
80	13.11 ± 1.10	0.296 ± 0.010	70.97
100	17.50 ± 0.93	0.224 ± 0.008	61.24
120	11.63 ± 1.04	0.168 ± 0.018	74.24
140	17.61 ± 1.23	0.267 ± 0.015	61.00
160	17.32 ± 1.99	0.478 ± 0.013	61.65

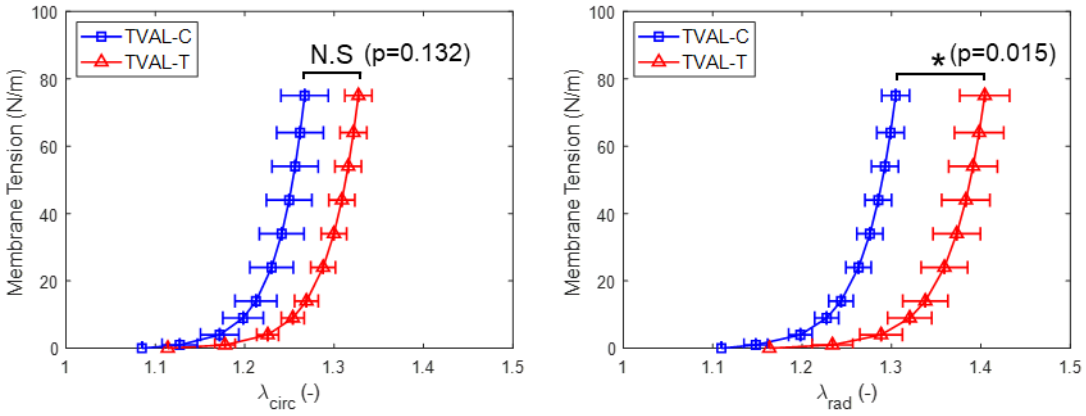

Figure 5-11: Biaxial mechanical characterization results of the GAG contribution investigation for the TVAL in the circumferential and radial directions. N.S. denotes staistically non-significant, and * denotes statistically significant. Images were adapted from [115].

Similarly, the preconditioning stretches were shown be greater post-treatment for both the circumferential and radial directions. The percent difference in the radial preconditioning

stretch was 2.7% greater (p=0.310), whereas the percent difference in the circumferential preconditioning stretch was 4.8% greater (p=0.048). Finally, the same trend was observed for the mechanical stretches with an increase in value post-treatment. The percent difference in the circumferential mechanical stretch was 2.0% (p=0.240), while for the radial direction it was 2.6% (p=0.329). Like the peak stretches, this trend was consistent across all tested protocols.

The results for the stress relaxation testing before and after enzyme treatment are provided in Figure 5-13. It was found that the control tissues had a larger stress reduction than the treated tissues in both directions for the TVAL. Specifically, there was a nearly statistically-significant difference in the pre- and post-treatment stress-relaxation behaviors in the circumferential direction (C: 17.1% relaxation, T: 15.0% relaxation, p=0.065) and in the radial direction (C: 16.4% relaxation, T: 14.5% relaxation, p=0.065). Further discussions of these results are provided in Section 5.3.3.

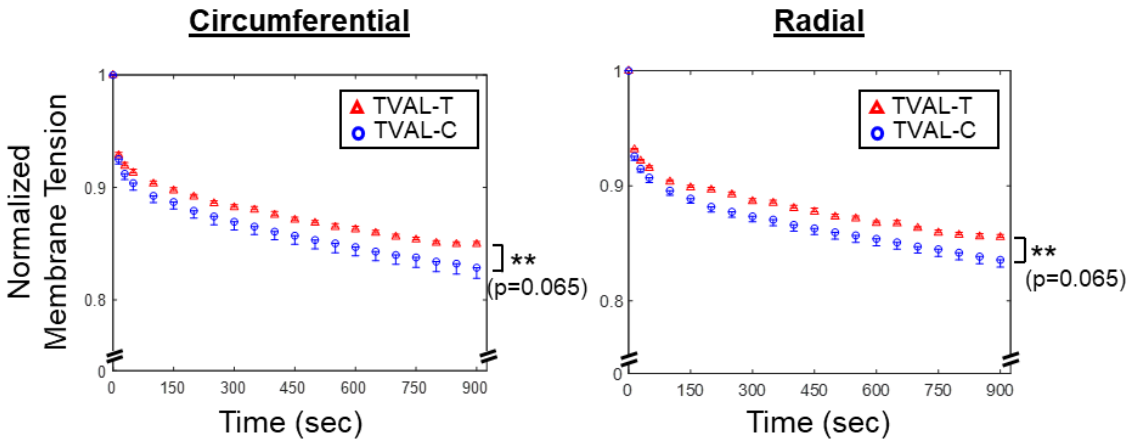

Figure 5-12: Stress relaxation testing results of the GAG contribution study for the TVAL in the circumferential and radial directions. ** denotes nearly statistically significant (0.05<p<0.10). Images were adapted from [115].

5.3 Discussion

There were a few limitations shared among all investigations. First, all TV tissues were stored using a freezing-based method, which has been shown to have negligible effects on arterial and skin tissues but has not been investigated for AHV leaflet tissues [38, 133, 149]. Second, the effective testing size for each study was different, and this potential effect has not been investigated. Third, the deformations within the fiducial markers was assumed to be homogeneous. Additionally, the deformation calculations within this region were assumed to have negligible shear stress that may arise from improper alignment of the BioRake attachments. Fourth, a 15-minute hold time was used for the stress relaxation testing. Previous studies have shown that 4-hours may be appropriate to show the full relaxation behavior, but for our studies, the 15-minute time frame was able to successfully reveal the differences. Finally, the caliper thickness measurements presented in the studies could depend on the amount of force applied during the measurement. Nevertheless, in our study we have shown that the dial caliper method agrees well with the thickness measurements quantified using histological measurements in Jett *et al.* (2018) [59]. Investigation-specific limitations (specifically for the GAG contribution investigations) and conclusions are provided in the sub-sections below.

5.3.1 Baseline Investigations

In this study, the response of each porcine atrioventricular leaflet has been thoroughly characterized. Our comprehensive results suggest the porcine TVPL was the most compliant in the radial direction, the TVSL was the most compliant in the circumferential

direction, and the TVAL and TVPL had the same anisotropy that was larger than the TVSL. These findings also suggest the necessity of employing different constitutive model parameters to describe the distinct mechanical behavior of each individual atrioventricular valve leaflet, rather than assuming homogeneous mechanical properties between leaflets. Moreover, we have demonstrated an increased loading rate is associated with a stiffer mechanical response, and increased temperature yields directionally-specific differences in the tissue stretches. We have also provided a novel quantification of the distinct mechanical responses of porcine and ovine leaflets and quantified the difference in leaflet mechanical response between different species and between juvenile and adult animals.

5.3.2 Investigation of Regional Variations

This research has, *for the first time*, examined the regional variance and similarity of the mechanical properties of the AHVs. The biaxial mechanical testing results in this study have demonstrated a significant difference in the material anisotropy when comparing the central tissue regions to the edge regions. Variance was observed in the peak mechanical stretch across the six tissue regions. Our stress relaxation results have further showed an anisotropic, exponential stress decay trend with variations in the stress reduction between tissue regions. Our novel experimental findings could provide a better understanding of the regionally-varying mechanics of AHVs and open the door to future refinement of computational models for accurately predicting diseased or surgically-intervened condition, where tissue heterogeneity plays an essential role in the valve function.

5.3.3 GAG Contributions to the TV Mechanical Behavior

Two limitations exist primarily for this investigation that were not described at the beginning of this section. First, although not emphasized in the methods of this section, the optimal enzyme treatment time was determined from treating different tissue strips with the enzyme to observe the percentage of GAGs removed. This has inherent limitations as our regional variation investigation demonstrated that the tissue has regionally-varying mechanical response (cf. Section 5.2.2), which indicates a heterogeneous tissue microstructure. This inherent regional heterogeneity may slightly affect the actual percentage of GAGs removed, but a time point was selected after >50% GAGs were removed to ensure this threshold was met for all tissues. Second, not all of the GAGs were removed (only 61-75%) for the post-enzyme mechanical testing, so the full contribution of the GAGs not captured. Nevertheless, removing the majority of GAGs in the tissue revealed a statistically-significant "softening" of the mechanical response.

By studying the effects of the GAGs on overall leaflet mechanical function, a new contribution has been made to detailing the complex microstructure of the atrioventricular heart valve leaflets. It was found that the GAGs play a notable role in the mechanical characteristics of the TVAL. Specifically, our results demonstrated: (i) under biaxial mechanical testing, tissues with GAGs removed had greater extensibility; (ii) under stress relaxation tests, tissues with GAGs removed had a lessened stress decay behavior. Because of the differences observed in untreated and enzyme-treated specimens, future investigations may be warranted into the GAG contributions of the other AHV leaflets' mechanical behaviors. Findings from this study will be useful in expanding the

understanding of the leaflet microstructure that may be used in the refinement of computational models of the AHV. Specifically, this information can be used for refining existing microstructure-based constitutive models [17, 55, 56, 73, 84-86, 105, 113, 120, 134] or growth and remodeling framework for soft tissues [3, 58]. These models could then be employed, with moderate future extensions, for predictive simulations of the AHV function and to inform improved valve replacement therapeutics.

CHAPTER 6 Constitutive Modeling of the Tricuspid Valve Biaxial Mechanical Response

Few studies exist for determining the optimal constitutive model parameters for the TV leaflet mechanical response under various loading scenarios. Furthermore, no study exists that provides a thorough examination of how effectively the common SEDFs in literature can model the TV leaflet mechanical response. The first study to attempt constitutive modeling for the TV leaflets was Heyden *et al.* (2015) [51]. The authors modeled the equibiaxial and uniaxial loading protocols using the following SEDF

$$W = C(I_1 - 3) + \sum_{i=1}^{N} G_i \left(\left| I_{4,i} - 1 \right| \right)^{\alpha_i}, \tag{6.1}$$

where C is the extracellular matrix stiffness, G is the fiber stiffness, α is the exponent constant, i denotes the i^{th} fiber family, and I_1 and I_4 are the first and fourth invariants. They were able to obtain excellent fits of both the uniaxial and equibiaxial loading scenarios. The second study was Aversa and Carredu [6] in which the authors fit the equibiaxial loading data for human tissues (Pham *et al.* (2017) [108]) to the following SEDF [83]

$$W = C_{10}\left(I_1 - 3\right) + \frac{c_0}{2}\left\{\delta \exp\left[c_1\left(I_1 - 3\right)^2\right] + \left(1-\delta\right)\exp\left[c_2\left(I_4 - 1\right)^2\right] - 1\right\}, \tag{6.2}$$

in which C_{10}, c_0, c_1, and c_2 are material constants, δ describes the alignment of the collagen fibers about the preferred orientation (δ=1 is purely isotropic; δ=0 is purely anisotropic), and $I_1 = trace(\mathbf{C})$ and $I_4 = \mathbf{N}\bullet\mathbf{C}\bullet\mathbf{N}$ are the first and fourth strain invariants. They obtained excellent fits of the equibiaxial data and subsequently used the SEDF and the optimal parameters in their computational modeling study. The third study by Kong *et al.* (2018)

[71] used the popular HGO SEDF proposed by Gasser *et al.*(2005) [44]

$$W = \frac{c}{2}\left(I_1 - 3\right) + \frac{k_1}{2k_2}\left[\exp\left\{k_2\left[\kappa I_1 + \left(1-3\kappa\right)I_{4i} - 1\right]^2\right\} - 1\right], \tag{6.3}$$

where c, k_1, and k_2 are the same material constants, κ describes the material anisotropy, and i denotes the fiber family of interest (i=1-2). Similar to the previous two studies, Kong *et al.* only fit the data to the equibiaxial loading protocol, and likewise obtained an excellent fit for the data. The fourth, and most comprehensive study, by Khoiy *et al.* (2018) [67] investigated the following SEDF

$$W = \frac{c}{2}\left(\exp\left\{a_1 E_{CC}^2 + a_2 E_{RR}^2 + 2a_3 E_{CC} E_{RR}\right\} - 1\right) \tag{6.4}$$

Here, c, a_1, a_2, and a_3 are material constants, and E_{cc} and E_{rr} are the circumferential and radial Green strains, respectively. Khoiy *et al.* used this SEDF to model their previous biaxial mechanical data for porcine TV leaflets. They were able to obtain an excellent fit (R^2>0.85) of the five protocols (T_{circ}:T_{rad} = 1:1, 1:0.75, 0.75:1, 1:0.5, 0.5:1) for the three TV leaflets. These four constitutive modeling studies do have their drawbacks or limitations. The first three studies presented were only fitting the equibiaxial data set, which our preliminary studies show is quite easy for most nonlinear, anisotropic SEDFs. In fact, the difficulty is being able to effectively capture all the possible biaxial or uniaxial loading protocols. The study by Khoiy *et al.* was more comprehensive in this sense as they looked at five different loading protocols, but seminal work by Sacks *et al.* (2000) [119] demonstrated that more protocols may be needed (T_{circ}:T_{rad} = 1:1, 0.5:1, 1:0.5, 0.333:1, 1:0.333, 0:1, and 1:0) to accurately capture the mechanical response. Also, Khoiy *et al.* only considered one Fung-type SEDF and did not investigate other possible SEDFs to determine which is the most effective. Therefore, the objective of this chapter is to develop

a constitutive modeling framework for modeling the TV biaxial mechanical response. The developed framework is developed in a way to easily allow for investigations of different SEDFs and combinations of loading protocols. Section 6.1 provides the general overview of the constitutive modeling framework; Section 6.2 discusses the DEO portion of the framework; Section 6.3 presents preliminary results using two common SEDFs; Section 6.4 concludes with some discussion of the results.

6.1 Constitutive Modeling Framework

The assumptions made for the constitutive modeling framework presented within this sub-section include: (i) the material is hyperelastic, incompressible, and transversely isotropic, (ii) the SEDF is either strain-based or invariant-based, and (iii) the tissue is undergoing biaxial tension. Based on the hyperelasticity theory, the stress of the material can be related to the strain through

$$\mathbf{S} = \frac{\partial W}{\partial \mathbf{E}} = 2\frac{\partial W}{\partial \mathbf{C}} = 2\sum_i \frac{\partial W}{\partial I_i(\mathbf{C})}\frac{\partial I_i(\mathbf{C})}{\partial \mathbf{C}} \ . \tag{6.5}$$

Here, **S** is the second Piola-Kirchhoff stress tensor, **E** is the Green-Lagrange strain tensor, **C** is the right Cauchy-Green deformation tensor, W is the strain energy density, and I_i denotes the i^{th} invariant of **C**. The right-hand side of Eq. (6.5) can be simplified to

$$\mathbf{S} = 2\left(W_{,1} - I_1 W_{,2}\right)\mathbf{I} - 2W_{,2}\mathbf{C} - p\mathbf{C}^{-1} + 2W_{,4}\mathbf{N}\otimes\mathbf{N} \tag{6.6}$$

$$p = \left[2(W_{,1} - I_1 W_{,2}) - 2W_{,2}C_{33}\right]\left(C_{33}^{-1}\right)^{-1}, \tag{6.7}$$

where $W_{,i}$ denotes the derivative of the strain energy density with respect to the i^{th} invariant of **C**.

The constitutive modeling framework follows an iterative approach to estimate the optimal parameters for a given SEDF. A detailed flow chart of this is provided in Figure 6-1.

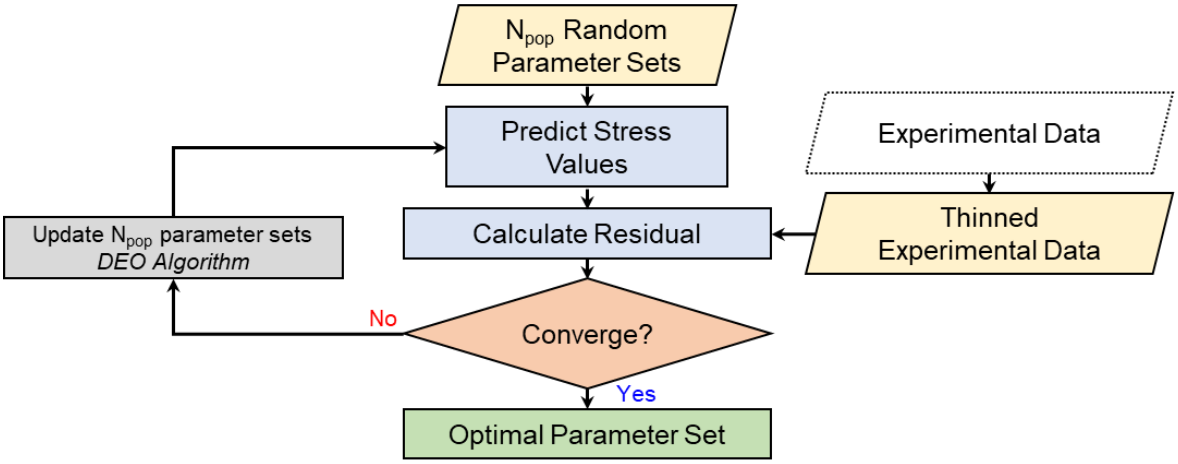

Figure 6-1: Schematic of the constitutive modeling framework.

In brief, for given loading protocols the data is first thinned to 25 data points per protocol and, if necessary, the invariant values are pre-calculated for each data point. Then, N_{pop} combinations of random parameter values within are initialized. The stress values corresponding to the N_{pop} parameter sets are calculated using the constitutive model (Eq. (6.6-6.7)) and compared to the experimental data to calculate the residual r:

$$r^2 = \frac{1}{N_{\text{data}}} \sum_{i=1}^{N_{\text{data}}} (S_{11}^{\text{experimental}} - S_{11}^{\text{prediction}})^2 + (S_{22}^{\text{experimental}} - S_{22}^{\text{prediction}})^2 . \tag{6.8}$$

Depending on if the residual value has converged, the parameter sets will either be modified using our in-house differential evolution algorithm or the parameter set with the lowest residual will be declared as the optimal parameter set. More details for the DEO algorithm are presented in the next sub-section. Following successful convergence of the framework to the minimum residual value, the optimal parameters are used to predict the other loading protocols that were not used in the optimization (training).

6.2 Differential Evolution Algorithm

Evolution-based optimization algorithms have become common in soft tissue constitutive modeling due to their relatively quick convergence time and ability to not be trapped in a local minimum. Recent works have often utilized the genetic algorithm method of evolution-based optimization [37, 70, 83, 148]. However, in the evolution algorithm community, differential evolution algorithms have quickly become of great interest due to their ease of implementation, large number of variants, and relatively quick convergence compared to other methods (see the extensive review by Neri *et al.* (2010) [101]). The fundamental concept of DEO is described in three parts: (i) mutation, (ii) crossover, and (iii) selection. Each of these three components are designed to mimic one aspect of evolution. Mutation will take one "parent" parameter set and one or more other random parameter sets and create a linear combination of the parameter values, resulting in the "mutant" set. Cross-over then creates the "child" parameter set that is a random combination of the mutated set and the parent set. Then, the residual value of the child set is compared with the parent set. If the child set has a better residual, it replaces the parent set, otherwise the parent set remains, and the child set is discarded. A plethora of variations using this three-step method exist, including methods with self-adapting parameters for the mutation and crossover [107], different mutation methods [16, 153], and a two-step searching approach [151]. Each method has its advantages and disadvantages depending on the type of problem that is being optimized (i.e., unimodal, multi-modal, or hybrid functions). For our application, we have selected to utilize the two-step approach proposed

by Yu *et al.* (2014) [150]. In this method, the typical DEO algorithm is used as outlined above, and the current state of the optimization is assessed to determine if it is explorative (covering a large range of residual values) or exploitative (approaching the global minimum with a low range of residual values). The corresponding DEO parameters are then adjusted accordingly. Selection of the model proposed by Yu *et al.* was primarily due to the long valley of similar residual values that has been revealed in a previous study by Aggarwal [2]. Hence, the two-step approach can be explorative to find the long valley and then exploitative to find the global minimum within the valley.

Figure 6-2 provides a schematic of the two-step DEO algorithm highlighting key features. First, the residual corresponding to each parameter set is calculated. Then, the parameter sets are sorted two separate times based on: (i) the residual value, (ii) the Euclidian distance of the parameter set to the current parameter set with the lowest residual value. The rank of each parameter set in both sorting scenarios is then used to calculate the *index of state* (IOS), which is defined as

$$IOS = \sum_{i=1}^{N_{pop}} \left| rank_{\text{residual,i}} - rank_{\text{distance,i}} \right|. \tag{6.9}$$

The IOS is then normalized based on the maximum IOS, and a random number between 0 and 1 is generated. If this random number is less than the IOS, the optimization is in an explorative state while if the number is greater than the IOS, the optimization is in an exploitative state. Based on the current state of the optimization, the DEO parameters are modified to either expand the searching capabilities (explorative) or restrict the searching capabilities (exploitative) within the search space.

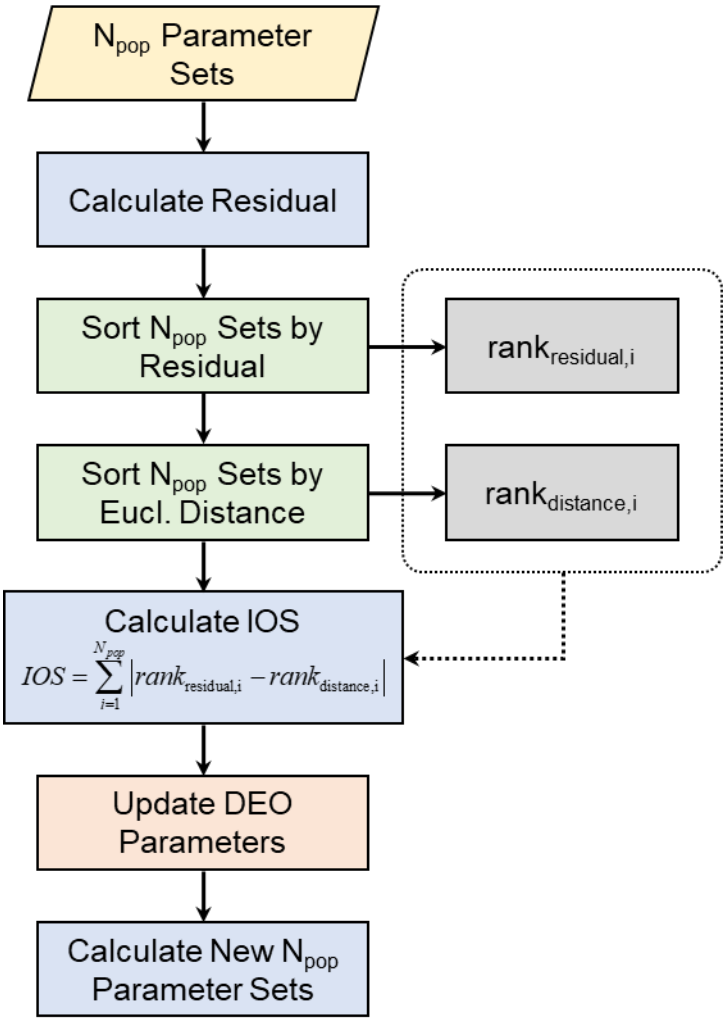

Figure 6-2: Schematic of the two-step differential evolution optimization algorithm. Image was adopted from [151].

As a result of this two-step method, the framework will search more of the parameter space while the points are spread out or it will search closer to the parameters when the points are closer to the global minimum. The DEO algorithm will iterate until the residual is below $5x10^{-7}$, or the difference between the maximum and minimum residual values is less than $1x10^{-7}$.

6.3 Model Fitting Results

Two different SEDFs were investigated to model experimental data obtained in our lab for the three TV leaflets and demonstrate the efficacy of the developed framework. The first SEDF tested was the invariant-based SEDF proposed by Lee *et al.* (2014) [83]

$$W = C_{10}\left(I_1 - 3\right) + \frac{c_0}{2}\left\{\delta \exp\left[c_1\left(I_1 - 3\right)^2\right] + \left(1-\delta\right)\exp\left[c_2\left(I_4 - 1\right)^2\right] - 1\right\}. \qquad (6.10)$$

The second was the strain-based (Fung-type) SEDF investigated by Khoiy *et al.* (2018) [67]

$$W = \frac{c}{2}\left(\exp\left\{a_1 E_{CC}^2 + a_2 E_{RR}^2 + 2a_3 E_{CC} E_{RR}\right\} - 1\right). \qquad (6.11)$$

The experimental data used for the fitting purposes was taken from our refined mechanical characterization framework. Whereas the baseline experiments presented in Chapter 5 had five different loading protocols (T_{circ}:T_{rad} = 1:1, 1:0.75, 0.75:1, 1:0.5, 0.5:1), this refined mechanical characterization framework used 13 loading protocols. There were *9 biaxial loading* protocols (T_{circ}:T_{rad} = 1:1, 1:0.8, 0.8:1, 1:0.6, 0.6:1, 1:0.4, 0.4:1, 1:0.2, 0.2:1), *2 constrained uniaxial* protocols (i.e., T_{circ}:T_{rad} = 1:0 and 0:1), and *2 pure shear* protocols where one axis was under tension and the other axis was under compression to keep the area between the attachments constant. Two training scenarios were considered to examine the efficacy of the models to predict the TV leaflet mechanical response. The first scenario used all 9 biaxial testing protocols for training while the second scenario used the pure shear protocols. Following successful training using the DEO framework, the estimated model parameters were used to predict the tissue's mechanical response under the other protocols not used in the training.

6.3.1 Strain Energy Density Form Proposed by Lee *et al.*

The predictions of the experimental data using the model proposed by Lee *et al.* with the estimated parameters obtained using the biaxial protocols for training are provided in Figure 6-3. Training of the model resulted in excellent fits for all of the biaxial testing protocols with R^2 values ranging from 0.95-0.96. However, the model cannot adequately capture the TV leaflets' mechanical response under the constrained uniaxial (R^2=0.28-0.37) and pure shear protocols ($R^2 \ll 1$). The model appears to under-predict the leaflet stresses when it is under tension and over-predict the leaflet stress while it is in compression during the pure shear loading. The predictions for the second scenario (using the pure shear protocols for training) are provided in Figure 6-4. The most notable finding from this scenario is that the invariant-based model from Lee *et al.* cannot fit the pure shear loading on its own (R^2=0.69-0.89), especially for the TVPL and TVSL leaflet where there is some unrealistic deformation. Additionally, the predictions of the other protocols barely resemble the experimental data. These interesting results suggests the Lee *et al.* SEDF may not accurately capture the leaflets' mechanical response, especially considering uniaxial or pure shear loading. This may stem from the invariants used in the SEDF, and this point is further discussed in Section 6.4.

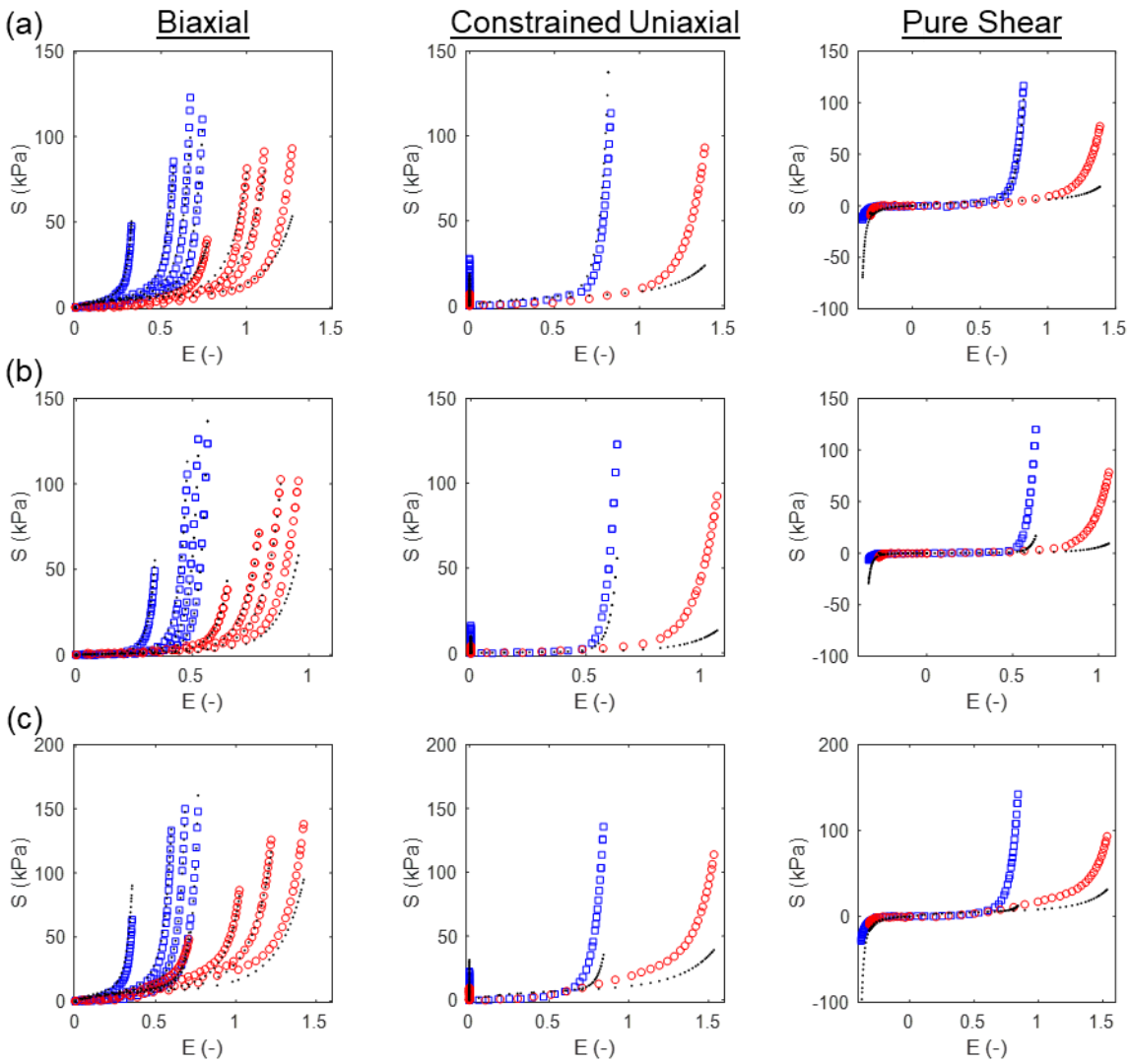

Figure 6-3: Predictions (dots) of the experimental data (shapes) using the Lee *et al.* model for the (a) TVAL, (b) TVPL, and (c) TVSL tissues using model parameters obtained from the training with *all biaxial mechanical data*.

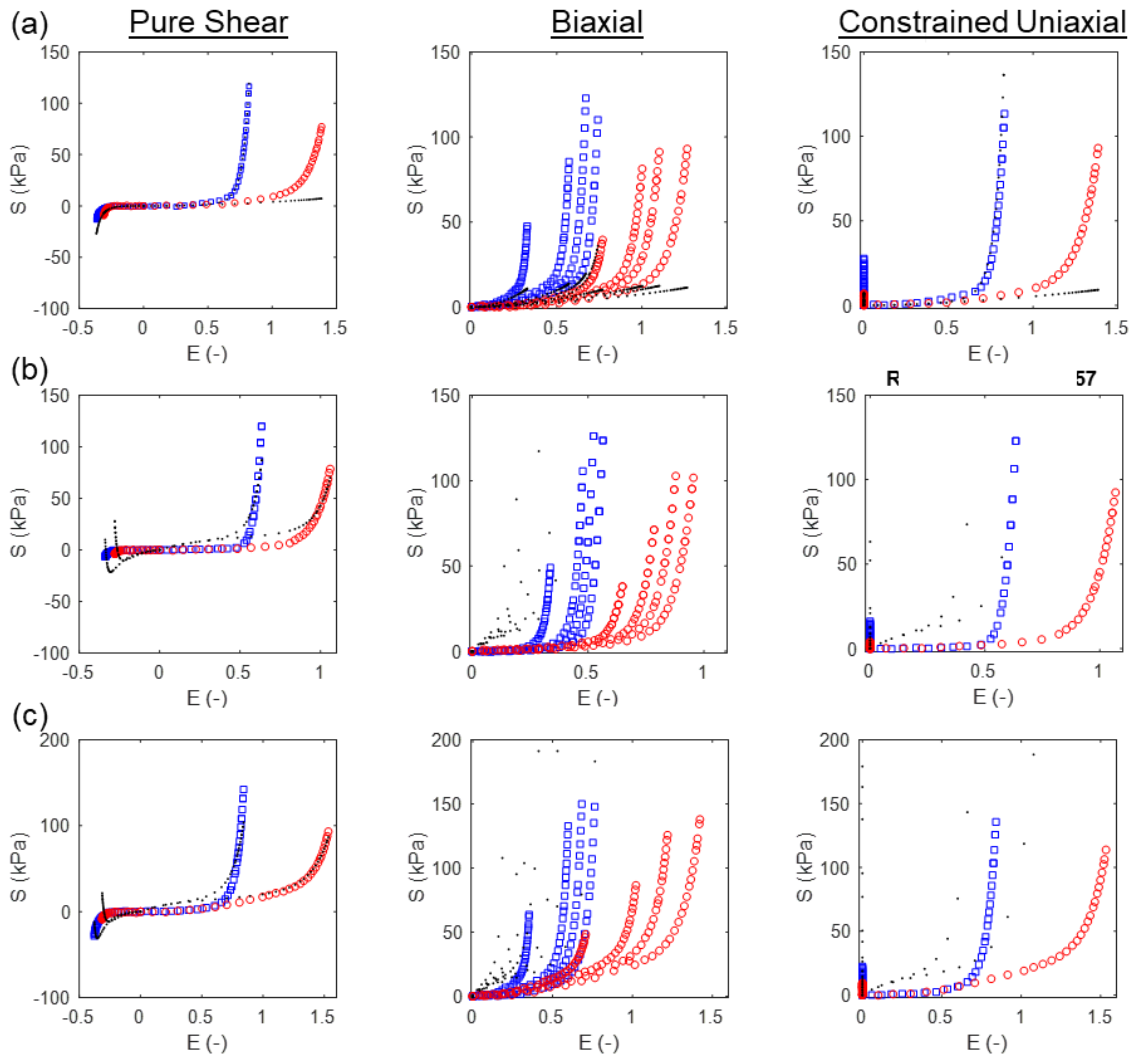

Figure 6-4: Predictions (dots) of the experimental data (shapes) using the Lee *et al.* model for the (a) TVAL, (b) TVPL, and (c) TVSL tissues using model parameters obtained from the training with *only the pure shear data*.

6.3.2 Fung-Type Strain Energy Density Form

The predictions of the experimental data using the Fung-type model with the estimated optimal parameters using the biaxial protocols for training are provided in Figure 6-5. The training using the Fung-type model was slightly less-accurate (R^2=0.93-0.97) than the

training using the Lee *et al.* model. Similar to the Lee *et al.* model, the Fung-type model cannot capture the pure shear loading, but it appears to better predict the constrained uniaxial deformations (R^2=0.49-0.77). It is also interesting to note that the Fung-type model appears to over-estimate the stresses in the pure shear protocol whereas the Lee *et al.* model consistently under-estimated the stresses.

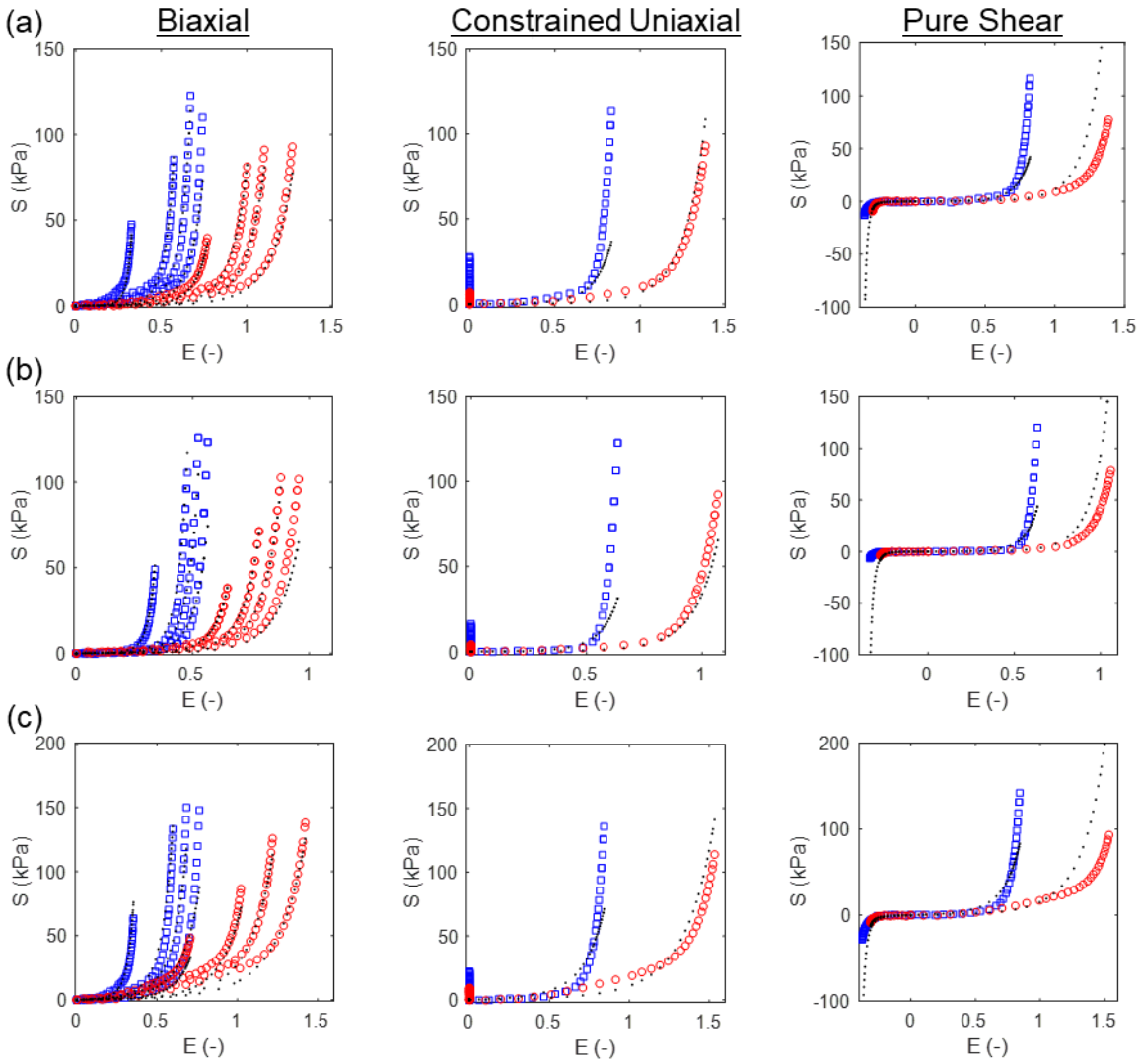

Figure 6-5: Predictions (dots) of the experimental data (shapes) using the Fung-type model for the (a) TVAL, (b) TVPL, and (c) TVSL considering model parameters obtained from the training with *all the biaxial loading protocols*.

The predictions of the experimental data in scenario 2 (using pure shear experimental data for training) are provided in Figure 6-6. The Fung-type model appears to be more suitable for fitting the pure shear data despite some discrepancy with the tissue being under tension where it should be in compression.

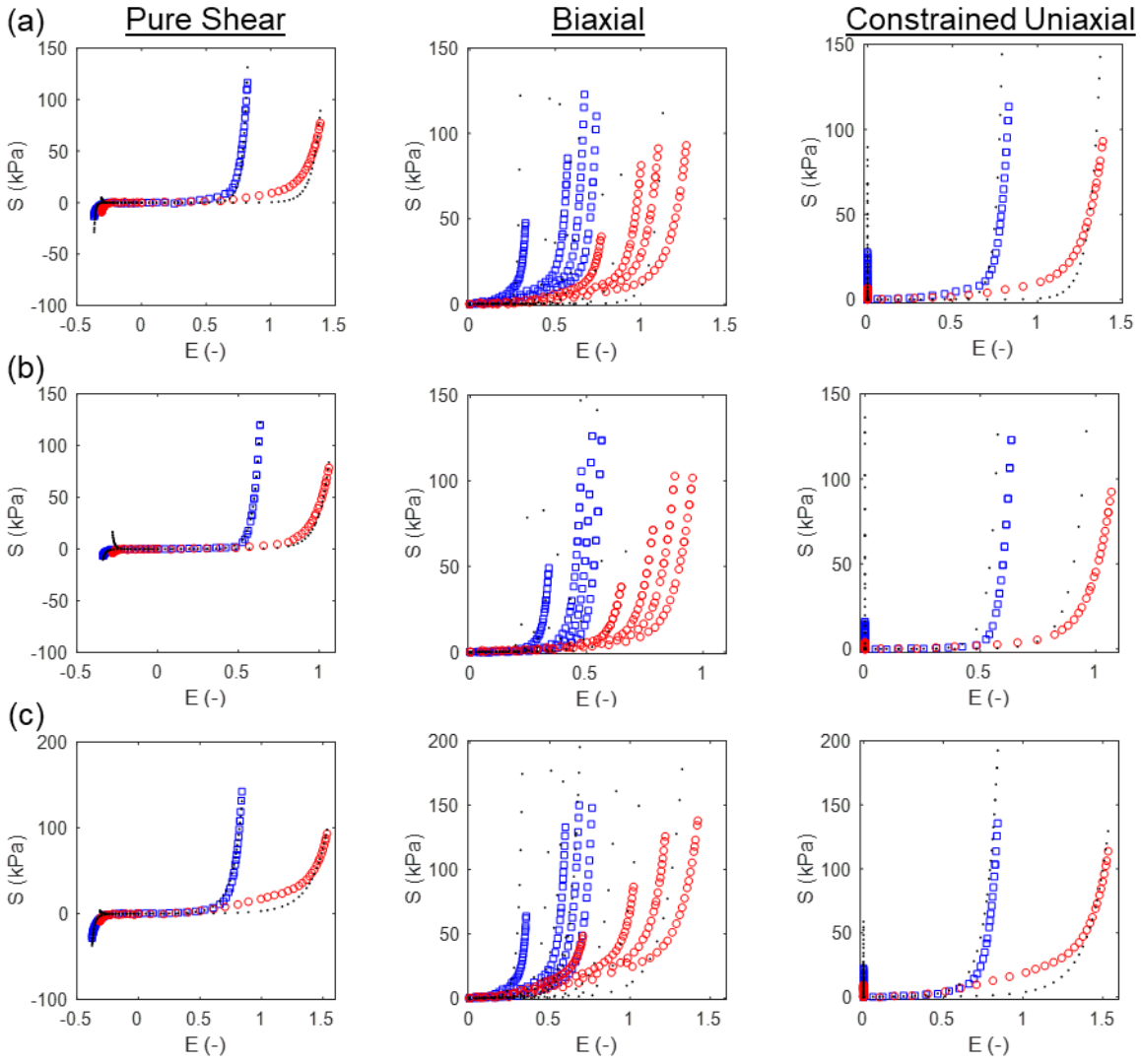

Figure 6-6: Predictions (dots) of the experimental data (shapes) using the Fung-type model for the (a) TVAL, (b) TVPL, and (c) TVSL considering model parameters obtained from the training with *only the pure shear loading protocols*.

Model predictions for the biaxial loading and constrained uniaxial are still very poor with

a significant over-estimate of the stress. This observation suggests that, alongside the Lee *et al.* model, the Fung-type model may not be able to accurately predict the TV leaflet mechanical response under all loading conditions.

6.4 Discussion

The constitutive modeling framework presented in this chapter presents a new avenue for using the experimental data acquired in our laboratory for application in computational modeling. It was constructed in a robust manner to easily allow for investigations considering different SEDF's and different protocols for training. Within the scope of this Thesis we specifically estimated the optimal material parameters for two common SEDF for the three TV leaflets using our extensive biaxial mechanical data. These optimal parameters were then used to predict the TV leaflets' mechanical response under constrained uniaxial and pure shear loading. The results from these preliminary studies held two primary observations: (i) each of the three TV leaflets required unique SEDF parameters to predict the function, and (ii) the optimal material parameters determined from "training" the SEDF with the biaxial loading protocols could not capture the constrained uniaxial and pure shear mechanical response. One rationale for the model not being able to adequately capture the pure shear loading protocol is the lack of terms that can account for the compression of the tissue. For example, the Lee *et al.* model uses the first invariant I_1 and the fourth invariant I_4 to describe the kinematic state of the tissue. It is uncommon for $I_1<1$ during the pure shear simply because the compressive deformation is smaller than the tensile deformation. Additionally, it is assumed $I_4>1$ based on the idea that the individual fibers within the tissue cannot withstand a compressive load. However,

it is known that the families of these fibers are able to withstand compressive forces with the collagen in the fibrosa found in a naturally-compressed state [145]. These two points may indicate why the invariant-based model proposed in Lee *et al.* cannot capture the pure shear loading despite capturing the tensile biaxial mechanical loading well. On the other hand, for the Fung-type model there is a mixed term in the exponent ($a_3E_{11}E_{22}$) that allows for the consideration of the compressive loading. This might explain why the Fung-type can predict the constrained uniaxial and pure shear loading better, but nevertheless it cannot predict them accurately. These two key findings highlight the need for a new SEDF that is formulated such that it can accurately capture the various potential loading scenarios. There are various microstructure-informed constitutive models that may serve as excellent candidates for this need, but they are computationally expensive compared to the phenomenological SEDFs. Once such a phenomenological SEDF has been formulated, the leaflet-specific parameters must be estimated for subsequent use in computational modeling.

CHAPTER 7 Conclusions and Future Work

7.1 Conclusions

The results presented in this thesis aim to enhance the current understanding of the TV biomechanical function. A FE-based computational model of the TV was developed to compare healthy and pathological TV function. Then, to fill many existing gaps in the understanding and computational modeling of the TV biomechanical function, an extensive biaxial mechanical testing study, which are *the first of its kind*, was conducting for characterizations of the TV leaflet tissues. Next, a constitutive modeling framework was developed that utilizes a DEO algorithm to estimate the constitutive model parameters as fitting to the acquired biaxial mechanical testing data. The research developments and key observations are summarized below.

7.1.1 Finite Element Computational Model of the Tricuspid Valve

A FE-based computational model was developed for the TV with geometry based on cubic B-spline and surface representations of porcine TV leaflets and ovine annulus, together with a parametric representation of the chordae tendineae. A nonlinear, isotropic hyperelastic material model was adopted to model the mechanical responses of the TV leaflets. For the chordae tendineae, an elastic, nonlinear material model (with an elastic modulus of 40 MPa and a Poisson's ratio of 0.3) was used. This framework was initially used to simulate the healthy geometry by applying a pressure traction to the ventricular

side of the leaflets corresponding to a TVP of 25 mmHg, while fixing the TV annulus and PM tips. The FE computational model was able to successfully model the complex closure of the TV leaflets and provide realistic leaflet belly stresses (~125 kPa) that agree with previously estimated *in vivo* values based on the Laplace's law for a spherical surface.

7.1.2 Numerical Investigations of the Pathological Tricuspid Valve Via *In Silico* Modeling

The FE-based computational model highlighted in Section 7.1.1 was utilized to simulate various pathological scenarios associated with FTR, which include: (i) PH, (ii) AD, (iii) PM displacement, (iv) flattening of the TV annulus, and (v) chordae tendineae rupture. Simulation results revealed that through an increase in TA/height and decrease in CH, AD and PM displacement directly contribute to the formation of TV regurgitation, while PH does not. However, PH does increase the leaflet stress by ~65% of the original value, which indicates that it may result in adverse remodeling of the surrounding myocardium tissue. As for the chordae tendineae rupture scenario, it was observed that, when ruptured, chordae tendineae attached to the septal or anterior leaflets had the greatest potential for TV leaflet prolapse.

7.1.3 Biaxial Mechanical Characterizations of Tricuspid Valve Leaflets

Six things were investigated using our biaxial mechanical characterization protocol: (i) TV leaflets' biaxial mechanical response, (ii) loading-rate and temperature effects on TV leaflets' tissue mechanical properties, (iii) influence of species and aging on the TV leaflets' mechanical response, (iv) spatial variations of the TV leaflet's tissue mechanical

properties, (v) contribution of the GAGs to the TV leaflets' mechanical responses. Briefly, the results from these studies suggested that the TV leaflets (i) were more extensible than the MV leaflets, (ii) slightly stiffened with increased loading rate, (iii) had a complex response to increasing temperature, (iv) stiffened with aging, (v) had regionally-varying mechanical response, and (vi) were more compliant after removal of GAGs. Results from these characterizations can be used to determine optimal constitutive model parameters or for refining computational models to consider the regional heterogeneities and structural contributions.

7.1.4 Constitutive Modeling Framework

A constitutive modeling framework was developed to allow for investigations determining optimal constitutive model parameters for the acquired experimental data. The development of this type of framework is not novel, but the developed framework can be used for future developments within our laboratory. Preliminary investigations were performed using two common SEDFs to model extensive biaxial mechanical data acquired for the three TV leaflets. These preliminary investigations demonstrated that the efficacy of the model to predict the tissue deformations depended largely on the protocols selected for training the model. Furthermore, it was shown that the invariant-based model was unable to capture the compressive forces present in the pure shear loading while a strain-based model could. This preliminary result suggests that new strain invariants are needed that can account for the compressive forces acting on the tissue. Additionally, investigations are needed to determine the optimal SEDF and material parameters for the atrioventricular heart valve leaflets.

7.2 Recommendations for Future Research

We conclude this thesis by recommending the following topics for future research studies:

(1) *Determination of a leaflet-specific SEDF and model parameters*

Chapter 5 highlighted that each TV leaflet has a unique, anisotropic, nonlinear mechanical response to loading. Additionally, Chapter 6 illustrated that current common SEDFs are not be adequate to capture the TV leaflet's mechanical responses under various loading conditions. Therefore, a SEDF that can accurately capture the TV leaflet's mechanical response to various loading conditions (especially compressive loading) needs to be developed. Once an appropriate SEDF has been determined, the optimal model parameters must be estimated using a similar approach outlined in Chapter 6. Subsequently, the refined SEDF and parameters can be implemented into a computational modeling framework to more accurately predict the TV dynamic closure.

(2) *Refinement of the finite element-based computational model*

The FE-based computational framework presented in Chapter 3 and Chapter 4 had three prominent limitations hindering it from being applicable on a patient-specific case: (i) the use of a fixed annulus and pinned PM tips, (ii) the use of porcine TV leaflet geometry and a parametric representation for the chordae, and (iii) the use of a linearly-increasing pressure traction. The first two limitations necessitate formulation of a new image segmentation pipeline that produces accurate, timely segmented geometry determined from clinical imaging data. Once developed, this

framework can provide patient-specific annulus and PM tip dynamic displacements throughout systole. Additionally, the patient-specific leaflet geometry can be discretized into an FE-suitable mesh for use in the computational framework rather than the porcine geometry. The third limitation requires the implementation of the physiological time-dependent transvalvular pressure into the FE simulation. Refinements of the model to consider these patient-specific conditions will open the door for (i) helping with timely clinical intervention and (ii) considering more complex congenital defects such as Tetralogy of Fallot.

(3) *Enhancement of the FE model to consider the right ventricle*

Many TV diseases or pathologies also affect the right ventricle function and anatomy. Therefore, the right ventricle should be considered and implemented into the FE model to quantify how the pathologies described in Chapter 4 affect the right ventricle function. Insight from these pathological simulations can enhance the current understanding of right ventricular failure that may arise from TV regurgitation. Additionally, once the right ventricle has been implemented, realistic fluid-structure interaction simulations can be formulated and performed. Accurate fluid-structure interaction simulations can provide more enhanced information about the TV regurgitation through providing a quantitative value for the regurgitant blood flow. This extension is another avenue for translational impact in the clinical setting of the presented FE model studies.

(4) *Mechanical characterizations of the AHVs considering other scenarios*

The results presented in Chapter 5 are an excellent first step towards understanding the complex biaxial mechanical response of the heart valve leaflets, but much is still unknown. For instance, the TV leaflets are known to have a distinct four-layered structure with each layer having a unique microstructural make-up, but there are no studies discussing the contribution of each distinct layer to the TV leaflets' mechanical response. Furthermore, studies are warranted to investigate the contribution of the microstructural constituents besides the GAGs (e.g., the collagen fibers, elastin fibers or VICs) to the TV leaflet's mechanical properties. The data from these experiments could then be implemented into the constitutive modeling framework presented in Chapter 6 to determine scenario-specific constitutive model parameters.

APPENDIX A Nomenclature

Table A-1: Description of the abbreviations used throughout the Thesis.

Group	Abbreviation	Description
Anatomy	AV	Aortic Valve
	CH_{AP}	Commissure Height Anterior-Posterior
	CH_{AS}	Commissure Height Anterior-Septal
	CH_{PS}	Commissure Height Posterior-Septal
	LH_{A}	Leaflet Height Anterior Leaflet
	LH_{P}	Leaflet Height Posterior Leaflet
	LH_{S}	Leaflet Height Septal Leaflet
	MV	Mitral Valve
	PM	Papillary Muscle
	PM-AP	Papillary Muscle Anterior-Posterior
	PM-AS	Papillary Muscle Anterior-Septal
	PM-PS	Papillary Muscle Posterior-Septal
	RA	Right Atrium
	RV	Right Ventricle
	TV	Tricuspid Valve
	TVAL	Tricuspid Valve Anterior Leaflet
	TVP	Transvalvular Pressure
	TVPL	Tricuspid Valve Posterior Leaflet
	TVSL	Tricuspid Valve Septal Leaflet
Clinically-Relevant Values	CH	Coaptation Height
	CVAP	Cut View Anterior-Posterior
	CVAS	Cut View Anterior-Septal
	CVPS	Cut View Posterior-Septal
	TA	Tenting Area

	TH	Tenting Height
Constitutive Modeling	**C**	Right Cauchy-Green Deformation Tensor
	δ	Degree of Anisotropy (Lee *et al.* [83])
	DEO	Differential Evolution Optimization
	E	Green-Lagrange Strain Tensor
	E_f	Fiber Ensemble Strain
	F	Deformation Gradient
	Γ	Fiber Orientation Distribution Function
	HGO	Holzapfel, Gasser, and Ogden
	I	Identity Tensor
	I_1	First Invariant of **C**
	I_4	Fourth Invariant of **C**
	IOS	Index of State
	κ	Fiber distribution about preferred angle
	N	Preferred Fiber Orientation
	N_{pop}	Number of parameter sets in population
	P	First-Piola Kirchoff Stress Tensor
	S	Second-Piola Kirchoff Stress Tensor
	SEDF	Strain Energy Density Function
	S_f	Ensemble Fiber Stress
	W	Strain Energy Density
Disease/Pathology	AD	Annulus Dilation
	FTR	Functional Tricuspid Regurgitation
	PH	Pulmonary Hypertension
	TR	Tricuspid Regurgitation
Imaging Modalities	2DTTE	Two-Dimensional Transthoracic Echocardiography
	CT	Computed Tomography
	MRI	Magnetic Resonance Imaging
	TEE	Transesophageal Echocardiography

	TTE	Transthoracic Echocardiography
	μCT	Micro-Computed Tomography
Mechanical Testing	circ	Circumferential Direction
	L	Specimen Edge Length
	λ	Tissue Stretch
	λ^{1-peak}	Mechanical Stretch
	λ^{0-peak}	Peak Stretch
	λ^{0-1}	Preconditioning Stretch
	rad	Radial
	t	Specimen thickness
	T_{circ}	Membrane Tension in the Circumferential Direction
	$T_{circ,max}$	Maximum Membrane Tension in the Circumferential Direction
	T_{rad}	Membrane Tension in the Radial Direction
	$T_{rad,max}$	Maximum Membrane Tension in the Radial Direction
Mechanics	FE	Finite Element
	FSI	Fluid-Structure Interaction
Microstructure	A	Atrialis
	F	Fibrosa
	GAG	Glycosaminoglycans
	S	Spongiosa
	V	Ventricularis
	VIC	Valvular Interstitial Cell
Other	2D	Two-Dimensional
	3D	Three-Dimensional
	ANOVA	Analysis of Variance
	CCD	Charge-Coupled Device

	DIC	Digital Image Correlation
	PBS	Phosphate-Buffered Saline
	SEM	Standard Error of the Mean
	USDA	United States Department of Agriculture

APPENDIX B ABAQUS Input File Description

This appendix describes the ABAQUS input files used for the finite element simulations presented in Chapter 3 and Chapter 4. First, the entire input file is presented and then detailed information about each section of code is provided.

```
*Heading
** Job name: TV_Mesh_4 Model name: Model-1
** Generated by: Abaqus/CAE 6.12-1
**
*Include, input=Model_6_node_scaled_085.inp
*Include, input=Model_6_ele_leaflet_scaled_085.inp
*Include, input=Model_6_ele_chord_scaled_085.inp
**
**
*SHELL SECTION, ELSET=PROP_TVAL, MATERIAL=MAT_TVAL,
section integration = GAUSS
0.52, 5
*Transverse Shear
40., 40., 0.
**
*SHELL SECTION, ELSET=PROP_TVPL, MATERIAL=MAT_TVPL,
section integration = GAUSS
0.46, 5
*Transverse Shear
40., 40., 0.
**
*SHELL SECTION, ELSET=PROP_TVSL, MATERIAL=MAT_TVSL,
section integration = GAUSS
0.37, 5
*Transverse Shear
40., 40., 0.
**
*SOLID SECTION, ELSET=PROP_CHORD, MATERIAL=MAT_CHORD
0.171
```

```
*Nset, nset=Set-1
   1,   2,   5,   6,   7,   8,   9,  10,  11,  12,  13,  14,  15,  16,  17,  18
  19,  20,  21,  22,  23,  24,  25,  26,  27,  28,  29,  30,  31,  32,  33,  34
  35,  36,  37,  38,  39,  40,  41,  42,  43,  44,  45,  46,  47,  48,  49,  50
  51,  52,  53,  54,  55,  56,  57,  58,  59,  60,  61,  62,  63,  64,  65,  66
  67,  68,  69,  70,  71,  72,  73,  74,  75,  76,  77,  78,  79,  80,  81,  82
  83,  84,  85,  86,  87,  88,  89,  90,  91,  92,  93,  94,  95,  96,  97,  98
  99, 100, 101, 102, 103, 104, 105, 106, 107, 108, 109, 110, 111, 112, 113, 114
 115, 116, 117, 118, 119, 120, 121, 122, 123, 124, 125, 126, 127, 128, 129, 130
 131, 132, 133, 134, 135, 136, 137, 138, 139, 140, 141, 142, 143, 144, 145, 146
 147, 148, 149, 353, 354, 355, 356, 357, 358, 359, 360, 361, 362, 363, 364, 365
 366, 367, 368, 369, 370, 371, 372, 373, 374, 375, 376, 377, 378, 379, 380, 381
 382, 383, 384, 385, 386, 387, 388, 389, 390, 391, 392, 393, 394, 395, 396, 397
 398, 399, 400, 401, 402, 403, 404, 405, 406, 407, 408, 409, 410, 411, 412, 413
 414, 415, 416, 417, 418, 419, 420, 421, 422, 423, 424, 425, 426, 427, 428, 429
 430, 431, 432, 433, 434, 435, 436, 437, 438, 439, 440, 441, 442, 443, 444, 445
 446, 447, 448, 449, 450, 451, 452, 453, 454, 455, 456, 457, 458, 459, 460, 461
 462, 463, 464, 465, 466, 467, 468, 469, 470, 471, 472, 473, 474, 475, 476, 477
 478, 479, 480, 481, 482, 483, 484, 485, 486, 487, 488, 489, 490, 491, 492, 493
 494, 495, 496, 497, 498, 499, 500
*Nset, nset=Set-2
   10001, 10066, 10135
**
**
*Elset, elset=_Surf-1_SNEG, generate
    1,  8850,     1
*Surface, type=ELEMENT, name=Surf-1
_Surf-1_SNEG, SNEG
*Elset, elset=_Surf-2_SPOS, generate
    1,  8850,     1
*Surface, type=ELEMENT, name=Surf-2, MAX RATIO=1.0
_Surf-2_SPOS, SPOS
**
*Amplitude, name=Amp-1, definition=SMOOTH STEP
                0.,    0., 0.4,    25.
```

```
** MATERIALS **
*Material, name=MAT_TVAL
*Density
1.100e-9
*User Material, constants=6
 0.01,  0.000209,     9.046,   16.4511,  -12.8814,  0.8438
*DEPVAR
 10
*Material, name=MAT_TVPL
*Density
1.100e-9
*User Material, constants=6
 0.01,  0.000209,     9.046,   16.4511,  -12.8814,  0.8438
*DEPVAR
 10
*Material, name=MAT_TVSL
*Density
1.100e-9
*User Material, constants=6
 0.01,  0.000209,     9.046,   16.4511,  -12.8814,  0.8438
*DEPVAR
 10
*Material, name=MAT_CHORD
*Density
1.100e-9
*Elastic
40, 0.3
***
```

```
*Surface Interaction, name=IntProp-1
1.0
*Friction
0.,
*Surface Behavior, pressure-overclosure=linear
0.5
**
*Contact
*Contact Inclusions
Surf-1 ,
Surf-2 ,
Surf-1 , Surf-2
*Contact Property Assignment
 ,  , IntProp-1
** BOUNDARY CONDITIONS
**
*Boundary
Set-1, 1, 1
Set-1, 2, 2
Set-1, 3, 3
Set-1, 4, 4
Set-1, 5, 5
Set-1, 6, 6
Set-2, PINNED
```

```
*Step, name=Step-1, nlgeom=YES
*Dynamic, explicit
, 0.400
**
** INTERACTION PROPERTIES
**
**
*Variable mass scaling, freq=1, dt=1.25e-006, type = below min
**
**
*Dsload, amplitude=Amp-1
Surf-1, P,      0.0001333224
*Dsload
Surf-1, VP,    -0.000005
**
**
*Output, field, NUMBER INTERVAL=50
*Node Output
U, COORD, RF
*Element Output
S, MISESMAX, E, LE
*End Step
```

1) (Lines 5-7): The input files that describe the model nodes and elements are included.

```
*Include, input=Model_6_node_scaled_085.inp
*Include, input=Model_6_ele_leaflet_scaled_085.inp
*Include, input=Model_6_ele_chord_scaled_085.inp
```

1.1) "Model_6_node_scaled_085.inp" contains the coordinates for each node.

1.2) "Model_6_ele_leaflet_scaled_085.inp" contains the element connectivity (Type=S4) for the leaflets.

1.3) "Model_6_ele_chord_scaled_085.inp" contains the element connectivity

(Type=T3D2) for the chordae.

2) (Lines 10-29): The four sections of the model (TVAL, TVPL, TVSL, and chordae) are defined based on the element set (ELSET) defined in bullet item 1 and the material (MATERIAL) that is defined later in the .inp file. Additionally, the thickness values (in mm) are defined for each section (e.g., 0.52 for TVAL shown below).

```
10 *SHELL SECTION, ELSET=PROP_TVAL, MATERIAL=MAT_TVAL,
11 section integration = GAUSS
12 0.52, 5
13 *Transverse Shear
14 40., 40., 0.
```

3) (Lines 32-51) A node set (Nset) is created including all of the annulus nodes.

```
32 *Nset, nset=Set-1
33    1,   2,   5,   6,   7,   8,   9,  10,  11,  12,  13,  14,  15,  16,  17,  18
34   19,  20,  21,  22,  23,  24,  25,  26,  27,  28,  29,  30,  31,  32,  33,  34
35   35,  36,  37,  38,  39,  40,  41,  42,  43,  44,  45,  46,  47,  48,  49,  50
36   51,  52,  53,  54,  55,  56,  57,  58,  59,  60,  61,  62,  63,  64,  65,  66
37   67,  68,  69,  70,  71,  72,  73,  74,  75,  76,  77,  78,  79,  80,  81,  82
38   83,  84,  85,  86,  87,  88,  89,  90,  91,  92,  93,  94,  95,  96,  97,  98
39   99, 100, 101, 102, 103, 104, 105, 106, 107, 108, 109, 110, 111, 112, 113, 114
40  115, 116, 117, 118, 119, 120, 121, 122, 123, 124, 125, 126, 127, 128, 129, 130
41  131, 132, 133, 134, 135, 136, 137, 138, 139, 140, 141, 142, 143, 144, 145, 146
42  147, 148, 149, 353, 354, 355, 356, 357, 358, 359, 360, 361, 362, 363, 364, 365
43  366, 367, 368, 369, 370, 371, 372, 373, 374, 375, 376, 377, 378, 379, 380, 381
44  382, 383, 384, 385, 386, 387, 388, 389, 390, 391, 392, 393, 394, 395, 396, 397
45  398, 399, 400, 401, 402, 403, 404, 405, 406, 407, 408, 409, 410, 411, 412, 413
46  414, 415, 416, 417, 418, 419, 420, 421, 422, 423, 424, 425, 426, 427, 428, 429
47  430, 431, 432, 433, 434, 435, 436, 437, 438, 439, 440, 441, 442, 443, 444, 445
48  446, 447, 448, 449, 450, 451, 452, 453, 454, 455, 456, 457, 458, 459, 460, 461
49  462, 463, 464, 465, 466, 467, 468, 469, 470, 471, 472, 473, 474, 475, 476, 477
50  478, 479, 480, 481, 482, 483, 484, 485, 486, 487, 488, 489, 490, 491, 492, 493
51  494, 495, 496, 497, 498, 499, 500
```

4) (Lines 52-53) A node set (Nset) is created including the papillary muscle nodes.

```
52 *Nset, nset=Set-2
53    10001, 10066, 10135
```

5) (Lines 56-59) An element set and surface are created for the leaflet face with a negative normal vector.

```
56 *Elset, elset=_Surf-1_SNEG, generate
57     1,  8850,     1
58 *Surface, type=ELEMENT, name=Surf-1
59 _Surf-1_SNEG, SNEG
```

6) (Lines 60-63) An element set and surface are created for the leaflet face with a positive normal vector.

```
60 *Elset, elset=_Surf-2_SPOS, generate
61     1,  8850,     1
62 *Surface, type=ELEMENT, name=Surf-2, MAX RATIO=1.0
63 _Surf-2_SPOS, SPOS
```

7) (Lines 65-66) A smooth step amplitude is defined that will go from 0 mmHg to 25 mmHg in 0.40 seconds. This will be used in the later boundary conditions.

```
65 *Amplitude, name=Amp-1, definition=SMOOTH STEP
66              0.,    0., 0.4,    25.
```

8) (Lines 67-88) The material properties for each leaflet are defined (e.g., TVAL shown below). These are used as an input into the ABAQUS user material sub-routine.

```
67 ** MATERIALS **
68 *Material, name=MAT_TVAL
69 *Density
70 1.100e-9
71 *User Material, constants=6
72  0.01,  0.000209,     9.046,   16.4511,  -12.8814,  0.8438
73 *DEPVAR
74  10
```

9) (Lines 89-93) The material properties for the chordae tendineae are defined.

```
89 *Material, name=MAT_CHORD
90 *Density
91 1.100e-9
92 *Elastic
93 40, 0.3
```

10) (Lines 95-100) Surface interaction properties are defined.

```
 95 *Surface Interaction, name=IntProp-1
 96 1.0
 97 *Friction
 98 0.,
 99 *Surface Behavior, pressure-overclosure=linear
100 0.5
```

11) (Lines 102-108) The contact properties between the leaflets are defined.

```
102 *Contact
103 *Contact Inclusions
104 Surf-1 ,
105 Surf-2 ,
106 Surf-1 , Surf-2
107 *Contact Property Assignment
108  ,  , IntProp-1
```

12) (Lines 111-118) The boundary conditions are defined: annulus (Set-1) is fixed and the papillary muscles (Set-2) are pinned.

```
111 *Boundary
112 Set-1, 1, 1
113 Set-1, 2, 2
114 Set-1, 3, 3
115 Set-1, 4, 4
116 Set-1, 5, 5
117 Set-1, 6, 6
118 Set-2, PINNED
```

13) (Lines 121-128) The "Step" for the simulation is initialized and the mass scaling properties are defined.

```
121 *Step, name=Step-1, nlgeom=YES
122 *Dynamic, explicit
123 , 0.400
124 **
125 ** INTERACTION PROPERTIES
126 **
127 **
128 *Variable mass scaling, freq=1, dt=1.25e-006, type = below min
```

14) (Lines 131-134) The loading conditions are defined for the simulation. The value "0.0001333224" is for converting 1.0 mmHg to 1.0 MPa.

```
131 *Dsload, amplitude=Amp-1
132 Surf-1, P,      0.0001333224
133 *Dsload
134 Surf-1, VP,    -0.000005
```

15) (Lines 137-142) The requested simulation outputs and end of the simulation Step are defined.

```
137 *Output, field, NUMBER INTERVAL=50
138 *Node Output
139 U, COORD, RF
140 *Element Output
141 S, MISESMAX, E, LE
142 *End Step
```

APPENDIX C Biaxial Mechanical Testing Procedures

The detailed protocols for performing the biaxial mechanical characterizations of the heart valve leaflets were adapted from our previously-published manuscript [116] and are described below.

1. Tissue Acquisition and Cleaning

1.1) Retrieve the animal hearts on the same day as the animal is slaughtered and store the hearts in an ice chest to ensure the tissue freshness. Transport the hearts to the laboratory space.

1.2) Upon arrival to the lab, submerge the heart in the bucket of phosphate-buffered saline (PBS) solution to rinse off any excess blood. Retrieve forceps, a placemat, a surgical blade, a bucket of PBS solution, bleach and a plastic bag. Prepare the placemat by laying it on the dissection counter, allowing for easier cleanup of blood-related mess. After the heart has been sufficiently rinsed, place the heart on the placemat (Figure C-1a).

1.3) Using the forceps, locate the parting line between the atria and the ventricle on each side of the heart. Using a razor blade, make an incision carefully along this parting line and reveal the heart valves and the ventricles (Figure C-1b). Make the incision along the entire outer circumference of the heart, such that the atria and all heart material superior to the ventricles may be removed.

1.4) With the forceps, carefully pull out any observed blood clots in the ventricles (Figure C-1c). If an attempt is made to remove a blood clot but it does not move, ensure

chordae tendineae or leaflets have not been grabbed. Place blood clots in the biohazard bag for waste disposal.

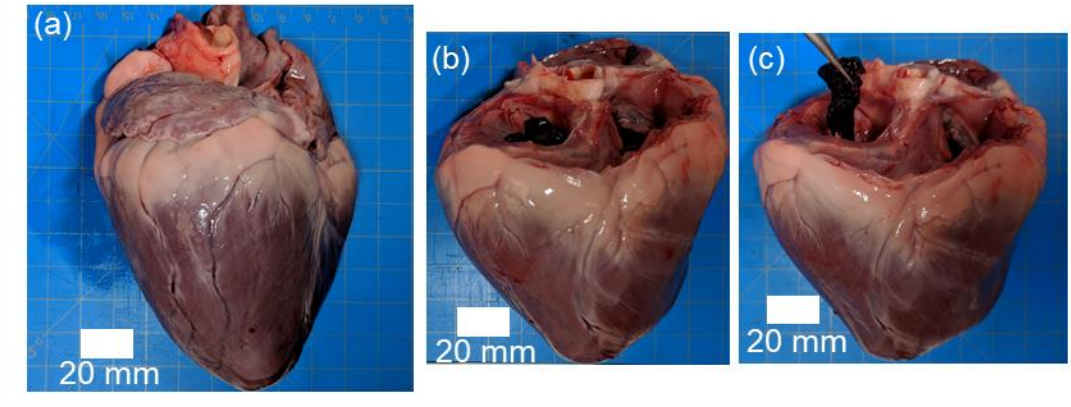

Figure C-1: Experimental photos of porcine hearts retrieved from a local slaughterhouse: (a) whole heart is rinsed of blood with PBS solution; (b) a cut is made between the atria and ventricle to reveal both the mitral and tricuspid valves; and (c) blood clots are then removed from the heart before storage.

1.5) When all blood clots have been removed from the ventricles, rinse the heart one final time in the bucket of PBS solution. Place the clean heart in the plastic bag and store it in a freezer.

1.6) Using a solution of 10% bleach and 90% water, mix the blood with the bleach solution and stir continuously for approximately 10 minutes. Successful bleach treatment is indicated by the solution transitioning from red to yellow. Dispose the bleach-treated blood through drainage.

2. Heart Dissection and Examination of Anatomy

2.1) Retrieve the previously cleansed heart and allow it to thaw in a warm water bath. The required materials for dissection include forceps, surgical blades, placemats,

phosphate-buffered saline, and small storage containers. After the heart is completely thawed, put it on a placemat to absorb remaining blood.

2.2) Hold the heart in the top-down view and identify the tricuspid valve (TV) on the right side of the heart. Locate the commissures and make an incision through one of the commissures and the ventricular wall (Figure C-2b).

2.3) Identify the TV septal, posterior, and anterior leaflets, and perform the leaflet extraction as done in Step 2.4. Place all obtained leaflets in a labeled container filled with PBS solution and store the container in a refrigerator at approximately 4 °C.

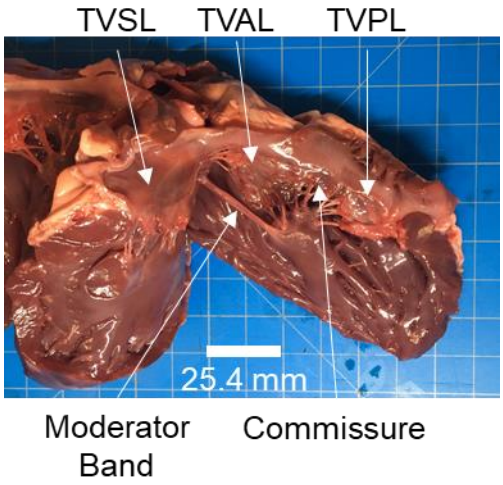

Figure C-2: Experimental photos of the opened porcine heart revealing the tricuspid valve with the anterior leaflet (TVAL), posterior leaflet (TVPL), and septal leaflet (TVSL).

3. Tissue Dissection

3.1) Retrieve the leaflet from the fridge, the tissue cutter for the specified sectioning size, surgical pen, forceps, razor blades, and a cutting mat.

3.2) Using forceps, remove the specimen from the PBS solution and lay it flat on the cutting mat with radial direction (rad) aligned to the *Y*-direction, and the circumferential

direction (circ) aligned to the *X*-direction (Figure C-3a). Identify the leaflet's *central region* as the testing section.

3.3) Align the tissue cutter such that the desired tissue testing region is within the boundaries of the razor blades. Make one cut horizontally and another vertically to form a square region of desired dimension (Figure C-3b). Using the surgical pen, label the tissue's radial direction (Figure C-3b).

3.4) Using the razor blade, trim chordal attachments by stretching the chordae from the leaflet with the forceps and making a careful cut without causing damage to the leaflet.

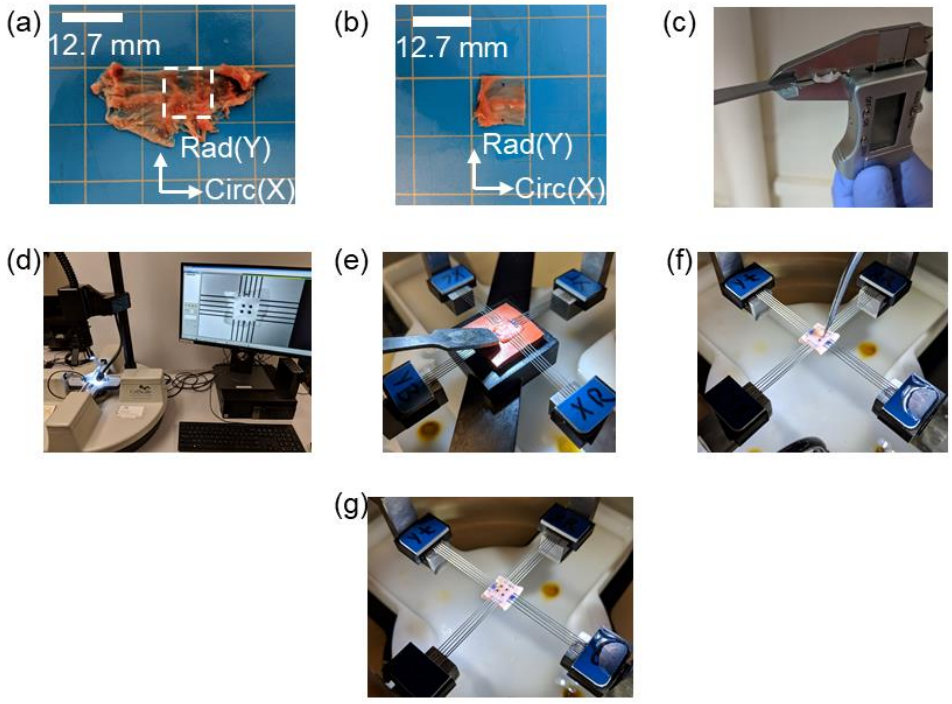

Figure C-3: The (a) bulk leaflet is sectioned into a (b) 10 x 10 mm testing region (radial direction noted by surgical pen markers). (c) The leaflet thickness is measured. Specimens are mounted to (d) the biaxial testing system by (e) piercing the tissue with metal tines. After mounting, (f) fiducial markers are glued onto the surface of the tissue before (g) submersion in PBS solution at 37 °C.

4. Thickness Measurement and Biaxial Tester Setup

4.1) Retrieve the sectioned tissue specimen, digital calipers, and a small metal spatula. Using the digital calipers, measure and record the thickness of the metal spatula.

4.2) Using forceps, lay the tissue specimen flat on the metal spatula. Using the digital calipers measure the thickness of the spatula-tissue pair (Figure C-3c) at 3 different leaflet locations. Subtract the spatula's thickness from the pair and record the average thickness.

4.3) Prepare a PBS bath at 37 °C, which is correspondent to the tissue's physiologic conditions.

5. Tissue Mounting and Fiducial Marker Placement

5.1) Retrieve forceps, tissue specimen, mounting hardware, fine-tipped tool, glass beads (diameters of 300-500 μm), and super glue.

5.2) Mount the tissue to the biaxial testing system (Figure C-3d-e). While mounting, ensure the tissue's circumferential and radial directions are aligned with the machine's *X*- and *Y*-directions.

5.3) For fiducial marker placement, place glass beads into one small open-faced container and a small pool of super glue in another container. Using the fine-tipped tool, coat the tip with a small amount of super glue and stick an individual bead to the tip of the tool.

5.4) Carefully use the tool to transfer the bead to one corner of the middle third of the tissue's testing region (Figure C-3f). Repeat this step until a square array of four beads is formed (Figure C-3g).

6. Preconditioning Step and Duration Timing

6.1) To compute the appropriate membrane tension, obtain the tissue's effective testing edge length and use the equation:

$$\mathbf{T} = diag[T_{Circ}, T_{Rad}] = diag[f_{Circ}, f_{Rad}] / L. \quad \text{(C.1)}$$

Here, $\mathbf{T}$ is the membrane tension tensor in a unit of force/length, f is the force, and L is the specimen's effective testing length.

6.2) Create a preconditioning protocol such that the tissue will undergo 10 loading/unloading cycles at the forces associated with peak membrane tension at a loading rate of 4.42 N/min, including a preload of 2.5% of the maximum force (Figure C-4).

6.2.1) Create a new arbitrary testing directory to temporarily to store the preconditioning data because it is not necessary for future calculations. Establish a loading rate of 4.42 N/min for subsequent testing.

6.2.2) Create a new set of testing parameters and set the name of the protocol as Preconditioning0 (Figure C-4a). For the *X*- and *Y*-axes, set the control mode to be force and the control function to be step. Set the load magnitude as the force associated with targeted peak membrane tension (cf. Step 6.1) (Figure C-4b). Set the preload magnitude as 2.5% of the maximum force for the first repetition only (Figure C-4c). Set the stretch duration and recovery duration to both be 25 seconds. Set the number of repetitions to be 10 (Figure C-4e).

6.3) When the preconditioning step finishes, make a note of the tissue's deformation in the *X*- and *Y*-directions. Prepare a protocol to move the specimen to the maximum force

beginning from the recorded size.

6.3.1) Retrieve a stopwatch for timing purposes. Begin the maximum force loading protocol and start the stopwatch simultaneously when the machine begins actuation (Figure C-5a). Stop the stopwatch when actuation stops. Stopping will be obvious through auditory cues.

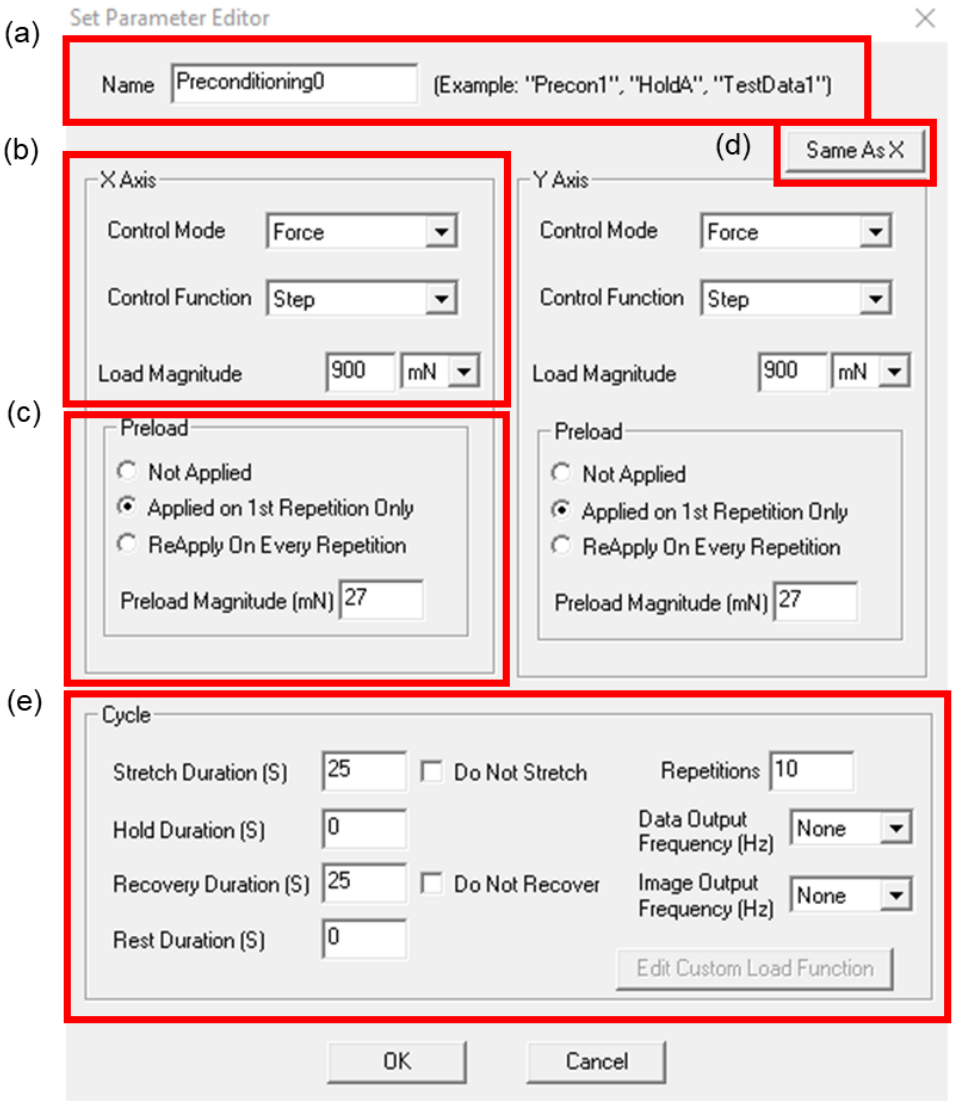

Figure C-4: The preconditioning protocol is created by setting (a) the protocol name, (b) the testing control mode and force in the *X*-axis, (c) the preload conditions, (d) the *Y*-axis parameters to be the same as in the *X*-axis, and (e) the cycle parameters.

6.3.2) Record the post preconditioning peak tissue deformation, alongside the time from the stopwatch representing the tissue's optimal stretch time (Figure C-5b).

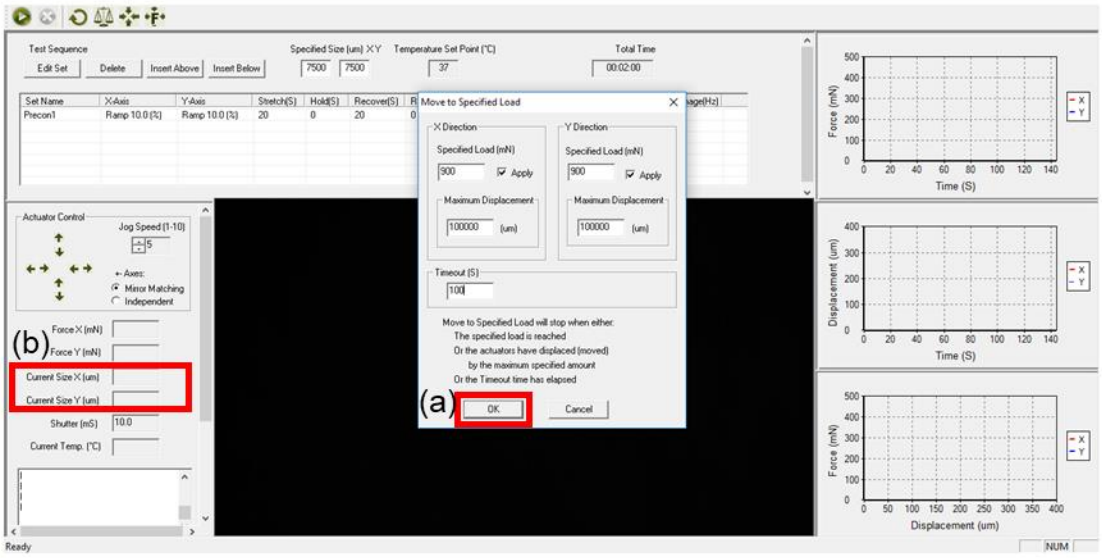

Figure C-5: The timing step requires (a) moving the tissue from the post preconditioning deformation to the peak membrane tension (and corresponding peak deformation) while simultaneously starting a stopwatch to record the stretch time. When the target force has been reached, (b) the post-preconditioning deformation is recorded.

7. Biaxial Mechanical Testing

7.1) Prepare a force-controlled protocol at a loading rate of 4.42 N/min:

7.1.1) Open a new testing directory and name the test. Set the data to save to a known location for use in later stress and strain calculations. Move the specimen back to the original mounting configuration.

7.1.2) Create a protocol set titled "FirstImage". Set the *X*-axis and *Y*-axis control mode to force and the control function to step. Set the load magnitude to 0 mN. Set the stretch duration and recovery duration each to 1 second. Set the number of

repetitions to 1. Set the data output frequency and image output frequency each to 1 Hz

7.1.3) Construct a new testing set named "PreconditioningA". Establish the testing parameters such that the tissue will undergo 10 repetitions of cyclic loading/unloading to the targeted force for desired membrane tension exactly as was prepared in Step 6.2. Note that now, the stretch time and recover time should be the time recorded in Step 6.4. No images are captured in the "A" testing set, but data is captured at 15 Hz.

7.1.4) Construct another testing set named "PreconditioningB". All testing parameters should be identical to as found in the previous step, with the exception that image output frequency is set to 15Hz, and no preload is applied.

7.1.5) After the preconditioning protocol, create testing protocols such that the tissue is loaded to peak membrane tension in the following circumferential-to-radial loading ratios at a loading rate of 4.42 N/min: 1:1, 0.75:1, 1:0.75, 0.5:1, 1:0.5 (Figure C-6). Retrieve data from the last two cycles of each loading ratio for subsequent data processing and analyses described in Step 10. Refer to Table C-1 for a detailed description of the protocols to be established.

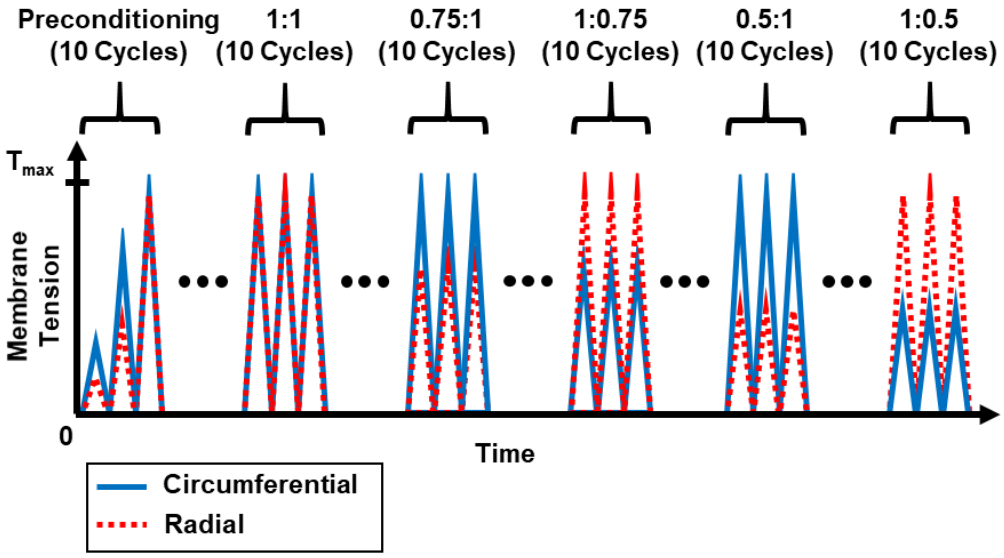

Figure C-6: Schematic of the force-controlled biaxial testing protocols.

Table C-1: Full testing parameters for all protocols of the force-controlled testing scheme.

Set Name	*X*-Axis	*Y*-Axis	Stretch (S)	Hold (S)	Recover (S)	Rest (S)	XPreload (mN)	YPreload (mN)	Reps	Data (Hz)	Image (Hz)
FirstImage	Step 0.0 (mN)	Step 0.0 (mN)	1	0	1	0	0.0 (First)	0.0 (First)	1	1	1
PreconditioningA	Step *F* (mN)	Step *F* (mN)	*t*	0	*t*	0	0.025**F* (First)	0.025**F* (First)	8	15	0
PreconditioningB	Step *F* (mN)	Step *F* (mN)	*t*	0	*t*	0	None	None	2	15	15
1:1A	Step *F* (mN)	Step *F* (mN)	*t*	0	*t*	0	None	None	10	15	0
1:1B	Step *F* (mN)	Step *F* (mN)	*t*	0	*t*	0	None	None	2	15	15
0.75:1A	Step (0.75**F*) (mN)	Step *F* (mN)	*t*	0	*t*	0	None	None	10	15	0
0.75:1B	Step (0.75**F*) (mN)	Step *F* (mN)	*t*	0	*t*	0	None	None	2	15	15
1:0.75A	Step *F* (mN)	Step (0.75**F*) (mN)	*t*	0	*t*	0	None	None	10	15	0
1:0.75B	Step *F* (mN)	Step (0.75**F*) (mN)	*t*	0	*t*	0	None	None	2	15	15
0.5:1A	Step (0.5**F*) (mN)	Step *F* (mN)	*t*	0	*t*	0	None	None	10	15	0
0.5:1B	Step (0.5**F*) (mN)	Step *F* (mN)	*t*	0	*t*	0	None	None	2	15	15
1:0.5A	Step *F* (mN)	Step (0.5**F*) (mN)	*t*	0	*t*	0	None	None	10	15	0
1:0.5B	Step *F* (mN)	Step (0.5**F*) (mN)	*t*	0	*t*	0	None	None	2	15	15

7.2) Prepare a displacement-controlled testing protocol at a loading rate of 4.42 N/min:

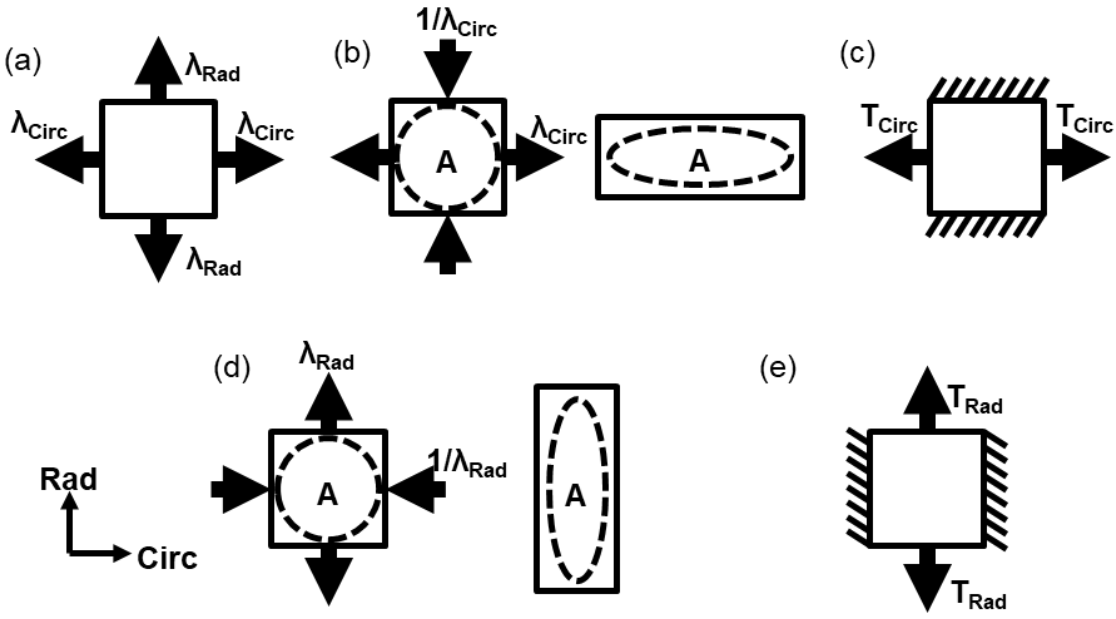

Figure C-7: Schematic of the displacement-controlled biaxial testing protocols.

7.2.1) Biaxial stretching in the *X*-direction and *Y*-direction to the displacements associated with the peak circumferential and radial stretches, respectively (Figure C-7a).

7.2.2) Pure shear along the *X*-direction—stretching in the *X*-direction associated with the peak circumferential stretch and shortening in the *Y*-direction, *while keeping the dashed area constant under deformation* (Figure C-7b).

7.2.3) Constrained uniaxial stretching along the *X*-direction (Figure C-7c).

7.2.4) Pure shear along the *Y*-direction (Figure C-7d).

7.2.5) Constrained uniaxial stretching along the *Y*-direction (Figure C-7e).

7.2.6) Between each of these steps, construct a rest "cycle" of one minute that holds

the tissue at the original mounted configuration. Retrieve data from the last two cycles of each loading ratio for data processing and analyses (Step 9). Refer to Table C-2 for a detailed description of the protocols to be established.

Table C-2: Full testing parameters for all protocols of the displacement-controlled testing scheme.

Set Name	*X*-Axis	*Y*-Axis	Stretch (S)	Hold (S)	Recover (S)	Rest (S)	XPreload (mN)	YPreload (mN)	Reps	Data (Hz)	Image (Hz)
FirstImage	Step 0.0 (mN)	Step 0.0 (mN)	1	0	1	0	0.0 (First)	0.0 (First)	1	1	1
1:1A	Ramp d_x (%)	Ramp d_y (%)	t	0	t	0	0.025*F (First)	0.025*F (First)	10	15	0
1:1B	Ramp d_x (%)	Ramp d_y (%)	t	0	t	0	None	None	2	15	15
Rest	Ramp 0.0 (%)	Ramp 0.0 (%)	0	0	0	60	None	None	1	15	0
PSXA	Ramp d_x (%)	Ramp $1/d_y$ (%)	t	0	t	0	None	None	10	15	0
PSXB	Ramp d_x (%)	Ramp $1/d_y$ (%)	t	0	t	0	None	None	2	15	15
Rest	Ramp 0.0 (%)	Ramp 0.0 (%)	0	0	0	60	None	None	1	15	0
PSYA	Ramp $1/d_x$ (%)	Ramp d_y (%)	t	0	t	0	None	None	10	15	0
PSYB	Ramp $1/d_x$ (%)	Ramp d_y (%)	t	0	t	0	None	None	2	15	15
Rest	Ramp 0.0 (%)	Ramp 0.0 (%)	0	0	0	60	None	None	1	15	0
CUXA	Ramp d_x (%)	Ramp 0.0 (%)	t	0	t	0	None	None	10	15	0
CUXB	Ramp d_x (%)	Ramp 0.0 (%)	t	0	t	0	None	None	2	15	15
Rest	Ramp 0.0 (%)	Ramp 0.0 (%)	0	0	0	60	None	None	1	15	0
CUYA	Ramp 0.0 (%)	Ramp d_y (%)	t	0	t	0	None	None	10	15	0
CUYB	Ramp 0.0 (%)	Ramp d_y (%)	t	0	t	0	None	None	2	15	15

7.3) Prepare a stress-relaxation protocol such that the tissue is loaded in each direction, at a loading rate of 4.42 N/min, to the displacements associated with the peak membrane tensions (Step 7.2) and held at that displacement for 15 minutes (Figure C-8). After 15 minutes the protocol should be set to recover the tissue to its original mounting configuration.

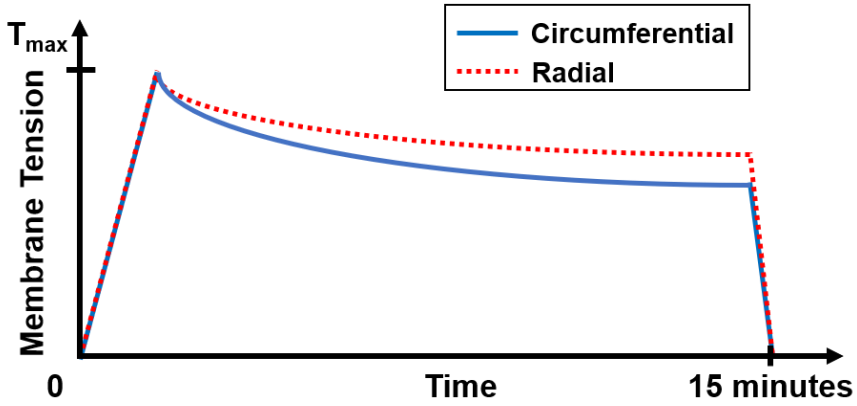

Figure C-8: Schematic illustration of the stress relaxation testing protocol.

8. Tissue Fixation, Histology, and Histology Image Analysis

8.1) Unmount the tissue from the biaxial testing system. Place the tissue into a container filled with 10% formalin, and then place the container in a refrigerated environment. Let the tissue be fixed for 24-48 hours, depending on the tissue's thickness.

8.2) After the tissue has been fixed in formalin for 24-48 hours, transfer the tissue to an 80% ethanol solution for later histology. The tissue should be stored in solution in a refrigerated environment at 4 °C.

8.3) Prepare the tissue for commercial histology analysis as per the vendor's instructions. If a certain leaflet constituent, such as collagen, elastin, glycosaminoglycans, etc., is of the study's interest, ensure that the appropriate histology stain is employed.

Histology slides may be visualized using a microscope to observe desired constituents.

8.4) Using an image processing program ImageJ (National Institute of Health, Bethesda, MD), perform color deconvolution methods to determine the percentage of each stained constituent in the tissue. For greater detail on these procedures, please refer to the citation [117].

9. Biaxial Testing Data Post Processing Procedures

9.1) Perform data image correlation (DIC) based tracking on the four fiducial markers from the images taken during the biaxial mechanical testing (Figure C-9) to determine the time-dependent marker positions:

$$\mathbf{x}_I(t) = \mathbf{X}_I + \mathbf{d}_I(t),\ I = 1 \sim 4, \tag{C.2}$$

where $\mathbf{X}_I$ and $\mathbf{x}_I(t)$ are the undeformed and deformed positions of the markers, respectively, and $\mathbf{d}_I(t)$ is the displacement vector of each marker.

9.1.1) If it is desired to perform the analysis with respect to the mounting configuration, let $\mathbf{X}_I$ be the marker positions in the undeformed state at the beginning of the biaxial test. If it is desired to perform the analysis with respect to the post-preconditioning deformation, let $\mathbf{X}_I$ be the marker positions at the end of the preconditioning protocol. The subsequent steps will be conducted in the same manner, regardless of the reference configuration chosen.

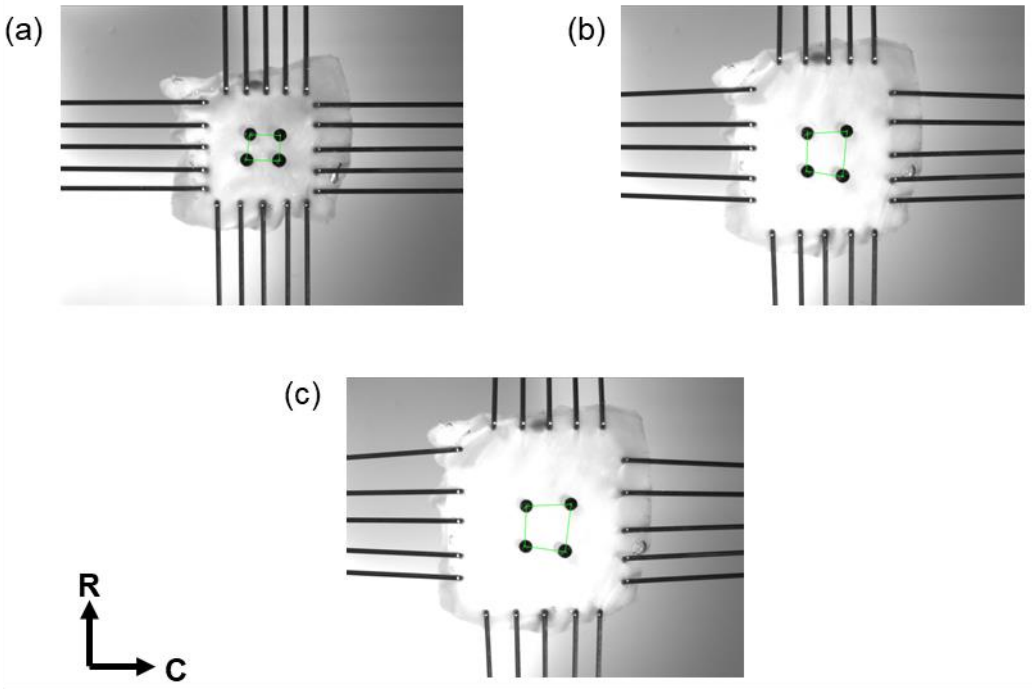

Figure C-9: Representative images illustrating the tracking of the coordinates of four fiducial markers during biaxial mechanical testing using a data image correlation (DIC) technique: (a) the tissue mounting configuration, (b) the configuration after the preconditioning step, and (c) the deformed configuration associated with the tissue specimen under mechanical loading.

9.2) Compute the deformation gradient **F** of the fiducial markers using a four-node bilinear finite element [12, 59, 119]:

$$\mathbf{F} = \mathbf{F}(\mathbf{X},t) = \frac{\partial \mathbf{x}}{\partial \mathbf{X}} = \begin{bmatrix} \sum_{I=1}^{4} B_{XI} u_I(t) & \sum_{I=1}^{4} B_{YI} u_I(t) \\ \sum_{I=1}^{4} B_{XI} v_I(t) & \sum_{I=1}^{4} B_{YI} v_I(t) \end{bmatrix}. \tag{C.3}$$

Here, B_{xI}'s and B_{yI}'s are the finite element shape function-derivatives in the *X*- and *Y*-directions for node I, respectively, and $u_I(t)$ and $v_I(t)$ are the time-dependent *X*- and *Y*-displacements, respectively, as previously determined from Step 9.1.1. Note the *X*-*Y*

coordinates were aligned to the tissue's circumferential and radial directions.

9.3) Compute the right Cauchy-Green deformation tensor **C** and the Green-Lagrange strain tensor **E**:

$$\mathbf{C} = \mathbf{F}^T\mathbf{F}\text{, and}\,\mathbf{E} = \frac{1}{2}(\mathbf{C} - \mathbf{I})\,. \tag{C.4}$$

Here, **I** is the second-order identity tensor. Determine the circumferential and radial stretches by taking the square roots of the principle values of **C**.

9.4) Determine the first Piola-Kirchhoff (1st-PK) stress tensor **P**

$$\mathbf{P} = \frac{1}{t}\begin{bmatrix} T_C & 0 \\ 0 & T_R \end{bmatrix}, \tag{C.5}$$

where t is the specimen's thickness, and T_C and T_R are the applied membrane tensions in the circumferential and radial directions, respectively. Also, compute other stress tensors, such as the Cauchy stress tensor $\boldsymbol{\sigma}$ and the second Piola-Kirchhoff (2nd-PK) stress tensor **S**, using:

$$\boldsymbol{\sigma} = J^{-1}\mathbf{P}\mathbf{F}^T \text{ and } \mathbf{S} = \mathbf{F}^{-1}\mathbf{P}\,. \tag{C.6}$$

where J is the Jacobian of the deformation gradient tensor **F**.

References

1. Addetia, K., Yamat, M., Mediratta, A., Medvedofsky, D., Patel, M., Ferrara, P., Mor-Avi, V., and Lang, R.M., Comprehensive two-dimensional interrogation of the tricuspid valve using knowledge derived from three-dimensional echocardiography. *Journal of the American Society of Echocardiography*, 2016. 29(1): pp. 74-82.
2. Aggarwal, A., An improved parameter estimation and comparison for soft tissue constitutive models containing an exponential function. *Biomechanics and Modeling in Mechanobiology*, 2017. 16(4): pp. 1309-1327.
3. Ambrosi, D., Ateshian, G.A., Arruda, E.M., Cowin, S.C., Dumais, J., Goriely, A., Holzapfel, G.A., Humphrey, J.D., Kemkemer, R., and Kuhl, E., Perspectives on biological growth and remodeling. *Journal of the Mechanics and Physics of Solids*, 2011. 59(4): pp. 863-883.
4. Antunes, M.J. and Barlow, J.B., Management of tricuspid valve regurgitation. *Heart*, 2007. 93(2): pp. 271-276.
5. Anwar, A.M., Folkert, J., and Soliman, O.I., *Clinical recognition of tricuspid valve disease*, in *Practical Manual of Tricuspid Valve Diseases*. 2018, Springer. pp. 25-48.
6. Aversa, A. and Careddu, E., *Image-Based Analysis of Tricuspid Valve Biomechanics: Towards a Novel Approach Integrating In Vitro 3D-Echocardiography and Finite Element Modelling*. 2017, Politecnico di Milano.
7. Ayoub, S., Lee, C.-H., Driesbaugh, K.H., Anselmo, W., Hughes, C.T., Ferrari, G., Gorman, R.C., Gorman, J.H., III, and Sacks, M.S., Regulation of valve interstitial

cell homeostasis by mechanical deformation: Implications for heart valve disease and surgical repair. *Journal of the Royal Society Interface*, 2017. 14(135): p. 20170580.

8. Badano, L.P., Ginghina, C., Easaw, J., Muraru, D., Grillo, M.T., Lancellotti, P., Pinamonti, B., Coghlan, G., Marra, M.P., and Popescu, B.A., Right ventricle in pulmonary arterial hypertension: Haemodynamics, structural changes, imaging, and proposal of a study protocol aimed to assess remodelling and treatment effects. *European Journal of Echocardiography*, 2009. 11(1): pp. 27-37.
9. Badano, L.P., Muraru, D., and Enriquez-Sarano, M., Assessment of functional tricuspid regurgitation. *European Heart Journal*, 2013. 34(25): pp. 1875-1885.
10. Balachandran, K., Konduri, S., Sucosky, P., Jo, H., and Yoganathan, A.P., An ex vivo study of the biological properties of porcine aortic valves in response to circumferential cyclic stretch. *Annals of Biomedical Engineering*, 2006. 34(11): pp. 1655-1665.
11. Ballazhi, F., Feyrer, R., Heim, C., Tandler, R., Kondruweit, M., Weyand, M., and Harig, F., Isolated Surgery of Functional Tricuspid Valve Regurgitation-Preoperative Predictors of Adverse Outcome. *The Thoracic and Cardiovascular Surgeon*, 2016. 64(S 01): p. OP145.
12. Billiar, K. and Sacks, M., A method to quantify the fiber kinematics of planar tissues under biaxial stretch. *Journal of biomechanics*, 1997. 30(7): pp. 753-756.
13. Billiar, K.L. and Sacks, M.S., Biaxial mechanical properties of the native and glutaraldehyde-treated aortic valve cusp: Part II—A structural constitutive model. *Journal of Biomechanical Engineering*, 2000. 122(4): pp. 327-335.

14. Billiar, K.L. and Sacks, M.S., Biaxial mechanical properties of the natural and glutaraldehyde treated aortic valve cusp-Part I: Experimental results. *Journal of Biomechanical Engineering*, 2000. 122(1): pp. 23-30.

15. Braunwald, N.S., Ross Jr, J., and Morrow, A.G., Conservative management of tricuspid regurgitation in patients undergoing mitral valve replacement. *Circulation*, 1967. 35(4s1): pp. I-63-I-69.

16. Bujok, P., Tvrdík, J., and Poláková, R. *Differential evolution with rotation-invariant mutation and competing-strategies adaptation*. in *2014 IEEE Congress on Evolutionary Computation (CEC)*. 2014. IEEE.

17. Cacho, F., Elbischger, P.J., Rodriguez, J.F., Doblaré, M., and Holzapfel, G.A., A constitutive model for fibrous tissues considering collagen fiber crimp. *International Journal of Non-Linear Mechanics*, 2007. 42(2): pp. 391-402.

18. Calafiore, A.M., Gallina, S., Iacò, A.L., Contini, M., Bivona, A., Gagliardi, M., Bosco, P., and Di Mauro, M., Mitral valve surgery for functional mitral regurgitation: Should moderate-or-more tricuspid regurgitation be treated? A propensity score analysis. *The Annals of Thoracic Surgery*, 2009. 87(3): pp. 698-703.

19. Carpentier, A., A new reconstructive operation for correction of mitral and tricuspid insufficiency. *Journal of Thoracic Cardiovascular Surgery*, 1971. 61: pp. 1-13.

20. Casa, L.D., Dolensky, J.R., Spinner, E.M., Veledar, E., Lerakis, S., and Yoganathan, A.P., Impact of pulmonary hypertension on tricuspid valve function. *Annals of Biomedical Engineering*, 2013. 41(4): pp. 709-724.

21. Chan, V., Burwash, I.G., Lam, B.-K., Auyeung, T., Tran, A., Mesana, T.G., and

Ruel, M., Clinical and echocardiographic impact of functional tricuspid regurgitation repair at the time of mitral valve replacement. *The Annals of Thoracic Surgery*, 2009. 88(4): pp. 1209-1215.

22. Clark, R., Stress-strain characteristics of fresh and frozen human aortic and mitral leaflets and chordae tendineae. Implications for clinical use. *Journal of Thoracic and Cardiovascular Surgery*, 1973. 66(2): pp. 202-208.

23. Clark, R. and Finke, E., Scanning and light microscopy of human aortic leaflets in stressed and relaxed states. *The Journal of Thoracic and Cardiovascular Surgery*, 1974. 67(5): p. 792.

24. Cochran, R.P. and Kuzelman, K.S., Comparison of viscoelastic properties of suture versus porcine mitral valve chordae tendineae. *Journal of Cardiac Surgery*, 1991. 6(4): pp. 508-513.

25. Colli, A., Manzan, E., Rucinskas, K., Janusauskas, V., Zucchetta, F., Zakarkaitė, D., Aidietis, A., and Gerosa, G., Acute safety and efficacy of the NeoChord procedure. *Interactive CardioVascular and Thoracic Surgery*, 2015. 20(5): pp. 575-581.

26. Come, P.C. and Riley, M.F., Tricuspid anular dilatation and failure of tricuspid leaflet coaptation in tricuspid regurgitation. *The American Journal of Cardiology*, 1985. 55(5): pp. 599-601.

27. De Hart, J., Peters, G.W.M., Schreurs, P.J.G., and Baaijens, F.P.T., A three-dimensional computational analysis of fluid–structure interaction in the aortic valve. *Journal of Biomechanics*, 2003. 36(1): pp. 103-112.

28. De Vega, N., De Rabago, G., Castillon, L., Moreno, T., and Azpitarte, J., A new

tricuspid repair. Short-term clinical results in 23 cases. *The Journal of Cardiovascular Surgery*, 1973. 14: pp. 384-386.

29. Debelle, L. and Alix, A.J., The structures of elastins and their function. *Biochimie*, 1999. 81(10): pp. 981-994.

30. Debelle, L. and Tamburro, A., Elastin: molecular description and function. *The International Journal of Biochemistry & Cell Biology*, 1999. 31(2): pp. 261-272.

31. Di Mauro, M., Bezante, G.P., Di Baldassarre, A., Clemente, D., Cardinali, A., Acitelli, A., Salerni, S., Penco, M., Calafiore, A.M., and Gallina, S., Functional tricuspid regurgitation: An underestimated issue. *International Journal of Cardiology*, 2013. 168(2): pp. 707-715.

32. Drach, A., Khalighi, A.H., ter Huurne, F.M., Lee, C.-H., Bloodworth, C., Pierce, E.L., Jensen, M.O., Yoganathan, A.P., and Sacks, M.S., Population-averaged geometric model of mitral valve from patient-specific imaging data. *Journal of Medical Devices*, 2015. 9(3): p. 030952.

33. Dreyfus, G.D., Corbi, P.J., Chan, K.M.J., and Bahrami, T., Secondary tricuspid regurgitation or dilatation: Which should be the criteria for surgical repair? *Annals of Thoracic Surgery*, 2005. 79(1): pp. 127-132.

34. Eckert, C.E., Fan, R., Mikulis, B., Barron, M., Carruthers, C.A., Friebe, V.M., Vyavahare, N.R., and Sacks, M.S., On the biomechanical role of glycosaminoglycans in the aortic heart valve leaflet. *Acta Biomaterialia*, 2013. 9(1): pp. 4653-4660.

35. Fan, R. and Sacks, M.S., Simulation of planar soft tissues using a structural constitutive model: Finite element implementation and validation. *Journal of*

Biomechanics, 2014. 47(9): pp. 2043-2054.

36. Feigenbaum, H., Clinical applications of echocardiography. *Progress in Cardiovascular Diseases*, 1972. 14(6): pp. 531-558.

37. Feng, Y., Lee, C.-H., Sun, L., Ji, S., and Zhao, X., Characterizing white matter tissue in large strain via asymmetric indentation and inverse finite element modeling. *Journal of the Mechanical Behavior of Biomedical Materials*, 2017. 65: pp. 490-501.

38. Foutz, T.L., Stone, E.A., and Abrams, C.F., Effects of freezing on mechanical properties of rat skin. *American Journal of Veterinary Research*, 1992. 53(5): pp. 788-792.

39. Fukuda, S., Gillinov, A.M., McCarthy, P.M., Matsumura, Y., Thomas, J.D., and Shiota, T., Echocardiographic follow-up of tricuspid annuloplasty with a new three-dimensional ring in patients with functional tricuspid regurgitation. *Journal of the American Society of Echocardiography*, 2007. 20(11): pp. 1236-1242.

40. Fukuda, S., Gillinov, A.M., McCarthy, P.M., Stewart, W.J., Song, J.-M., Kihara, T., Daimon, M., Shin, M.-S., Thomas, J.D., and Shiota, T., Determinants of recurrent or residual functional tricuspid regurgitation after tricuspid annuloplasty. *Circulation*, 2006. 114(1 suppl): pp. I-582-I-587.

41. Fukuda, S., Gillinov, A.M., Song, J.-M., Daimon, M., Kongsaerepong, V., Thomas, J.D., and Shiota, T., Echocardiographic insights into atrial and ventricular mechanisms of functional tricuspid regurgitation. *American Heart Journal*, 2006. 152(6): pp. 1208-1214.

42. Fukuda, S., Song, J.-M., Gillinov, A.M., McCarthy, P.M., Daimon, M.,

Kongsaerepong, V., Thomas, J.D., and Shiota, T., Tricuspid valve tethering predicts residual tricuspid regurgitation after tricuspid annuloplasty. *Circulation*, 2005. 111(8): pp. 975-979.

43. Fung, Y.C., Fronek, K., and Patitucci, P., Pseudoelasticity of arteries and the choice of its mathematical expression. *American Journal of Physiology-Heart and Circulatory Physiology*, 1979. 237(5): pp. H620-H631.

44. Gasser, T.C., Ogden, R.W., and Holzapfel, G.A., Hyperelastic modelling of arterial layers with distributed collagen fibre orientations. *Journal of the Royal Society Interface*, 2005. 3(6): pp. 15-35.

45. Gonzalez-Vilchez, F., Zarauza, J., de Prada, J.A.V., Durán, R.M., Ruano, J., Delgado, C., and Figueroa, A., Assessment of tricuspid regurgitation by Doppler color flow imaging: angiographic correlation. *International Journal of Cardiology*, 1994. 44(3): pp. 275-283.

46. Grashow, J.S., Sacks, M.S., Liao, J., and Yoganathan, A.P., Planar biaxial creep and stress relaxation of the mitral valve anterior leaflet. *Annals of Biomedical Engineering*, 2006. 34(10): pp. 1509-1518.

47. Grashow, J.S., Yoganathan, A.P., and Sacks, M.S., Biaixal stress–stretch behavior of the mitral valve anterior leaflet at physiologic strain rates. *Annals of Biomedical Engineering*, 2006. 34(2): pp. 315-325.

48. Gupta, V., Werdenberg, J.A., Blevins, T.L., and Grande-Allen, K.J., Synthesis of glycosaminoglycans in differently loaded regions of collagen gels seeded with valvular interstitial cells. *Tissue Engineering*, 2007. 13(1): pp. 41-49.

49. Haj-Ali, R., Marom, G., Zekry, S.B., Rosenfeld, M., and Raanani, E., A general

three-dimensional parametric geometry of the native aortic valve and root for biomechanical modeling. *Journal of Biomechanics*, 2012. 45(14): pp. 2392-2397.

50. Hamid, M.S., Sabbah, H.N., and Stein, P.D., Vibrational analysis of bioprosthetic heart valve leaflets using numerical models: Effects of leaflet stiffening, calcification, and perforation. *Circulation Research*, 1987. 61(5): pp. 687-694.

51. Heyden, S., Nagler, A., Bertoglio, C., Biehler, J., Gee, M.W., Wall, W.A., and Ortiz, M., Material modeling of cardiac valve tissue: Experiments, constitutive analysis and numerical investigation. *Journal of Biomechanics*, 2015. 48(16): pp. 4287-4296.

52. Hinderliter, A.L., Willis, P.W., Long, W.A., Clarke, W.R., Ralph, D., Caldwell, E.J., Williams, W., Ettinger, N.A., Hill, N.S., and Summer, W.R., Frequency and severity of tricuspid regurgitation determined by Doppler echocardiography in primary pulmonary hypertension. *American Journal of Cardiology*, 2003. 91(8): pp. 1033-1037.

53. Hiro, M.E., Jouan, J., Pagel, M.R., Lansac, E., Lim, K.H., Lim, H.-S., and Duran, C.M.G., Sonometric study of the normal tricuspid valve annulus in sheep. *Journal of Heart Valve Disease*, 2004. 13(3): pp. 452-460.

54. Holzapfel, G.A., Gasser, T.C., and Ogden, R.W., A new constitutive framework for arterial wall mechanics and a comparative study of material models. *Journal of Elasticity and the Physical Science of Solids*, 2000. 61(1-3): pp. 1-48.

55. Holzapfel, G.A., Niestrawska, J.A., Ogden, R.W., Reinisch, A.J., and Schriefl, A.J., Modelling non-symmetric collagen fibre dispersion in arterial walls. *Journal of the Royal Society Interface*, 2015. 12(106): p. 20150188.

56. Holzapfel, G.A. and Ogden, R.W., Constitutive modelling of arteries. *Proceedings of the Royal Society of London, Series A; Mathematical and Physical Sciences*, 2010. 466(2118): pp. 1551-1597.

57. Hsu, M.-C., Kamensky, D., Bazilevs, Y., Sacks, M.S., and Hughes, T.J., Fluid–structure interaction analysis of bioprosthetic heart valves: Significance of arterial wall deformation. *Computational Mechanics*, 2014. 54(4): pp. 1055-1071.

58. Humphrey, J.D. and Rajagopal, K.R., A constrained mixture model for growth and remodeling of soft tissues. *Mathematical Models and Methods in Applied Sciences*, 2002. 12(03): pp. 407-430.

59. Jett, S., Laurence, D., Kunkel, R., Babu, A.R., Kramer, K., Baumwart, R., Towner, R., Wu, Y., and Lee, C.-H., An investigation of the anisotropic mechanical properties and anatomical structure of porcine atrioventricular heart valves. *Journal of the mechanical behavior of biomedical materials*, 2018. 87: pp. 155-171.

60. Jouan, J., Pagel, M.R., Hiro, M.E., Lim, K.H., Lansac, E., and Duran, C.M., Further information from a sonometric study of the normal tricuspid valve annulus in sheep: geometric changes during the cardiac cycle. *Journal of Heart Valve Disease*, 2007. 16(5): p. 511.

61. Kamensky, D., Hsu, M.-C., Schillinger, D., Evans, J.A., Aggarwal, A., Bazilevs, Y., Sacks, M.S., and Hughes, T.J., An immersogeometric variational framework for fluid–structure interaction: application to bioprosthetic heart valves. *Computer Methods in Applied Mechanics and Engineering*, 2015. 284: pp. 1005-1053.

62. Kamensky, D., Xu, F., Lee, C.-H., Yan, J., Bazilevs, Y., and Hsu, M.-C., A contact formulation based on a volumetric potential: Application to isogeometric

simulations of atrioventricular valves. *Computer Methods in Applied Mechanics and Engineering*, 2018. 330: pp. 522-546.

63. Khalighi, A.H., Drach, A., Bloodworth, C.H.t., Pierce, E.L., Yoganathan, A.P., Gorman, R.C., Gorman, J.H., 3rd, and Sacks, M.S., Mitral Valve Chordae Tendineae: Topological and Geometrical Characterization. *Annals of Biomedical Engineering*, 2017. 45(2): pp. 378-393.

64. Khalighi, A.H., Rego, B.V., Drach, A., Gorman, R.C., Gorman, J.H., 3rd, and Sacks, M.S., Development of a functionally equivalent model of the mitral valve chordae tendineae through topology optimization. *Annals of Biomedical Engineering*, 2019. 47(1): pp. 60-74.

65. Khoiy, K.A. and Amini, R., On the biaxial mechanical response of porcine tricuspid valve leaflets. *Journal of Biomechanical Engineering*, 2016. 138(10): pp. 104504-104504-6.

66. Khoiy, K.A., Asgarian, K.T., Loth, F., and Amini, R., Dilation of tricuspid valve annulus immediately after rupture of chordae tendineae in ex-vivo porcine hearts. *PLOS One*, 2018. 13(11): p. e0206744.

67. Khoiy, K.A., Pant, A.D., and Amini, R., Quantification of material constants for a phenomenological constitutive model of porcine tricuspid valve leaflets for simulation applications. *Journal of Biomechanical Engineering*, 2018. 140(9): p. 094503.

68. Kim, J.B., Jung, S.-H., Choo, S.J., Chung, C.H., and Lee, J.W., Surgical outcomes of severe tricuspid regurgitation: predictors of adverse clinical outcomes. *Heart*, 2013. 99(3): pp. 181-187.

69. Kim, Y.-J., Kwon, D.-A., Kim, H.-K., Park, J.-S., Hahn, S., Kim, K.-H., Kim, K.-B., Sohn, D.-W., Ahn, H., and Oh, B.-H., Determinants of surgical outcome in patients with isolated tricuspid regurgitation. *Circulation*, 2009. 120(17): pp. 1672-1678.

70. Kohandel, M., Sivaloganathan, S., and Tenti, G., Estimation of the quasi-linear viscoelastic parameters using a genetic algorithm. *Mathematical and Computer Modelling*, 2008. 47(3-4): pp. 266-270.

71. Kong, F., Pham, T., Martin, C., McKay, R., Primiano, C., Hashim, S., Kodali, S., and Sun, W., Finite element analysis of tricuspid valve deformation from multi-slice computed tomography images. *Annals of Biomedical Engineering*, 2018: pp. 1-16.

72. Kramer, K., Ross, C., Laurence, D., Babu, A., Wu, Y., Towner, R., Mir, A., Burkhart, H.M., Holzapfel, G.A., and Lee, C.-H., An investigation of layer-specific tissue biomechanics of porcine atrioventricular heart valve leaflets. *Acta Biomaterialia*, Under review.

73. Kroon, M. and Holzapfel, G.A., A new constitutive model for multi-layered collagenous tissues. *Journal of Biomechanics*, 2008. 41(12): pp. 2766-2771.

74. Kunzelman, K.S. and Cochran, R.P., Stress/strain characteristics of porcine mitral valve tissue: parallel versus perpendicular collagen orientation. *Journal of Cardiac Surgery*, 1992. 7(1): pp. 71-78.

75. Kunzelman, K.S., Cochran, R.P., Chuong, C., Ring, W.S., Verrier, E.D., and Eberhart, R.D., Finite element analysis of the mitral valve. *Journal of Heart Valve Disease*, 1993. 2(3): pp. 326-340.

76. Kunzelman, K.S., Cochran, R.P., Murphree, S.S., Ring, W.S., Verrier, E.D., and Eberhart, R.C., Differential collagen distribution in the mitral valve and its influence on biomechanical behaviour. *Journal of Heart Valve Disease*, 1993. 2(2): pp. 236-244.

77. Kunzelman, K.S., Einstein, D.R., and Cochran, R.P., Fluid–structure interaction models of the mitral valve: function in normal and pathological states. *Philosophical Transactions of the Royal Society B: Biological Sciences*, 2007. 362(1484): pp. 1393-1406.

78. Lacerda, C.M., Kisiday, J., Johnson, B., and Orton, E.C., Local serotonin mediates cyclic strain-induced phenotype transformation, matrix degradation, and glycosaminoglycan synthesis in cultured sheep mitral valves. *American Journal of Physiology-Heart and Circulatory Physiology*, 2012.

79. Lancellotti, P., Moura, L., Pierard, L.A., Agricola, E., Popescu, B.A., Tribouilloy, C., Hagendorff, A., Monin, J.-L., Badano, L., and Zamorano, J.L., European Association of Echocardiography recommendations for the assessment of valvular regurgitation. Part 2: Mitral and tricuspid regurgitation (native valve disease). *European Journal of Echocardiography*, 2010. 11(4): pp. 307-332.

80. Lancellotti, P., Tribouilloy, C., Hagendorff, A., Moura, L., Popescu, B.A., Agricola, E., Monin, J.-L., Pierard, L.A., Badano, L., and Zamorano, J.L., European Association of Echocardiography recommendations for the assessment of valvular regurgitation. Part 1: Aortic and pulmonary regurgitation (native valve disease). *European Journal of Echocardiography*, 2010. 11(3): pp. 223-244.

81. Lau, K.D., Diaz, V., Scambler, P., and Burriesci, G., Mitral valve dynamics in

structural and fluid–structure interaction models. *Medical Engineering & Physics*, 2010. 32(9): pp. 1057-1064.

82. Laurence, D., Ross, C., Jett, S., Johns, C., Echols, A., Baumwart, R., Towner, R., Liao, J., Bajona, P., Wu, Y., and Lee, C.-H., An investigation of regional variations in the biaxial mechanical properties and stress relaxation behaviors of porcine atrioventricular heart valve leaflets. *Journal of Biomechanics*, 2019. 83: pp. 16-27.
83. Lee, C.-H., Amini, R., Gorman, R.C., Gorman, J.H., 3rd, and Sacks, M.S., An inverse modeling approach for stress estimation in mitral valve anterior leaflet valvuloplasty for in-vivo valvular biomaterial assessment. *Journal of Biomechanics*, 2014. 47(9): pp. 2055-2063.
84. Lee, C.-H., Carruthers, C.A., Ayoub, S., Gorman, R.C., Gorman, J.H., 3rd, and Sacks, M.S., Quantification and simulation of layer-specific mitral valve interstitial cells deformation under physiological loading. *Journal of Theoretical Biology*, 2015. 373: pp. 26-39.
85. Lee, C.-H., Rabbah, J.-P., Yoganathan, A.P., Gorman, R.C., Gorman, J.H., 3rd, and Sacks, M.S., On the effects of leaflet microstructure and constitutive model on the closing behavior of the mitral valve. *Biomechanics and Modeling in Mechanobiology*, 2015. 14(6): pp. 1281-1302.
86. Lee, C.-H., Zhang, W., Feaver, K., Gorman, R.C., Gorman, J.H., 3rd, and Sacks, M.S., On the *in vivo* function of the mitral heart valve leaflet: Insights into tissue–interstitial cell biomechanical coupling. *Biomechanics and Modeling in Mechanobiology*, 2017. 16(5): pp. 1613-1632.
87. Mas, P.T., Rodríguez-Palomares, J.F., and Antunes, M.J., Secondary tricuspid

valve regurgitation: A forgotten entity. *Heart*, 2015. 101(22): pp. 1840-1848.

88. Matsuyama, K., Matsumoto, M., Sugita, T., Nishizawa, J., Tokuda, Y., and Matsuo, T., Predictors of residual tricuspid regurgitation after mitral valve surgery. *The Annals of Thoracic Surgery*, 2003. 75(6): pp. 1826-1828.

89. Mattson, J.M., Turcotte, R., and Zhang, Y., Glycosaminoglycans contribute to extracellular matrix fiber recruitment and arterial wall mechanics. *Biomechanics and Modeling in Mechanobiology*, 2017. 16(1): pp. 213-225.

90. May-Newman, K. and Yin, F.C., Biaxial mechanical behavior of excised porcine mitral valve leaflets. *American Journal of Physiology-Heart and Circulatory Physiology*, 1995. 269(4): pp. H1319-H1327.

91. May-Newman, K. and Yin, F.C., A constitutive law for mitral valve tissue. *Journal of Biomechanical Engineering*, 1998. 120(1): pp. 38-47.

92. McLaughlin, V.V., Archer, S.L., Badesch, D.B., Barst, R.J., Farber, H.W., Lindner, J.R., Mathier, M.A., McGoon, M.D., Park, M.H., and Rosenson, R.S., ACCF/AHA 2009 expert consensus document on pulmonary hypertension: A report of the American College of Cardiology Foundation Task Force on expert consensus documents and the American Heart Association developed in collaboration with the American College of Chest Physicians; American Thoracic Society, Inc.; and the Pulmonary Hypertension Association. *Journal of the American College of Cardiology*, 2009. 53(17): pp. 1573-1619.

93. Merryman, W.D., Lukoff, H.D., Long, R.A., Engelmayr Jr, G.C., Hopkins, R.A., and Sacks, M.S., Synergistic effects of cyclic tension and transforming growth factor-β1 on the aortic valve myofibroblast. *Cardiovascular Pathology*, 2007.

16(5): pp. 268-276.

94. Min, S.-Y., Song, J.-M., Kim, J.-H., Jang, M.-K., Kim, Y.-J., Song, H., Kim, D.-H., Lee, J.W., Kang, D.-H., and Song, J.-K., Geometric changes after tricuspid annuloplasty and predictors of residual tricuspid regurgitation: A real-time three-dimensional echocardiography study. *European Heart Journal*, 2010. 31(23): pp. 2871-2880.

95. Missirlis, Y. and Chong, M., Aortic valve mechanics--Part I: Material properties of natural porcine aortic valves. *Journal of Bioengineering*, 1978. 2(3-4): pp. 287-300.

96. Missirlis, Y.F., *In-vitro Studies of Human Aortic Valve Mechanics*. 1974, Rice University.

97. Morganti, S., Conti, M., Aiello, M., Valentini, A., Mazzola, A., Reali, A., and Auricchio, F., Simulation of transcatheter aortic valve implantation through patient-specific finite element analysis: Two clinical cases. *Journal of Biomechanics*, 2014. 47(11): pp. 2547-2555.

98. Nagueh, S.F., Kopelen, H.A., and Zoghbi, W.A., Relation of mean right atrial pressure to echocardiographic and Doppler parameters of right atrial and right ventricular function. *Circulation*, 1996. 93(6): pp. 1160-1169.

99. Navia, J.L., Brozzi, N.A., Klein, A.L., Ling, L.F., Kittayarak, C., Nowicki, E.R., Batizy, L.H., Zhong, J., and Blackstone, E.H., Moderate tricuspid regurgitation with left-sided degenerative heart valve disease: To repair or not to repair? *The Annals of Thoracic Surgery*, 2012. 93(1): pp. 59-69.

100. Navia, J.L., Nowicki, E.R., Blackstone, E.H., Brozzi, N.A., Nento, D.E., Atik, F.A., Rajeswaran, J., Gillinov, A.M., Svensson, L.G., and Lytle, B.W., Surgical

management of secondary tricuspid valve regurgitation: Annulus, commissure, or leaflet procedure? *The Journal of Thoracic and Cardiovascular Surgery*, 2010. 139(6): pp. 1473-1482. e5.

101. Neri, F. and Tirronen, V., Recent advances in differential evolution: A survey and experimental analysis. *Artificial Intelligence Review*, 2010. 33(1-2): pp. 61-106.

102. Nicosia, M.A., Cochran, R.P., Einstein, D.R., Rutland, C.J., and Kunzelman, K.S., A coupled fluid-structure finite element model of the aortic valve and root. *Journal of Heart Valve Disease*, 2003. 12(6): pp. 781-789.

103. Nishimura, R.A., Otto, C.M., Bonow, R.O., Carabello, B.A., Erwin, J.P., Guyton, R.A., O'Gara, P.T., Ruiz, C.E., Skubas, N.J., and Sorajja, P., 2014 AHA/ACC guideline for the management of patients with valvular heart disease: Executive summary: A report of the American College of Cardiology/American Heart Association Task Force on Practice Guidelines. *Journal of the American College of Cardiology*, 2014. 63(22): pp. 2438-2488.

104. Onoda, K., Yasuda, F., Takao, M., Shimono, T., Tanaka, K., Shimpo, H., and Yada, I., Long-term follow-up after Carpentier-Edwards ring annuloplasty for tricuspid regurgitation. *The Annals of Thoracic Surgery*, 2000. 70(3): pp. 796-799.

105. Padala, M., Patient-specific computational biomechanical modeling to guide mitral valve repair strategy: Practicality and value? *Journal of Thoracic and Cardiovascular Surgery*, 2018. 155(2): pp. 606-607.

106. Park, Y.-H., Song, J.-M., Lee, E.-Y., Kim, Y.-J., Kang, D.-H., and Song, J.-K., Geometric and hemodynamic determinants of functional tricuspid regurgitation: a real-time three-dimensional echocardiography study. *International Journal of*

Cardiology, 2008. 124(2): pp. 160-165.

107. Pedrosa Silva, R.C., Lopes, R.A., and Guimarães, F.G. *Self-adaptive mutation in the differential evolution*. in *Proceedings of the 13th Annual Conference on Genetic and Evolutionary Computation*. 2011. ACM.

108. Pham, T., Sulejmani, F., Shin, E., Wang, D., and Sun, W., Quantification and comparison of the mechanical properties of four human cardiac valves. *Acta Biomaterialia*, 2017. 54: pp. 345-355.

109. Phillips, M.R., Daly, R.C., Schaff, H.V., Dearani, J.A., Mullany, C.J., and Orszulak, T.A., Repair of anterior leaflet mitral valve prolapse: Chordal replacement versus chordal shortening. *Annals of Thoracic Surgery*, 2000. 69(1): pp. 25-29.

110. Pokutta-Paskaleva, A., Sulejmani, F., DelRocini, M., and Sun, W., Comparative mechanical, morphological, and microstructural characterization of porcine mitral and tricuspid leaflets and chordae tendineae. *Acta Biomaterialia*, 2019. 85: pp. 241-252.

111. Pozzoli, A., Buzzatti, N., Vicentini, L., DE, M.B., and Alfieri, O., Results of tricuspid valve surgery for functional tricuspid regurgitation: Acute and long-term outcomes and predictors of failure. *Minerva Cardioangiologica*, 2017. 65(5): pp. 491-499.

112. Prot, V., Skallerud, B., and Holzapfel, G.A., Transversely isotropic membrane shells with application to mitral valve mechanics. Constitutive modelling and finite element implementation. *International Journal for Numerical Methods in Engineering*, 2007. 71(8): pp. 987-1008.

113. Prot, V., Skallerud, B., Sommer, G., and Holzapfel, G.A., On modelling and analysis of healthy and pathological human mitral valves: Two case studies. *Journal of the Mechanical Behavior of Biomedical Materials*, 2010. 3(2): pp. 167-177.

114. Rogers, J.H. and Bolling, S.F., The tricuspid valve: Current perspective and evolving management of tricuspid regurgitation. *Circulation*, 2009. 119(20): pp. 2718-2725.

115. Ross, C., Laurence, D., Richardson, J., Babu, A., Evans, L., Beyer, E., Wu, Y., Towner, R., Fung, K.-M., Mir, A., Burkhart, H.M., Holzapfel, G.A., and Lee, C.-H., An investigation of the glycosaminoglycan contribution to biaxial mechanical behaviors of porcine atrioventricular heart valve leaflets. *Journal of the Royal Society Interface*, Under review.

116. Ross, C., Laurence, D., Wu, Y., and Lee, C.-H., Biaxial mechanical characterizations of atrioventricular heart valves. *Journal of Visualized Experiments*, 2019. 146: p. e59170.

117. Ruifrok, A.C. and Johnston, D.A., Quantification of histochemical staining by color deconvolution. *Analytical and Quantitative Cytology and Histology*, 2001. 23(4): pp. 291-299.

118. Sacco, J.J., Botten, J., Macbeth, F., Bagust, A., and Clark, P., The average body surface area of adult cancer patients in the UK: A multicentre retrospective study. *PloS one*, 2010. 5(1): p. e8933.

119. Sacks, M.S., Biaxial mechanical evaluation of planar biological materials. *Journal of Elasticity*, 2000. 61(1): p. 199.

120. Sacks, M.S., Incorporation of experimentally-derived fiber orientation into a structural constitutive model for planar collagenous tissues. *Journal of Biomechanical Engineering*, 2003. 125(2): pp. 280-287.

121. Sacks, M.S. and Sun, W., Multiaxial mechanical behavior of biological materials. *Annual Review of Biomedical Engineering*, 2003. 5(1): pp. 251-284.

122. Sahasakul, Y., Edwards, W.D., Naessens, J.M., and Tajik, A.J., Age-related changes in aortic and mitral valve thickness: Implications for two-dimensional echocardiography based on an autopsy study of 200 normal human hearts. *The American Journal of Cardiology*, 1988. 62(7): pp. 424-430.

123. Sauren, A., Van Hout, M., Van Steenhoven, A., Veldpaus, F., and Janssen, J., The mechanical properties of porcine aortic valve tissues. *Journal of Biomechanics*, 1983. 16(5): pp. 327-337.

124. Silver, M.D., Lam, J.H.C., Ranganathan, N., and Wigle, E.D., Morphology of the human tricuspid valve. *Circulation*, 1971. 43(3): pp. 333-348.

125. Singh-Gryzbon, S., Sadri, V., Toma, M., Pierce, E.L., Wei, Z.A., and Yoganathan, A.P., Development of a computational method for simulating tricuspid valve dynamics. *Annals of Biomedical Engineering*, 2019: pp. 1-13.

126. Smedira, N.G., Selman, R., Cosgrove, D.M., McCarthy, P.M., Lytle, B.W., Taylor, P.C., Apperson-Hansen, C., Stewart, R.W., and Loop, F.D., Repair of anterior leaflet prolapse: Chordal transfer is superior to chordal shortening. *Journal of Thoracic and Cardiovascular Surgery*, 1996. 112(2): pp. 287-292.

127. Song, J.-M., Jang, M.-K., Kim, Y.-J., Kim, D.-H., Kang, D.-H., and Song, J.-K., Right ventricular remodeling determines tricuspid valve geometry and the severity

of functional tricuspid regurgitation: A real-time 3-dimensional echocardiography study. *Korean Circulation Journal*, 2010. 40(9): pp. 448-453.

128. Sousa, U.M., Grare, P., Jebara, V., Fuzelier, J.F., Portoghese, M., Acar, C., Relland, J., Mihaileanu, S., Fabiani, J.N., and Carpentier, A., Transposition of chordae in mitral valve repair. Mid-term results. *Circulation*, 1993. 88(5 Pt 2): pp. II35-8.

129. Spinner, E.M., Lerakis, S., Higginson, J., Pernetz, M., Howell, S., Veledar, E., and Yoganathan, A.P., Correlates of tricuspid regurgitation as determined by 3D echocardiography: Pulmonary arterial pressure, ventricle geometry, annular dilatation, and papillary muscle displacement. *Circulation: Cardiovascular Imaging*, 2012. 5(1): pp. 43-50.

130. Spinner, E.M., Shannon, P., Buice, D., Jimenez, J.H., Veledar, E., del Nido, P.J., Adams, D.H., and Yoganathan, A.P., *In vitro* characterization of the mechanisms responsible for functional tricuspid regurgitation. *Circulation*, 2011. 124(8): pp. 920-929.

131. Stella, J.A., Liao, J., and Sacks, M.S., Time-dependent biaxial mechanical behavior of the aortic heart valve leaflet. *Journal of Biomechanics*, 2007. 40(14): pp. 3169-3177.

132. Stella, J.A. and Sacks, M.S., On the biaxial mechanical properties of the layers of the aortic valve leaflet. *Journal of Biomechanical Engineering*, 2007. 129(5): pp. 757-766.

133. Stemper, B.D., Yoganandan, N., Stineman, M.R., Gennarelli, T.A., Baisden, J.L., and Pintar, F.A., Mechanics of fresh, refrigerated, and frozen arterial tissue. *Journal of Surgical Research*, 2007. 139(2): pp. 236-242.

134. Stevanella, M., Maffessanti, F., Conti, C.A., Votta, E., Arnoldi, A., Lombardi, M., Parodi, O., Caiani, E.G., and Redaelli, A., Mitral valve patient-specific finite element modeling from cardiac MRI: application to an annuloplasty procedure. *Cardiovascular Engineering and Technology*, 2011. 2(2): pp. 66-76.

135. Stevanella, M., Votta, E., Lemma, M., Antona, C., and Redaelli, A., Finite element modelling of the tricuspid valve: A preliminary study. *Medical Engineering and Physics*, 2010. 32(10): pp. 1213-1223.

136. Stuge, O. and Liddicoat, J., Emerging opportunities for cardiac surgeons within structural heart disease. *The Journal of Thoracic and Cardiovascular Surgery*, 2006. 132(6): pp. 1258-1261.

137. Sukmawan, R., Watanabe, N., Ogasawara, Y., Yamaura, Y., Yamamoto, K., Wada, N., Kume, T., Okura, H., and Yoshida, K., Geometric changes of tricuspid valve tenting in tricuspid regurgitation secondary to pulmonary hypertension quantified by novel system with transthoracic real-time 3-dimensional echocardiography. *Journal of the American Society of Echocardiography*, 2007. 20(5): pp. 470-476.

138. Sun, Y.-P. and O'Gara, P.T., Epidemiology, anatomy, pathophysiology and clinical evaluation of functional tricuspid regurgitation. *Minerva Cardioangiologica*, 2017. 65(5): pp. 469-479.

139. Tabata, M., Kasegawa, H., Fukui, T., Shimizu, A., Sato, Y., and Takanashi, S., Long-term outcomes of artificial chordal replacement with tourniquet technique in mitral valve repair: A single-center experience of 700 cases. *Journal of Thoracic and Cardiovascular Surgery*, 2014. 148(5): pp. 2033-2038. e1.

140. Tang, G.H.L., David, T.E., Singh, S.K., Maganti, M.D., Armstrong, S., and Borger,

M.A., Tricuspid valve repair with an annuloplasty ring results in improved long-term outcomes. *Circulation*, 2006. 114(1 suppl): pp. I-577-I-581.

141. Taramasso, M., Pozzoli, A., Guidotti, A., Nietlispach, F., Inderbitzin, D.T., Benussi, S., Alfieri, O., and Maisano, F., Percutaneous tricuspid valve therapies: The new frontier. *European Heart Journal*, 2016. 38(9): pp. 639-647.

142. Ton-Nu, T.-T., Levine, R.A., Handschumacher, M.D., Dorer, D.J., Yosefy, C., Fan, D., Hua, L., Jiang, L., and Hung, J., Geometric determinants of functional tricuspid regurgitation: Insights from 3-dimensional echocardiography. *Circulation*, 2006. 114(2): pp. 143-149.

143. Tribouilloy, C.M., Enriquez-Sarano, M., Bailey, K.R., Tajik, A.J., and Seward, J.B., Quantification of tricuspid regurgitation by measuring the width of the vena contracta with Doppler color flow imaging: A clinical study. *Journal of the American College of Cardiology*, 2000. 36(2): pp. 472-478.

144. Tribouilloy, C.M., Enriquez-Sarano, M., Capps, M.A., Bailey, K.R., and Tajik, A.J., Contrasting effect of similar effective regurgitant orifice area in mitral and tricuspid regurgitation: A quantitative Doppler echocardiographic study. *Journal of the American Society of Echocardiography*, 2002. 15(9): pp. 958-965.

145. Vesely, I. and Lozon, A., Natural preload of aortic valve leaflet components during glutaraldehyde fixation: Effects on tissue mechanics. *Journal of Biomechanics*, 1993. 26(2): pp. 121-131.

146. Wang, Q., Sirois, E., and Sun, W., Patient-specific modeling of biomechanical interaction in transcatheter aortic valve deployment. *Journal of Biomechanics*, 2012. 45(11): pp. 1965-1971.

147. Wang, Q. and Sun, W., Finite element modeling of mitral valve dynamic deformation using patient-specific multi-slices computed tomography scans. *Annals of Biomedical Engineering*, 2013. 41(1): pp. 142-153.

148. Wenk, J.F., Ratcliffe, M.B., and Guccione, J.M., Finite element modeling of mitral leaflet tissue using a layered shell approximation. *Medical & Biological Engineering & Computing*, 2012. 50(10): pp. 1071-1079.

149. Woo, S.L.-Y., Orlando, C.A., Camp, J.F., and Akeson, W.H., Effects of postmortem storage by freezing on ligament tensile behavior. *Journal of Biomechanics*, 1986. 19(5): pp. 399-404.

150. Yu, W.-J., Shen, M., Chen, W.-N., Zhan, Z.-H., Gong, Y.-J., Lin, Y., Liu, O., and Zhang, J., Differential evolution with two-level parameter adaptation. *IEEE Transactions on Cybernetics*, 2014. 44(7): pp. 1080-1099.

151. Yu, W.-j. and Zhang, J. *Multi-population differential evolution with adaptive parameter control for global optimization*. in *Proceedings of the 13th Annual Conference on Genetic and Evolutionary Computation*. 2011. ACM.

152. Zhang, W., Ayoub, S., Liao, J., and Sacks, M.S., A meso-scale layer-specific structural constitutive model of the mitral heart valve leaflets. *Acta Biomaterialia*, 2016. 32: pp. 238-255.

153. Zou, D., Wu, J., Gao, L., and Li, S., A modified differential evolution algorithm for unconstrained optimization problems. *Neurocomputing*, 2013. 120: pp. 469-481.